# A Model to Predict the Elastic Properties of Reticulated Porous Ceramics

**A DISSERTATION**

**SUBMITTED TO THE FACULTY OF THE**

**UNIVERSITY OF MINNESOTA**

**BY**

**Stephen Joseph Sedler**

**IN PARTIAL FULFILLMENT OF THE REQUIREMENTS**

**FOR THE DEGREE OF**

**DOCTOR OF PHILOSOPHY**

**Prof. Thomas R. Chase and Prof. Jane H. Davidson**

**November 2016**

# Acknowledgements

I would like to thank Prof. Thomas Chase and Prof. Jane Davidson for all of their guidance and support in completing this project and all the other projects along the way. I would also like to thank my fellow Solar Energy Laboratory graduate students for all of their constructive input and friendships – Peter Krenzke, Rohini Bala Chandran, Brandon Hathaway, Adam Gladen, Luke Venstrom, Daniel Thomas, Shuping Wang, Jesse Fosheim, Aayan Banerjee, and Justin Lapp. Thank you to the people and teams that got me out of the office – Jon Meyer, Venkat Durbha, The Angry Carrots, and The Titans. Special thanks to the department staff that was always willing to help – John Gardner, Jennifer Dahal, Don Haney, Alyssa Burger, and Mike Gust. This work was supported by the National Science Foundation (EFRI-1038307) and the University of Minnesota Initiative for Renewable Energy and the Environment.

# Dedication

To Mom

and Dad and T and Austyn

who are *still* most definitely cruzin'

HTE

## Abstract

Reticulated porous ceramics (RPCs) have a number of useful applications, but utilizing them in structural applications is hampered by the lack of models to accurately predict their elastic properties. The existing models for the elastic properties of foams do not take into account the features present in RPCs, specifically the distinctive shape of the cross sections of the ligaments. The work herein presents the development of an analytical model to predict the elastic material properties of RPCs based on the realistic ligament matrix geometry. Also presented is a validation of the elastic modulus model using experimental results for a cerium dioxide (ceria) RPC and data from the literature of other RPCs.

The RPC is represented by a repeating unit structure of truncated octahedrons (tetrakaidecahedrons) with the ligaments represented by the cell edges. The deformations of the ligaments in the cellular structure under applied loads are used to determine the effective elastic modulus, shear modulus, and Poisson's ratio of the bulk material. The model is the first to consider the effect of the features of ligaments of RPCs on the elastic moduli of the bulk material. The ligament cross section is represented as having a Plateau border exterior surface with a cusp half-angle that is varied between zero and 90°, and a Plateau border interior void with a cusp half-angle of zero, representative of the range seen in RPCs. The ligament cross-sectional area is permitted to

vary along its length and the distance between internal and external cusps is assumed constant. The relative density of the foam, corresponding to the length, cusp distances, and external-cusp half-angle of the ligaments, is determined using solid geometry. The relative elastic properties of the RPC are presented in relation to the relative density. The moduli depends largely on the relative density. For example, the relative elastic modulus increases by ∼4000% from a relative density of 0.03 to 0.30. The impact of the normalized length of the ligament is less important. The normalized ligament length only varies the moduli by 11–49% in the same relative density range. The impact of the external shape of a ligament on the relative moduli is insignificant.

The model was validated through comparisons with the measured elastic properties of RPCs in the literature. Additional validation of the elastic modulus model was performed using experimental results from flexural tests performed on ceria RPCs. The new model agrees within 30% of the ceria RPC elastic modulus experimental measurements, a significant improvement compared to the 95% over prediction by a previous model that uses a staggered cubic structure.

The elastic modulus and four-point flexural strength of a gelcast ceramic, cerium dioxide (ceria), with a microporosity of nominally 20% and a grain size of 11 $\mu$m from 23 to 1500 °C was measured. The ceria tested is representative of that constituting the ligaments of a reticulated porous ceramic. The data augment the sparse data published for ceria and extend previous results by 150 °C. The elastic modulus decreases from 90 GPa at 23 °C to 16 GPa at 1500 °C. The flexural strength is 78 MPa below 900 °C

and then decreases rapidly to 5 MPa at 1500 °C. These trends are consistent with data reported for other ceramics. Comparing the measured elastic modulus to prior data obtained for lower porosity shows the minimum solid area model can be used to extend the modulus data to other porosities. Similarly, the flexural strength data agree with prior data when the effects of specimen size, porosity, and grain size are taken into account. The data provide a means of projecting the ceria RPC elastic properties to different temperatures.

# Contents

# List of Tables

# List of Figures

# Chapter 1

# Introduction

This dissertation is a series of papers, each in a chapter, which includes a relevant review of the literature, a description of the methods applied, a presentation and discussion of results, and conclusion. As an ensemble, these papers develop a validated approach to determining the elastic properties of reticulated porous ceramics (RPCs) (ceramic foams) with a focus on characterization of elastic properties of cerium dioxide (ceria) RPC as an example. Ceria was selected for study because it is used in a variety of applications including engine exhaust pollution control [1], wastewater treatment [2], thin film electrolytes within solid oxide fuel cells [3], and high temperature metal redox cycles to split water and carbon dioxide [4–9]. To provide context for the work presented herein, Sec. 1.1 provides background information in regards to prior models for predicting the elastic properties of foams. The deficiencies of the models with respect to predicting RPC elastic properties are introduced as motivation for the present study.

The objectives of the thesis that address gaps in the prior work are provided in Sec. 1.2. An outline of the organization of the thesis is provided in Sec. 1.3.

## 1.1 Background

RPCs have many uses, including filtration for the foundry industry [10], supports for catalysts [11], radiant burners [12], and scaffold implants [13]. There is also recent interest in using ceria RPCs as structural elements in high temperature reduction/oxidation reactors [9, 14]. To design an RPC as a structural material, the elastic properties of the RPC must be known. Models to predict the elastic properties of foams exist, but the prior models do not accurately capture the geometry of ceramic foams. The prior models either use overly-simplified geometries such as a repetitive cubic structure, neglect shearing deformation components in their energy equation, or use ligament geometries representative of polymer or metal foams which are manufactured differently than RPCs and consequently are not the same geometry.

RPCs are fabricated commonly using the replication method, in which a polyurethane foam serves as a template for the ceramic [15, 16]. The polyurethane foam is immersed in a ceramic slurry and then fired to produce a hardened structure of cellular void spaces and ceramic ligaments (e.g. Refs. [17–19]). Based on characterization and visual observation of ceramic foams [19–24], the ligament/void structure is a polyhedron network of ligaments with the most common cell shapes being fourteen-faced polyhedrons known as "tetrakaidecahedrons" [21, 22]. The ligaments have an internal

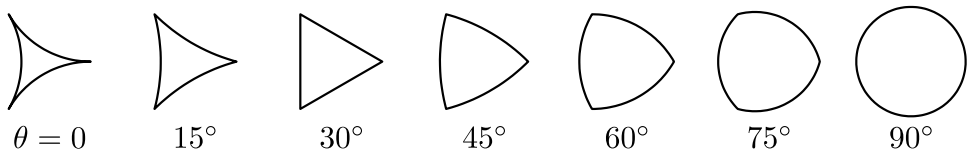


Figure 1.1: Range of Plateau border shapes used to represent the external surface of the ligaments, defined by the cusp half-angle

void resulting from volatilization of the polyurethane foam. Both the exterior of the ligament and the void typically take the shape of a "Plateau border," defined as the exclusive, bounded region created by the intersection of three circles of equal diameter having 120° of rotational symmetry [20]. Figure 1.1 illustrates a range of Plateau border shapes with varying cusp half-angle. The cross-sectional area of the central void in the ligaments varies along the length, gradually increasing from the center toward the ends of the ligament [22].

Metal foams are manufactured using a conventional casting process [25]. A mold of the polyurethane foam is created in which the metal is cast. Due to the nature of the manufacturing process, the external profiles of the ligaments of the resultant metal foam are rounder than the sharp cusp Plateau borders in polyurethane foams.

While elastic properties have been evaluated analytically for tetrakaidecahedron unit cells with cross-sectional shapes of solid triangles [25–27], squares [27], circles [25, 27], and single Plateau borders [22, 26, 27] as representations of polymer and metal foams, the double Plateau border shape representative of RPCs has not been considered.

Gibson and Ashby [28] developed the pioneering model for determining the relationship between the geometry and the elastic properties of polymer foams. The model

consists of a staggered cubic unit cell structure composed of ligaments with square cross sections. They relate the size of the ligament to both the density of the cubic cell and the deformation of the cell due to bending of the ligaments, which were treated as beams. They found that the relative moduli (the ratio of the foam moduli to the ligament moduli) are proportional to the square of the relative density (the ratio of foam density to ligament density) and determined the constant of proportionality by fitting their curve to an array of polymer foam data with relative densities ranging from 0.01 to 1.

Zhu et al. [26] and Warren and Kraynik [27] derived analytical models for the effective elastic and shear moduli of 90%-plus porosity tetrakaidecahedron unit cells with solid ligaments of uniform cross section. They modeled stretching and twisting of the ligaments in addition to bending. Results show that the cross-sectional shape of the ligaments can impact the relationships between relative moduli and relative density, where a 40% reduction in relative elastic modulus occurs when changing the ligament cross section from solid Plateau borders to circles. Gong et al. [22] and Jang et al. [25] expanded the analysis to elongated tetrakaidecahedron unit cells and allowed for axial variations in the cross-sectional area of the ligaments, while maintaining a constant shape along the length of the ligaments. They improved the model by including shearing deformations, and by more accurately modeling the material at the nodes of the cell, where the ligaments meet, in determining the relative density. Gong et al. applied the model to a solid Plateau border cross section for the analysis of polyurethane foams

with relative densities up to 0.06. Jang et al. focused on solid triangular and circular cross sections for metallic foams with relative densities up to 0.09. Through comparisons with finite element analyses of polyurethane and metal foams, both studies emphasize the importance of capturing the material distribution along the ligament length and accurately accounting for the material at the nodes.

The motivation for the work in this dissertation is the lack of an appropriate model to predict the elastic properties of RPCs. Existing models to predict the elastic properties of foams do not accurately capture the geometry of RPCs. Additionally, the lack of high temperature mechanical property data for ceria provides an opportunity to expand the database of mechanical properties needed for recently proposed uses of ceria, while also using ceria as a representative ceramic in the validation of the RPC model.

## 1.2 Research Objectives

The primary objective of the present work is to develop and validate a model for predicting the elastic properties of RPCs. A secondary objective is to characterize the elastic modulus and flexural strength of material representative of the morphology of ceramic ligaments in RPCs. The ligament elastic modulus is useful in applying the model and provides a means for validation. Ceria was selected as an example ceramic because of interest in this material at the University of Minnesota for solar thermochemical redox cycles [6–9] and its use in other applications. Prior data for mechanical properties of ceria are limited to temperatures less than 1350 °C [29, 30]. Moreover, much of

the prior data is difficult to interpret due to inadequate description of the material or experimental technique.

## 1.3 Thesis Organization

Chapter 2 is the development of an analytical model to predict the elastic modulus, shear modulus, and Poisson's ratio of RPCs based on their ligament matrix geometries. The tetrakaidecahedron repetitive structure used is representative of the structure of RPCs and takes into account the varying cross-sectional shapes of the ligaments in RPCs. The elastic properties of RPCs are influenced by the elastic modulus of the ligament material, and the macroscopic porosity of the foam. The cross-sectional shape of the ligaments, within the bounds of a double Plateau border, is shown to have negligible effect on the properties at a fixed relative density. Functional relationships of the elastic and shear moduli of the RPCs, dependent on the relative density of the RPCs, are presented. The results of the model are validated using data for alumina, mullite, cordierite, and Si-SiC RPCs available in the scientific literature [23, 24, 31, 32], and experimental data from flexural tests performed on ceria RPC.[1]

Chapter 3 is an experimental characterization of the elastic modulus and the flexural strength of gelcast ceria specimens, fabricated to mimic the pore size distribution and porosity of the ligaments in ceria RPC. The elastic modulus and flexural strength of the gelcast ceria are characterized from 23 to 1500 °C. The minimum solid area approach

[1] Details of the ceria RPC experiment are provided in Appendix A.

[33] is used to interpret the impact of porosity of the specimens on the elastic modulus. This approach allows comparison of the gelcast ceria data to prior data [29, 34–37]. Both the elastic modulus and flexural strength data obtained at room temperature agree with the published data [30, 38] when the effects of specimen size, porosity, and grain size are considered.

Chapter 4 summarizes the findings from Chapters 2 and 3. The contributions of this work are summarized and conclusions are drawn. Possible areas of future investigation are presented.

# Chapter 2

# Modeling the Elastic Properties of Reticulated Porous Ceramics[1]

## 2.1 Summary

A model to predict the elastic material properties of reticulated porous ceramics (RPCs) based on the microstructural geometry is presented. The RPC is represented by a repeating unit structure of truncated octahedrons (tetrakaidecahedrons) with the ligaments represented by the cell edges. The deformations of the ligaments in the cellular structure under applied loads are used to determine the effective moduli and Poisson's ratio of the bulk material. The ligament cross section is represented as having a Plateau

[1] **This chapter is based on the article Stephen J. Sedler, Thomas R. Chase, and Jane H. Davidson. Modeling the Elastic Properties of Reticulated Porous Ceramics. Journal of Engineering Materials and Technology, 139(1):011011, January 2017. [DOI: 10.1115/1.4035098]**

border exterior surface with a cusp half-angle that is varied between zero and 90°, and a Plateau border interior void with a cusp half-angle of zero, representative of the ranges seen in RPCs. The ligament cross-sectional area is permitted to vary along its length and the distance between internal and external cusps is assumed constant. The relative density of the foam, corresponding to the length, cusp distances, and external-cusp half-angle of the ligaments, is determined using solid geometry. The relative density has the dominant effect on the moduli, while normalized ligament length varies the moduli by 11–49% at a specified relative density. The impact of the external shape of a ligament on the relative moduli is insignificant. The model is validated through comparisons with the measured elastic properties of RPCs in the literature and new data. The model is the first to consider the effect of the microstructural features of ligaments of RPCs on the elastic moduli of the bulk material.

## 2.2 Introduction

Reticulated porous ceramics (RPCs) have been used as filtration devices in the foundry industry for decades [10] and have other applications as supports for catalysts [11], radiant burners [12], and scaffold implants [13]. RPCs are commonly fabricated using the replication method in which a polyurethane foam serves as a template for the ceramic [15, 16]. The polyurethane foam is immersed in a ceramic slurry and then fired to produce a hardened structure of cellular void spaces and ceramic ligaments (e.g., see

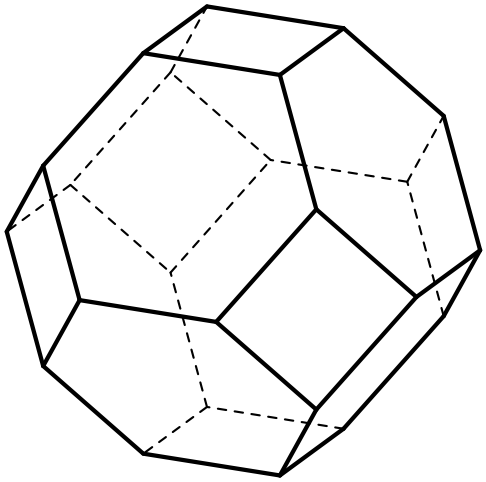

Figure 2.1: A tetrakaidecahedron, representative of the cellular structure of RPCs

Refs. [17–19]). Based on characterization and visual observation of ceramic foams [19–24], the ligament/void structure is a polyhedron network of ligaments with the most common cell shapes being fourteen-faced polyhedrons known as "tetrakaidecahedrons" [21, 22] (see Fig. 2.1). The ligaments have an internal void resulting from volatilization of the polyurethane foam. Both the exterior of the ligament and the void typically take the shape of a "Plateau border," defined as the exclusive, bounded region created by the intersection of three circles of equal diameter having 120° of rotational symmetry [20]. Figure 2.2 shows a representative image of the RPC ligament/void structure and a sectional view of a typical double Plateau border ligament. The cross-sectional area of the central void in the ligaments varies along the length, gradually increasing from the center toward the ends of the ligament [22].

For structural applications, knowledge of the impact of the geometry of the RPC on the mechanical properties of the RPC is important. While elastic properties have been

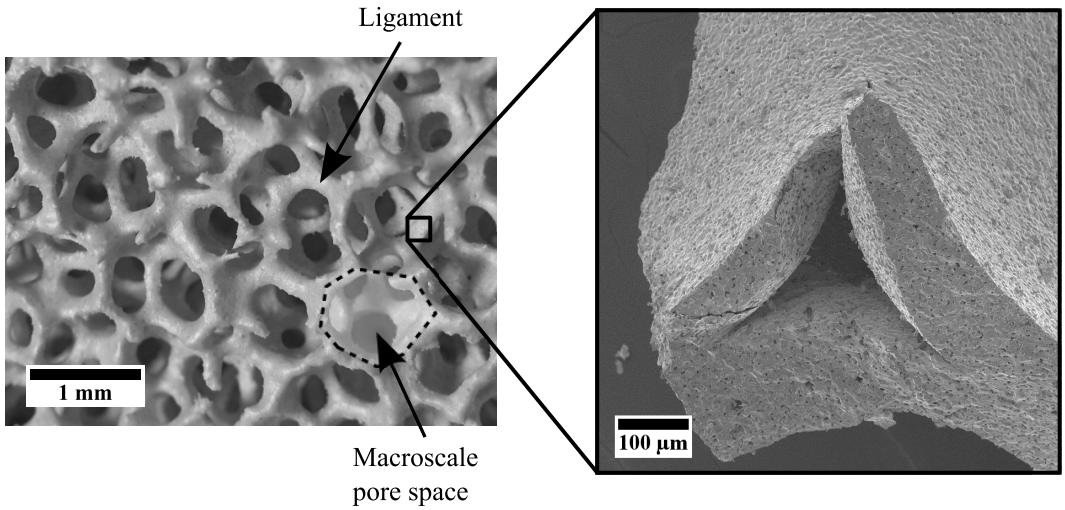


Figure 2.2: Macroscale photograph of an RPC with an inset scanning electron micrograph of a sectioned RPC ligament, exposing the Plateau border shaped void in the center

evaluated analytically for tetrakaidecahedron unit cells with cross-sectional shapes of solid triangles [25–27], squares [27], circles [25, 27], and single Plateau borders [22, 26, 27] as representations of polymer and metal foams, the double Plateau border shape representative of RPCs has not been considered.

Gibson and Ashby [28] provide an early model for determining the relationship between the geometry and the elastic properties of polymer foams. Their model consists of a staggered cubic unit cell structure composed of ligaments with square cross sections. They relate the size of the ligament to both the density of the cubic cell and the deformation of the cell due to bending of the ligaments, which were treated as beams. They found that the relative moduli (the ratio of the foam moduli to the ligament moduli) are proportional to the square of the relative density (the ratio of foam density to

ligament density) and determined the constant of proportionality by fitting their curve to an array of polymer foam data with relative densities ranging from 0.01 to 1.

Zhu et al. [26] and Warren and Kraynik [27] derived analytical models for the effective elastic and shear moduli of 90%-plus porosity tetrakaidecahedron unit cells with solid ligaments of uniform cross section. They modeled stretching and twisting of the ligaments in addition to bending. Results show the cross-sectional shape of the ligaments impacts the relationships between relative moduli and relative density. Gong et al. [22] and Jang et al. [25] expanded the analysis to elongated tetrakaidecahedron unit cells and allowed for axial variations in the cross-sectional area of the ligaments, while maintaining a constant shape along the length of the ligaments. They improved the model by including shearing deformations, and by more accurately modeling the material at the nodes of the cell, where the ligaments meet, in determining the relative density. Gong et al. applied the model to a solid Plateau border cross section for the analysis of polyurethane foams with relative densities up to 0.06. Jang et al. focused on solid triangular and circular cross sections for metallic foams with relative densities up to 0.09. Through comparisons with finite element analyses of polyurethane and metal foams, both studies emphasized the importance of capturing the material distribution along the ligament length and accurately accounting for the material at the nodes.

In addition to the analytical approaches used to quantify the relationship between relative moduli and relative density, experimental measurements of moduli are available for cordierite [31], mullite [32], and alumina [24] RPCs. Numerical simulation data are

available for Si-SiC [23] RPC manufactured using the replication method.

While the complexity of the various analytical models examined differ, all of the results predict that the relative moduli are well represented by Eqs. (2.1) and (2.2).

$$\frac{E^*}{E_\mathrm{s}} = C_1 \left(\frac{\rho^*}{\rho_\mathrm{s}}\right)^{n_1} \tag{2.1}$$

$$\frac{G^*}{E_\mathrm{s}} = C_2 \left(\frac{\rho^*}{\rho_\mathrm{s}}\right)^{n_2} \tag{2.2}$$

In these equations, $E^*$ is the elastic modulus of the foam, $G^*$ is the shear modulus of the foam, $E_\mathrm{s}$ is the elastic modulus of the ligament material, $\rho^*$ is the density of the foam, and $\rho_\mathrm{s}$ is the density of the ligament material. The $C_1$, $C_2$, $n_1$, and $n_2$ constants are determined either analytically, with their values varying based on the shape of the ligament [22, 26, 27], or experimentally [24, 28, 31]. The $C$ and $n$ constants from these analytical and experimental studies are listed in Table 2.1.

The goal of the present study is to develop expressions for the elastic modulus, shear modulus, and Poisson's ratio of RPCs with respect to the relative density for ligaments with varying double Plateau border cross-sectional shapes and lengths representative of RPCs. This study exploits the generality of the model developed by Gong et al. [22], where the ligaments are treated as deformable beams, with compliances for axial, bending, shearing, and torsional loads, assembled in a representative tetrakaidecahedron structure. However, it extends their work by including the effect of the interior voids in the ligaments that are characteristic of RPCs manufactured using the replication

Table 2.1: Constants and 95% confidence intervals for the power-law description of relative elastic and shear moduli with respect to relative density for various studies. †Fixed value when fitting the $C_1$ coefficient. ‡Fixed value when fitting the $C_2$ coefficient.

| *Study* | $C_1$ | $n_1$ | $C_2$ | $n_2$ | *Notes* |
|---|---|---|---|---|---|
| | | | *Experimental* | | |
| Gibson and Ashby [28]; staggered cubic | 1 | 2† | 0.4 | 2‡ | polymer foams; $0.01 < \rho^*/\rho_s < 1$ |
| Hagiwara and Green [24] | $0.236 \pm 0.195$ | $1.819 \pm 0.443$ | — | — | alumina RPC; $0.08 < \rho^*/\rho_s < 0.18$ |
| | — | — | $0.127 \pm 0.157$ | $1.928 \pm 0.627$ | alumina RPC; $0.08 < \rho^*/\rho_s < 0.16$ |
| Costa Oliveira [31] | $5.621 \pm 4.838$ | $3.074 \pm 0.538$ | $4.183 \pm 2.584$ | $3.276 \pm 0.388$ | cordierite RPC; $0.14 < \rho^*/\rho_s < 0.22$ |
| | | | *Analytical* | | |
| Warren and Kraynik [27]; tetrakaidecahedron | 0.593 | 2† | 0.200 | 2‡ | circle; $\rho^*/\rho_s \ll 1$ |
| | 0.619 | | 0.210 | | square; $\rho^*/\rho_s \ll 1$ |
| | 0.710 | | 0.242 | | triangle; $\rho^*/\rho_s \ll 1$ |
| | 0.979 | | 0.336 | | Plateau border; $\rho^*/\rho_s \ll 1$ |
| Zhu et al. [26]; tetrakaidecahedron | 0.559 | 1.930 | 0.196 | 1.954 | triangle; fit curve up to $\rho^*/\rho_s = 0.1$ |
| | 0.708 | 1.906 | — | — | Plateau border; fit curve up to $\rho^*/\rho_s = 0.1$ |
| Gong et al. [22]; tetrakaidecahedron | 1.366 | 1.929 | 0.733 | 2.152 | Plateau border; fit curve up to $\rho^*/\rho_s = 0.06$ |

method and by allowing for the cross-sectional shape of a ligament to vary along its length.

A description of the ligament geometry within RPC is presented in Sec. 2.3. The method used to generate the relationship between relative moduli and relative density is described in Sec. 2.4. The results of the analysis are presented, discussed, and compared to data in Sec. 2.5. Conclusions are drawn in Sec. 2.6.

## 2.3 Ligament Geometry for RPCs

Ceramic foams are represented by tetrakaidecahedron unit cells as illustrated in Fig. 2.1. The tetrakaidecahedron has fourteen faces, eight of which are regular hexagons and six of which are squares. The edges of the tetrakaidecahedron unit cell represent the central axes of the ceramic ligaments.

The ligament cross section is a double Plateau border. The double Plateau border cross section geometry is characterized by concentric Plateau borders, where the external Plateau border constitutes the exposed surface of the ceramic foam and the internal Plateau border constitutes the internal void surface of the ligaments (see Fig. 2.3). The Plateau border shape is fully defined by specifying any two of the five variables, $A$ (area inside the Plateau border), $c$ (half-distance between the Plateau border centroid and cusps), $R$ (radius of the Plateau border arcs), $\alpha$ (distance between the Plateau border

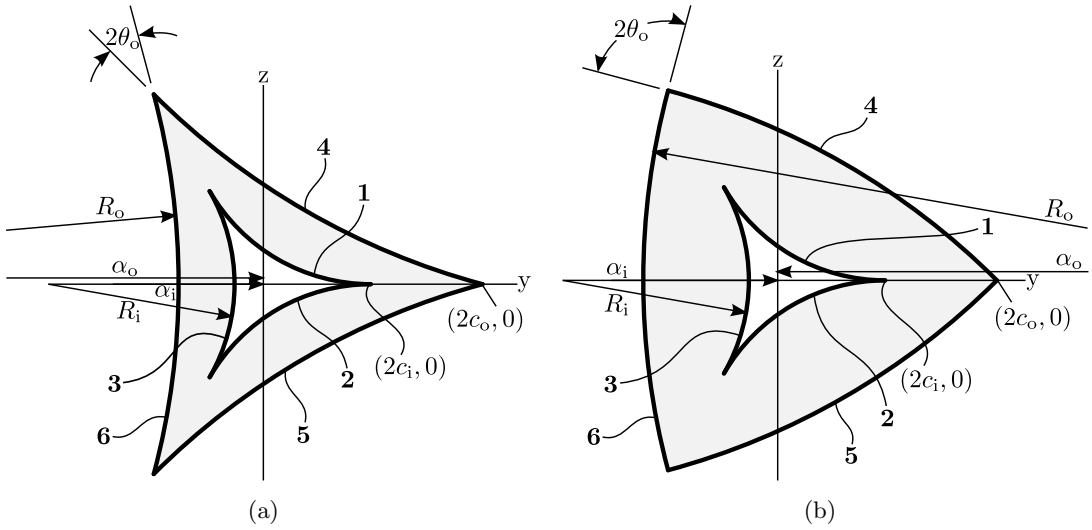


Figure 2.3: The double Plateau border cross section with an external cusp half-angle of (a) less than 30° and (b) greater than 30°. Arcs 1, 2, and 3 construct the internal Plateau border while arcs 4, 5, and 6 construct the external Plateau border. Equations defining the Plateau border arcs are provided in Appendix B.

centroid and center of the arcs), or $\theta$ (Plateau border cusp half-angle), and Eqs. (2.3)–(2.5).

$$\alpha = \frac{2\sqrt{3}\cos\theta}{3}R \tag{2.3}$$

$$c = \frac{\sqrt{3}\cos\theta - 3\sin\theta}{6}R \tag{2.4}$$

$$A = \begin{cases} 3\left[-R^2\sin^{-1}\left(\sqrt{3}\frac{c}{R}\right) + 2cR\cos\theta\right], & 0 \le \theta < 30° \\ 3\left[R^2\sin^{-1}\left(\sqrt{3}\frac{c}{R}\right) - 2cR\cos\theta\right], & 30° < \theta \le 90° \end{cases} \tag{2.5}$$

The internal Plateau border cusp half-angle is defined as zero, representative of the void shape generated by the polyurethane foam volatilization during manufacture. The

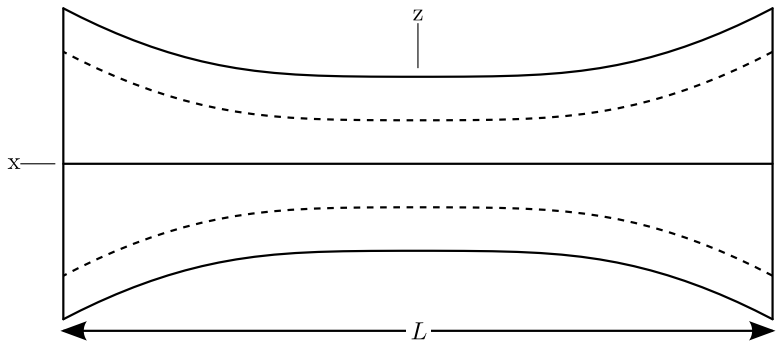


Figure 2.4: The concentric Plateau borders ligament shape

external Plateau border cusp half-angle, $\theta_o$, is permitted to vary from zero to 90° to model the variation possible in the fired ceramic slurry from the replication manufacturing procedure.[2] The shape of the ligament varies along its longitudinal $x$-axis, as illustrated in Fig. 2.4. The length of the ligament is $L$. The axial shape is defined by the cross-sectional area of the internal void, $A_i(\xi)$, where $\xi = \frac{x}{L}$, and the midplane thickness ratio, defined as the ratio of external-cusp location to internal-cusp location at the midplane of the ligament, $\zeta = \left.\frac{2c_o(\xi)}{2c_i(\xi)}\right|_{\xi=0}$. Because polyurethane foam is used as the template in making RPCs, the nondimensionalized area shape function, $f_i(\xi)$, measured by Gong et al. [22] for polyurethane foams, given in Eq. (2.6), is used to model the internal void area distribution

$$f_i(\xi) = \frac{A_i(\xi)}{A_i(0)} = 86\xi^4 + \xi^2 + 1 \tag{2.6}$$

Because the ligament is a complex three-dimensional geometry, an assumption needs

[2] A cusp half-angle of 30° yields an equilateral triangle and 90° yields a circle.

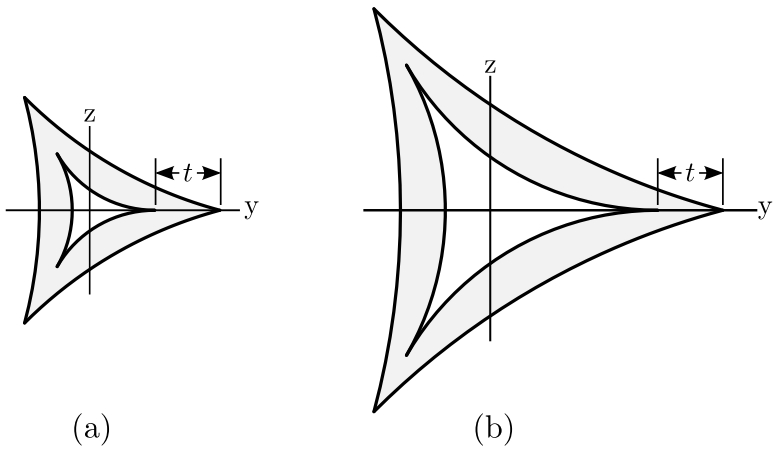


Figure 2.5: Cross sections (a) at the midplane ($\xi = 0$) and (b) at an end-plane ($\xi = \frac{1}{2}$) of a ligament defined by $\zeta = 2$ and $\theta_o = 15°$. Distance $t$ is assumed to remain constant along the entire length of the ligament.

to be made about how the slurry is deposited along the length of the ligament. In the present work, the distance between internal and external cusps, $t$, is assumed to be uniform along the length of the ligament. An example of the geometry produced by this assumption is provided in Fig. 2.5. This distance is related to the defined thickness ratio, $\zeta$, by

$$t = 2\,(\zeta - 1)\,c_i(0) \tag{2.7}$$

Other assumptions used to define the thickness along the length of the ligament may be reasonable, but are outside the scope of this study.

The ligament cross sections at all nondimensionalized axial positions are defined by specifying the internal void area at the ligament midplane, $A_i(0)$, external cusp half-angle, $\theta_o$, and midplane thickness ratio, $\zeta$, along with the internal area void shape function,

Eq. (2.6). All remaining cross-sectional parameters are then defined by Eqs. (2.8)–(2.13).

$$R_{\mathrm{i}}(\xi) = \sqrt{\frac{A_{\mathrm{i}}}{\sqrt{3} - \frac{\pi}{2}}} \tag{2.8}$$

$$\alpha_{\mathrm{i}}(\xi) = \frac{2\sqrt{3}R_{\mathrm{i}}}{3} \tag{2.9}$$

$$c_{\mathrm{i}}(\xi) = \frac{\sqrt{3}}{6}R_{\mathrm{i}} \tag{2.10}$$

$$c_{\mathrm{o}}(\xi, \zeta) = c_{\mathrm{i}} + (\zeta - 1)c_{\mathrm{i}}(0) \tag{2.11}$$

$$\alpha_{\mathrm{o}}(\xi, \zeta, \theta_{\mathrm{o}}) = \frac{4\cos(\theta_{\mathrm{o}})}{\cos(\theta_{\mathrm{o}}) - \sqrt{3}\sin(\theta_{\mathrm{o}})}c_{\mathrm{o}} \tag{2.12}$$

$$R_{\mathrm{o}}(\xi, \zeta, \theta_{\mathrm{o}}) = \begin{cases} \frac{2\sqrt{3}}{\cos(\theta_{\mathrm{o}}) - \sqrt{3}\sin(\theta_{\mathrm{o}})}c_{\mathrm{o}}, & 0 \leq \theta_{\mathrm{o}} < 30^{\circ} \\ \frac{-2\sqrt{3}}{\cos(\theta_{\mathrm{o}}) - \sqrt{3}\sin(\theta_{\mathrm{o}})}c_{\mathrm{o}}, & 30^{\circ} < \theta_{\mathrm{o}} \leq 90^{\circ} \end{cases} \tag{2.13}$$

Defining the ligament length, $L$, or equivalently, the ratio of this length to the square root of the void area at the ligament center, $L/\sqrt{A_{\mathrm{i}}(0)}$, then fully defines the ligament geometry. The second measure is used here; it is called the "normalized length" of the ligament. Three parameters are varied to investigate the potential impact of geometric variations: $\zeta$, $\theta_{\mathrm{o}}$, and $L/\sqrt{A_{\mathrm{i}}(0)}$. The ligament cross-sectional area along with the

second moment of area, $I$, is calculable using Eqs. (2.14)–(2.19).

$$A_{\mathrm{o}}(\xi,\zeta,\theta_{\mathrm{o}}) = \begin{cases} 3\left[-R_{\mathrm{o}}^2\sin^{-1}\left(\frac{\sqrt{3}c_{\mathrm{o}}}{R_{\mathrm{o}}}\right) + 2c_{\mathrm{o}}R_{\mathrm{o}}\cos(\theta_{\mathrm{o}})\right], & 0 \le \theta_{\mathrm{o}} < 30^\circ \\ 3\left[R_{\mathrm{o}}^2\sin^{-1}\left(\frac{\sqrt{3}c_{\mathrm{o}}}{R_{\mathrm{o}}}\right) - 2c_{\mathrm{o}}R_{\mathrm{o}}\cos(\theta_{\mathrm{o}})\right], & 30^\circ < \theta_{\mathrm{o}} \le 90^\circ \end{cases} \tag{2.14}$$

$$A(\xi,\zeta,\theta_{\mathrm{o}}) = A_{\mathrm{o}} - A_{\mathrm{i}} \tag{2.15}$$

$$I_{\mathrm{z,i}}(\xi) = \frac{R_{\mathrm{i}}^4}{24}\left[20\sqrt{3} - 11\pi\right] \tag{2.16}$$

$$\begin{aligned} I_{\mathrm{z,o}}(\xi,\zeta,\theta_{\mathrm{o}}) =& \frac{-R_{\mathrm{o}}^4}{24}\Bigg[6\sin^{-1}\left(\frac{\cos(\theta_{\mathrm{o}}) - \sqrt{3}\sin(\theta_{\mathrm{o}})}{2}\right)\Big(7 + 4\cos(2\theta_{\mathrm{o}})\Big) \\ &+ \cos(\theta_{\mathrm{o}})\Big(-21\sqrt{3}\cos(\theta_{\mathrm{o}}) + \sqrt{3}\cos(3\theta_{\mathrm{o}}) + 57\sin(\theta_{\mathrm{o}}) + 3\sin(3\theta_{\mathrm{o}})\Big)\Bigg] \end{aligned} \tag{2.17}$$

$$I_{\mathrm{z}}(\xi,\zeta,\theta_{\mathrm{o}}) = I_{\mathrm{z,o}} - I_{\mathrm{z,i}} \tag{2.18}$$

Because the cross sections have three axes of symmetry [39]

$$I(\xi,\zeta,\theta_{\mathrm{o}}) = I_{\mathrm{y}} = I_{\mathrm{z}} \tag{2.19}$$

## 2.4 Model and Methods

To model the elastic properties of an RPC, it is treated as a network of ligament beams that deform under applied loads. The deformation of the network under a normal load is used to determine the elastic modulus, $E^*$, and Poisson's ratio, $\nu^*$, and the deformation

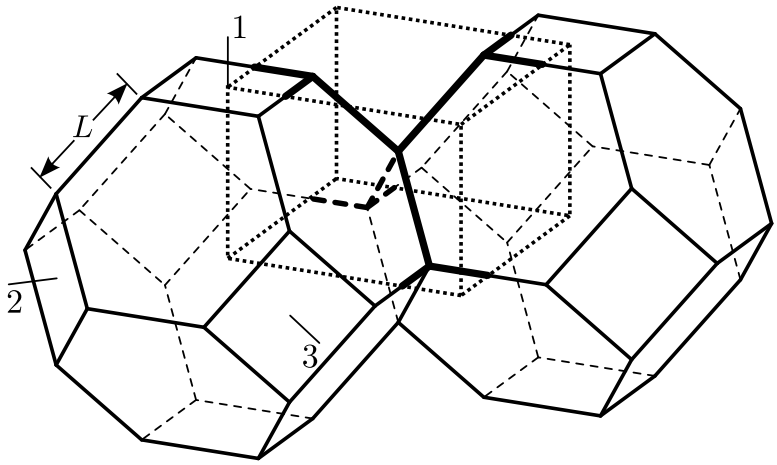


Figure 2.6: Two tetrakaidecahedron unit cells. The dotted lines form a rectangular repeating section having mirror symmetry across its faces. The ligaments in the repeating section are indicated with bold lines. The 1-, 2-, and 3-directions are perpendicular to the square faces of the tetrakaidecahedron.

under a shear load is used to determine the shear modulus, $G^*$.[3] To determine the relative elastic modulus, a unit cell of rectangular shape is defined by assembling two adjacent tetrakaidecahedrons as shown in Fig. 2.6. A rectangular cuboid unit cell with mirror symmetry across all faces is extracted from the assembly. The loads that are applied to the unit cell to determine the elastic modulus are shown in Fig. 2.7. The compressive loads, $P$, are the loads applied to generate the ligament deflections, and the moments, $M$, are resultant from the mirror-symmetry boundary conditions on the cuboid faces.

The elastic moduli in the orthogonal 1-, 2-, and 3-directions are identical due to symmetry within the tetrakaidecahedron unit cell and are defined by Eq. (2.20), where

[3] This approach is identical to the approach used by Gong et al. [22] and Jang et al. [25]. The differences between this study and the previous studies are the ability to vary the cross-sectional shape of the ligament and the inclusion of a void. This leads to a new set of constants $C_{XYZ}$ in Eq. (2.23).

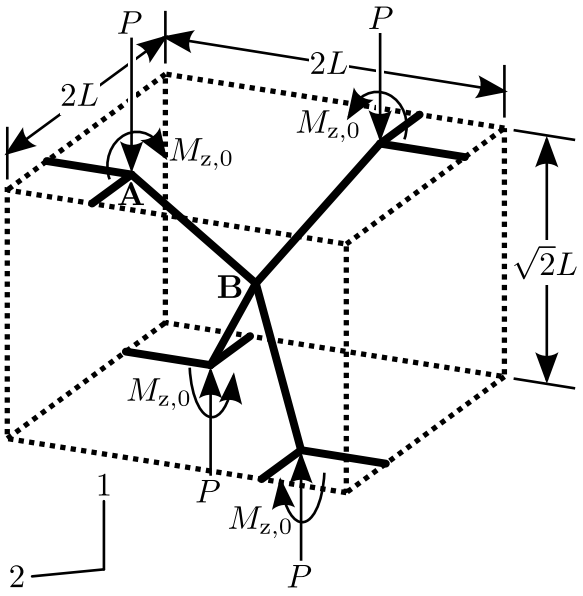


Figure 2.7: Rectangular repeating section of ligaments with mirror symmetry across the faces

$\Delta_1 = u_{1B} - u_{1A}$ is the difference in 1-direction displacements of nodes A and B

$$E_1^* = \frac{P}{2\sqrt{2}L\Delta_1} \tag{2.20}$$

The relative displacement of node B to node A in the 1-direction is determined using the free-body diagram in Fig. 2.8, and the geometrical description of the ligament. The strain energy in the ligament, $U$, is defined by Eq. (2.21).

$$U = \int_{-\frac{1}{2}}^{\frac{1}{2}} \frac{N_x^2(\xi)L}{2E_s A(\xi)}\,\mathrm{d}\xi + \int_{-\frac{1}{2}}^{\frac{1}{2}} \frac{M_z^2(\xi)L}{2E_s I_z(\xi)}\,\mathrm{d}\xi + \int_{-\frac{1}{2}}^{\frac{1}{2}} \beta_z(\xi)\frac{V_y^2(\xi)L}{2G_s A(\xi)}\,\mathrm{d}\xi + \int_{-\frac{1}{2}}^{\frac{1}{2}} \frac{T_x^2(\xi)L}{2G_s J_T(\xi)}\,\mathrm{d}\xi \tag{2.21}$$

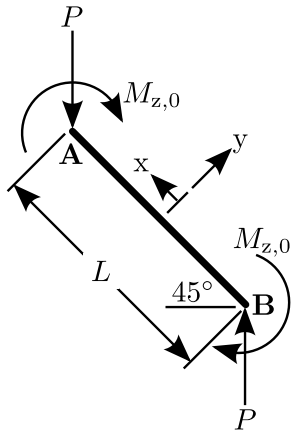


Figure 2.8: Free-body diagram of one of the diagonal ligaments

As is evident from Fig. 2.8, a normal force in the $x$-direction, bending moment in the $z$-direction, and shear force in the $y$-direction are all present in the ligament. A torque does not exist for the loading used to determine the elastic modulus.[4] Using Castigliano's second theorem of $\delta_i = \partial U/\partial P_i$ and by noting that for isotropic materials $G_s = \frac{E_s}{2(1+\nu_s)}$, the relative displacement of node B with respect to node A in the 1-direction is given by Eq. (2.22).

$$\Delta_1 = \frac{PL}{2E_s}\left[\int_{-\frac{1}{2}}^{\frac{1}{2}} \frac{1}{A(\xi)}\,\mathrm{d}\xi + L^2\int_{-\frac{1}{2}}^{\frac{1}{2}} \frac{\xi^2}{I(\xi)}\,\mathrm{d}\xi + 2\,(1+\nu_s)\int_{-\frac{1}{2}}^{\frac{1}{2}} \frac{\beta_z(\xi)}{A(\xi)}\,\mathrm{d}\xi\right] \tag{2.22}$$

By defining the geometrical integral constant $C_{XYZ}$ as

$$C_{XYZ} = \int_{-\frac{1}{2}}^{\frac{1}{2}} \frac{X(\xi)\xi^Y}{Z(\xi)}\,\mathrm{d}\xi \tag{2.23}$$

[4] Torque energy does contribute to the formulation of the shear modulus.

where $X$ is an alpha-variable when it exists, $Y$ is a numeric-variable, and $Z$ is an alpha-variable, the relative displacement in Eq. (2.22) simplifies to

$$\Delta_1 = \frac{PL}{2E_\mathrm{s}} \left[ C_{0\mathrm{A}} + L^2 C_{2\mathrm{I}} + 2\left(1+\nu_\mathrm{s}\right) C_{\beta_\mathrm{z}0\mathrm{A}} \right] \tag{2.24}$$

Combining Eqs. (2.20) and (2.24) yields Eq. (2.25), which expresses the relative elastic modulus in the 1-direction in terms of the ligament geometry and Poisson's ratio

$$\frac{E_1^*}{E_\mathrm{s}} = \frac{1}{\sqrt{2}L^2 \left[ C_{0\mathrm{A}} + L^2 C_{2\mathrm{I}} + 2\left(1+\nu_\mathrm{s}\right) C_{\beta_\mathrm{z}0\mathrm{A}} \right]} \tag{2.25}$$

To solve for the geometrical integral constants $C_{0\mathrm{A}}$ and $C_{2\mathrm{I}}$ for a specific ligament geometry defined by $\zeta$, $\theta_\mathrm{o}$, and $L/\sqrt{A_\mathrm{i}(0)}$, the analytical expressions for $A$ and $I$, Eqs. (2.15) and (2.19), respectively, are substituted into Eq. (2.23) and the integrals are evaluated numerically. To solve for the geometrical integral constant $C_{\beta_\mathrm{z}0\mathrm{A}}$, the axial dependence of the shear form factor in the $z$-direction, $\beta_\mathrm{z}(\xi)$, is required. Unlike prior analyses, the cross-sectional shape of the ligaments varies; therefore, the shear form factor in this analysis varies. To determine the axial dependence of the shear form factor for a specific ligament geometry, 21 double Plateau border cross sections, equally spaced along the ligament, are evaluated for their shear form factor using

$$\beta_\mathrm{z} = \frac{A}{I_\mathrm{z}^2} \int \frac{Q^2(y_1)}{b^2(y_1)} \, \mathrm{d}A \tag{2.26}$$

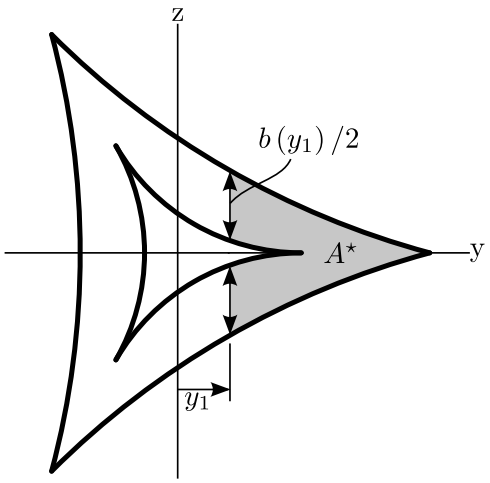


Figure 2.9: Parameters used to define the statical moment of area

where the statical moment of area is

$$Q(y_1) = \int_{A^\star} y \, \mathrm{d}A \tag{2.27}$$

as defined in Fig. 2.9. The $\xi$-dependent variation of the shear form factor of the ligament geometry is approximated by fitting an eighth-order polynomial through the 21 equally spaced $\beta_\mathrm{z}$ values along the ligament.[5] Curve fits of $\beta_\mathrm{z}$ are shown in Fig. 2.10 for example geometries. Using the $\xi$-dependent approximation of $\beta_\mathrm{z}$ along with the $\xi$-dependent cross-sectional area function, the $C_{\beta_\mathrm{z}0\mathrm{A}}$ integral is numerically integrated. Obtaining the geometrical integral constants in Eq. (2.25) enables solving for the relative elastic modulus.

[5] Because $f_\mathrm{i}(\xi)$ is an even function, $\beta_\mathrm{z}(\xi)$ is also an even function. Therefore an eighth-order, even function curve fit using 11 equally spaced $\beta_\mathrm{z}$ values from half of the ligament yields the same fit. 21 $\beta_\mathrm{z}$ values from the entire length are used to allow for use of MATLAB's [40] "poly8" curve fit model without modification.

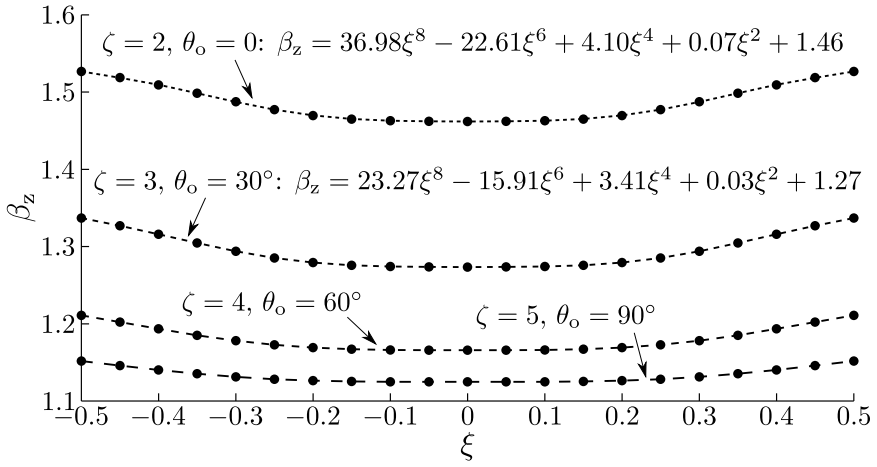


Figure 2.10: Eighth-order polynomial curves fit to the shear form factor data (generated using Eq. (2.26)) for example ligament geometries. Some example polynomials are shown.

Poisson's ratio of the RPC is the same in the 1-2-, 1-3-, and 2-3-planes due to cubic symmetry within the tetrakaidecahedron. Poisson's ratio of the RPC in the 1-2-plane, $\nu_{12}^*$, is found by determining the 2-direction relative displacement between nodes A and B, $\Delta_2$, from the same unit cell in Fig. 2.7 used to evaluate the elastic modulus

$$\begin{aligned}\nu_{12}^* &= -\frac{\varepsilon_2}{\varepsilon_1} = \frac{-\Delta_2}{2\Delta_1} \\ &= -\frac{C_{0\mathrm{A}} - L^2 C_{2\mathrm{I}} - 2(1+\nu_\mathrm{s})C_{\beta_\mathrm{z}0\mathrm{A}}}{2\left(C_{0\mathrm{A}} + L^2 C_{2\mathrm{I}} + 2(1+\nu_\mathrm{s})C_{\beta_\mathrm{z}0\mathrm{A}}\right)}\end{aligned} \tag{2.28}$$

The relative shear modulus of the RPC in the 1-2-, 1-3-, and 2-3-planes is determined in a manner similar to the relative elastic modulus, with a loading situation that deforms a different rectangular cuboid unit cell in shear as developed by Gong et al. [22]. The rectangular unit cell used has cubic symmetry, and thus $G_{12}^*$, $G_{13}^*$, and $G_{23}^*$

are equivalent. The derivation of shear modulus is provided in Appendix C and the result is given by Eq. (2.29).

$$\frac{G_{12}^{*}}{E_s} = \frac{1}{\sqrt{2}L^2\left[2C_{0\mathrm{A}} + 4(1+\nu_{\mathrm{s}})C_{\beta_{\mathrm{y}}0\mathrm{A}} + L^2\left(2C_{2\mathrm{I}} + \frac{C_{0\mathrm{I}}C_{0\mathrm{J_T}}(1+\nu_{\mathrm{s}})\left(C_{0\mathrm{I}}+2C_{0\mathrm{J_T}}(1+\nu_{\mathrm{s}})\right)}{\left(C_{0\mathrm{I}}+10C_{0\mathrm{J_T}}(1+\nu_{\mathrm{s}})\right)^2}\right)\right]} \tag{2.29}$$

The geometrical integral constants $C_{0\mathrm{I}}$ and $C_{\beta_{\mathrm{y}}0\mathrm{A}}$ are evaluated following the same approach used to solve for $C_{2\mathrm{I}}$ and $C_{\beta_{\mathrm{z}}0\mathrm{A}}$, respectively. To solve for $C_{0\mathrm{J_T}}$, the axial dependence of the torsional constant, $J_{\mathrm{T}}(\xi)$, is required. As is the case for the shear form factor, the nondimensionalized torsional constant, $D_{\mathrm{J_T}} = J_{\mathrm{T}}/(2I)$, varies due to the varying cross-sectional shape of the ligaments. To approximate this axial variation for a specific ligament geometry defined by $\zeta$, $\theta_{\mathrm{o}}$, and $L/\sqrt{A_{\mathrm{i}}(0)}$, the same 21 equally spaced double Plateau border cross sections are evaluated for their nondimensionalized torsional constant using a finite element analysis, similar to the approach used by Warren et al. [41]. The $\xi$-dependent variation of the nondimensionalized torsional constant of the ligament geometry is approximated by fitting an eighth-order polynomial through the 21 $D_{\mathrm{J_T}}$ values along the ligament. Curve fits of $D_{\mathrm{J_T}}$ are shown in Fig. 2.11 for example geometries. Because $D_{\mathrm{J_T}}(\xi)$ and $I(\xi)$ are known, $J_{\mathrm{T}}(\xi)$ is also known, thus the $C_{0\mathrm{J_T}}$ integral can be numerically evaluated.

To relate the relative moduli to the relative density, yielding a form like Eqs. (2.1) and (2.2), the relationship between the geometric parameters and relative density must

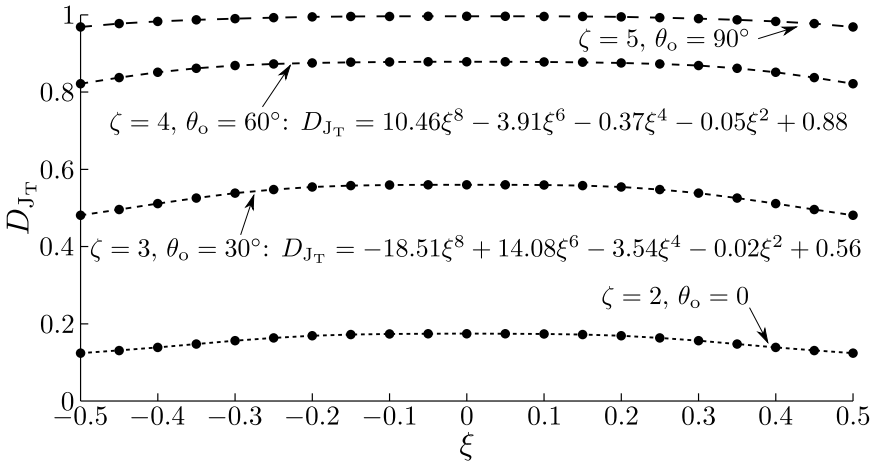


Figure 2.11: Eighth-order polynomial curves fit to the nondimensionalized torsional constant for example ligament geometries. Some example polynomials are shown.

be established. This step is done by way of a solid model. The graphical representation of the ligaments is developed using a combination of the MATLAB [40] and Creo Elements/Pro [42] software programs. For each set of geometric parameters, the cross-sectional geometry is defined and modeled at 21 equally spaced axial positions along the ligament. The arcs defining the cross sections are utilized with boundary blend, merge, and solidify features to construct the three-dimensional ligament geometry.

An assembly of ligaments is generated to create the cellular structure for the relative density calculation. To assemble the ligaments, a cut is made on both ends of the ligaments by end planes rotated 45° about their $z$-axis, as shown in Fig. 2.12(a), and a unit square is constructed by assembling four ligaments, as shown in Fig. 2.12(b). The tetrakaidecahedron geometry is constructed by assembling an array of unit squares, where each node of a unit square is coincident with only one node of an adjacent unit

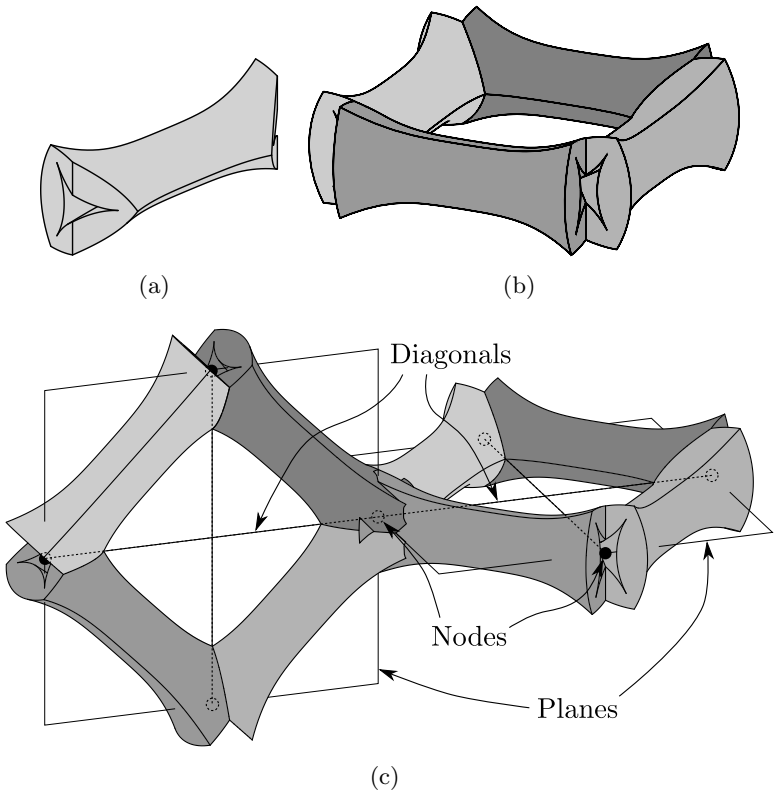


Figure 2.12: The graphical representation of (a) the ligament with the 45° end cuts, (b) the unit square assembled using four ligaments, and (c) two unit squares assembled with a common node, collinear diagonal lines, and rotated planes

square, the diagonal lines connecting unit square nodes are collinear, and adjacent unit square planes are rotated 90° from each other about their collinear diagonal lines, as shown in Fig. 2.12(c). The components in the constructed array are merged to create a single part, eliminating any double-counting of overlapping material. Cuts are taken through the planes created by the six square faces of the tetrakaidecahedron and all ligament volume outside of the six planes is removed, yielding the unit cell shown in Fig. 2.13.

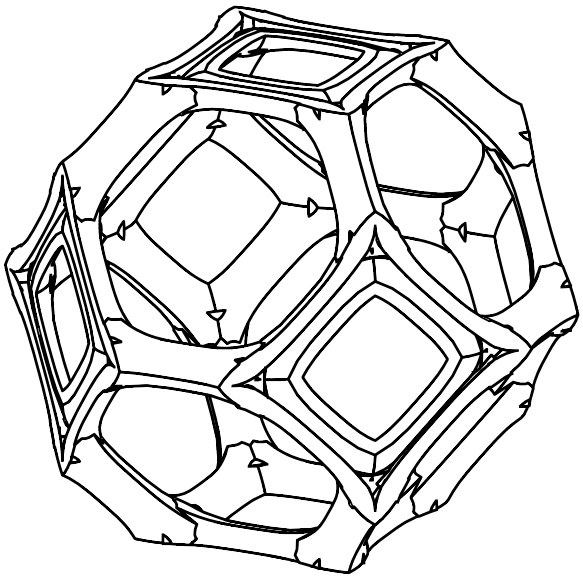

Figure 2.13: Solid model of a unit cell geometry used to determine the relative density as it relates to $\zeta$, $\theta_o$, and $L/\sqrt{A_i(0)}$. Geometry is created by assembling an array of unit squares and removing all material outside of the unit cube volume. Visible irregularities in the geometry are caused by a slight mismatch between adjacent unit squares due to ligament shape. These irregularities have a negligible contribution to the total volume.

Using the measurement capabilities of the solid modeling software, the volume of the unit cell solid is measured and divided by the volume of the enclosing cube.[6] Repeated calculations for varying geometric parameters yield relative density surfaces for fixed $L/\sqrt{A_i(0)}$ ratios and varying $\zeta$ and $\theta_o$ values. A contour plot of one such surface is shown in Fig. 2.14. With these surfaces and Eqs. (2.25) and (2.29), the relationship between the relative moduli and relative density is established for the range of geometric parameters.

[6] Note that $\rho^* = m_s / V_{cube}$ and $\rho_s = m_s / V_s$, so $\rho^*/\rho_s = V_s / V_{cube}$.

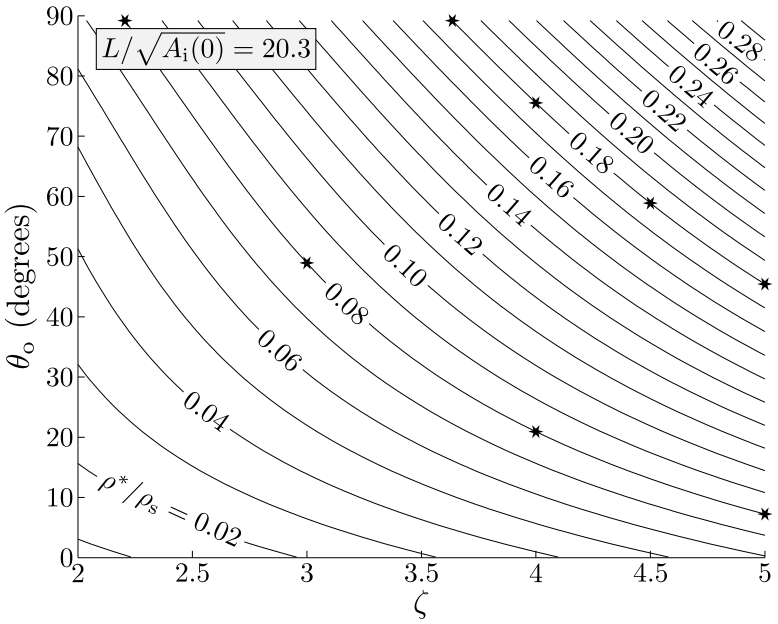


Figure 2.14: Relative density contours, generated using the unit cell geometry, for varying $\zeta$ and $\theta_o$ with $L/\sqrt{A_i(0)} = 20.3$. The marked locations are used in the generation of the curves in Fig. 2.18.

## 2.5 Results and Discussion

Figures 2.15–2.17 are plots of the relative elastic modulus, shear modulus, and Poisson's ratio, respectively, versus the relative density. Note that the plots are a collection of discrete points. For a specific ligament geometry, Eqs. (2.25) and (2.29) are used to determine the relative moduli, and Fig. 2.14 is used to determine the relative density. Equation (2.28) is used to determine Poisson's ratio. Within each plot, two sets of data, distinguished by the $L/\sqrt{A_i(0)}$ ratio, are shown for the range of geometries examined. The two $L/\sqrt{A_i(0)}$ ratios evaluated in this study come from the extremes of the range measured in the work of Gong et al. on polyurethane foams [22]. The two sets of data

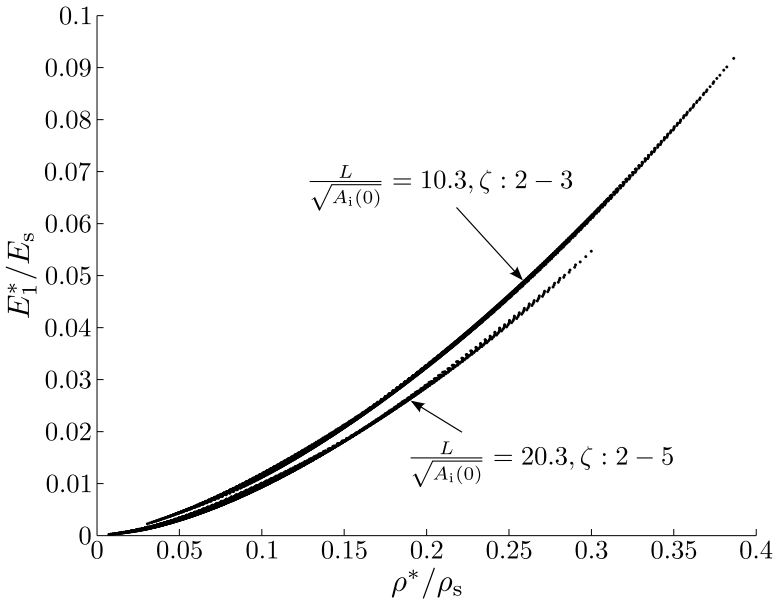


Figure 2.15: Relative density dependence of the relative elastic modulus. The different curves are for different ligament $L/\sqrt{A_i(0)}$ ratios, and plotting the entire range of $\zeta$ and $\theta_o$ investigated. The $\theta_o$ range examined spans from zero to 90°. The curves nearly collapse on each other regardless of $\zeta$ and $\theta_o$.

bound the expected relative moduli and Poisson's ratio. The data represented by an input of $L/\sqrt{A_i(0)} = 20.3$ use values of $2 \leq \zeta \leq 5$ and $0 \leq \theta_o \leq 90°$ to generate the geometry.[7] The data represented by the input of $L/\sqrt{A_i(0)} = 10.3$ use values of $2 \leq \zeta \leq 3$ and $0 \leq \theta_o \leq 90°$ to generate the geometry. The extremes of the $\zeta$ ranges represent limits established to maintain an open-cell structure in the RPC. Poisson's ratio of 0.3 is assumed for the ligament material. Between the two sets of $L/\sqrt{A_i(0)}$ data, the relative elastic modulus varies by up to 40% at a relative density of 0.03 and up to 11% at a relative density of 0.30. For the relative shear modulus,

[7] It is noted that this $\theta_o$ range includes some impractical ligament geometries for an RPC generated using the replication method.

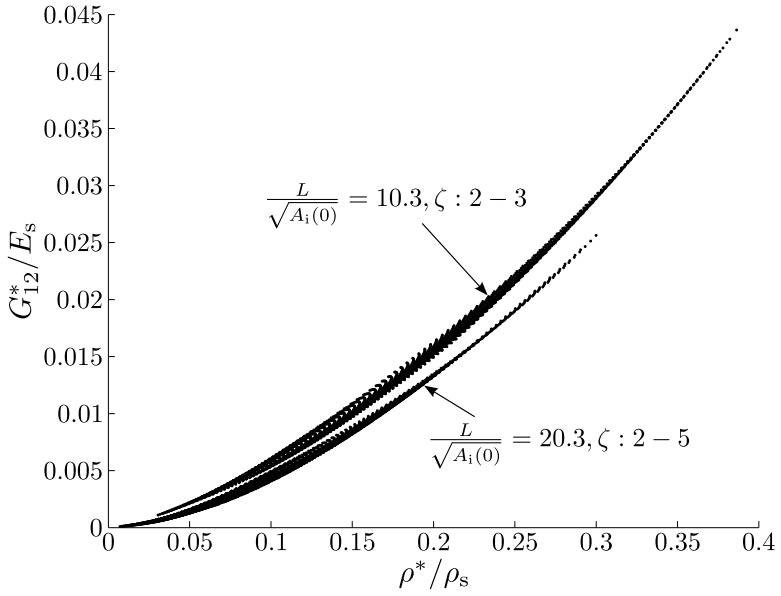


Figure 2.16: Relative density dependence of the relative shear modulus. The different curves are for different ligament $L/\sqrt{A_i(0)}$ ratios, and plotting the entire range of $\zeta$ and $\theta_o$ investigated. The "thickness" of the curves is attributable to varying $\zeta$ and $\theta_o$.

the variation between the sets is up to 49% and 12% at relative densities of 0.03 and 0.30, respectively. The maximum variation between the Poisson's ratio sets is 8% and 4% at relative densities of 0.03 and 0.30, respectively. As observed previously for other tetrakaidecahedron models, $\nu_{12}^*$ tends to 0.5 as the relative density tends to zero, and gradually decreases with increasing relative density.

Both sets of moduli data show a trend of relative modulus increasing with increasing relative density, as expected. The moduli are relatively insensitive to the particular $\zeta$ and $\theta_o$ chosen at any specific relative density. For fixed $L/\sqrt{A_i(0)}$ ratios, changes in the cross-sectional shape of the ligament only produce slight variations in the relative moduli, so the moduli in each set can be expressed solely as a function of relative density.

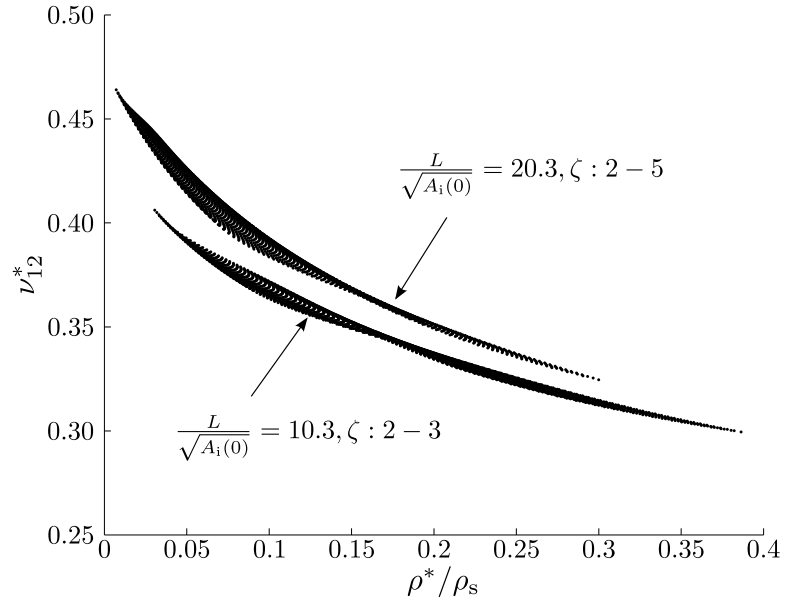


Figure 2.17: Relative density dependence of Poisson's ratio. The different curves are for different ligament $L/\sqrt{A_i(0)}$ ratios, and plotting the entire range of $\zeta$ and $\theta_o$ investigated. The "thickness" of the curves is attributable to varying $\zeta$ and $\theta_o$.

This insensitivity of the moduli to the specific cross-sectional shape is attributable to implicit constraints on the geometry of the ligaments. As shown in Fig. 2.14, each relative density corresponds to a locus of $\zeta$ and $\theta_o$ pairs, with limits on the ranges of $\zeta$ and $\theta_o$ that are possible. For example, using the 0.08 relative density contour in Fig. 2.14, $\zeta$ has a range of 2.2–5 and $\theta_o$ has a range of 7–90°. Meanwhile, the 0.18 relative density contour has a $\zeta$ range of 3.6–5 and a $\theta_o$ range of 45–90°. For any specific relative density chosen, the area and second moment of area of the ligament along the length of the ligament only changes by a small amount, as shown by example in Fig. 2.18 for the marked geometries in Fig. 2.14. These small variations in area and second moment of area are only capable of producing small variations in the ligament

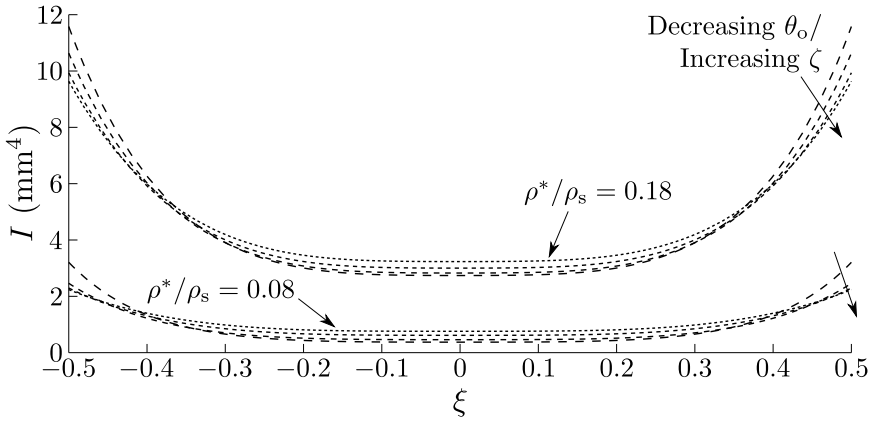


Figure 2.18: Second moment of area of the ligament along its nondimensionalized length. One set of curves is for relative densities of 0.08, and the other is for relative densities of 0.18. The $\zeta$ and $\theta_o$ pairs used to produce the individual curves are marked in Fig. 2.14.

Table 2.2: Fit constants for the power-law descriptions of relative moduli with respect to relative density

| $L/\sqrt{A_i(0)}$ | $C_1$ | $C_2$ |
|---|---|---|
| 20.3 | 0.346 | 0.161 |
| 10.3 | 0.396 | 0.188 |

deflections, and thus only small variations are seen in the resulting moduli calculated using Eqs. (2.25) and (2.29).

The two data sets in Figs. 2.15 and 2.16 are fit to the power-law functions in Eqs. (2.1) and (2.2) with fixed values of $n_1$ and $n_2$ using a least squares regression. The proportionality constants of the fits are listed in Table 2.2. An exponential constant of 1.55 was found to fit well for $n_1$ and $n_2$. For intermediate values of $L/\sqrt{A_i(0)}$, the curve fit proportionality constants can be linearly interpolated. For example, for an RPC with an $L/\sqrt{A_i(0)}$ ratio of 15.0 and a relative density of 0.20, the linearly interpolated constants in Eqs. (2.1) and (2.2) are $C_1 = 0.373$ and $C_2 = 0.175$. Application

of Eqs. (2.1) and (2.2) yield $E^*/E_s = 0.0308$ and $G^*/E_s = 0.0144$.

In order to validate the linear interpolation, moduli versus relative density data were generated using the model for geometries with an $L/\sqrt{A_i(0)}$ ratio of 15.0. The maximum differences between the curves fit to the model data and the linear interpolation curves over a range of relative densities of 0.03–0.30 are less than 1%.

The values in Table 2.2 are compared to fit constants of the previous analytical studies, and to fit constants of experimental data of RPCs for which sufficient data were provided such that power-law fits could be determined, in Table 2.1. Note that the fit constants in Table 2.2 are all lower than the fit constants of other analytical studies. This result is encouraging, because when compared to power-law curve fits of experimentally measured data by Hagiwara and Green [24] for alumina RPCs, the fit constants in the present study all fall within the 95% confidence intervals. This result shows an improvement in predictability over the available models that lack the shape details specific to RPC.

The analytically determined relative moduli of the present work are compared to measured values from the limited published experiments [23, 24, 31, 32] and our own measurements of cerium dioxide (ceria) RPC specimens with a ligament porosity of approximately 23% in Figs. 2.19 and 2.20. The ceria data were obtained from three-point flexural tests on RPC beam specimens,[8] and the ligament elastic modulus used for normalizing the measured values was obtained from a prior study [43]. The ceria

[8] Flexural test details are provided in Appendix A.

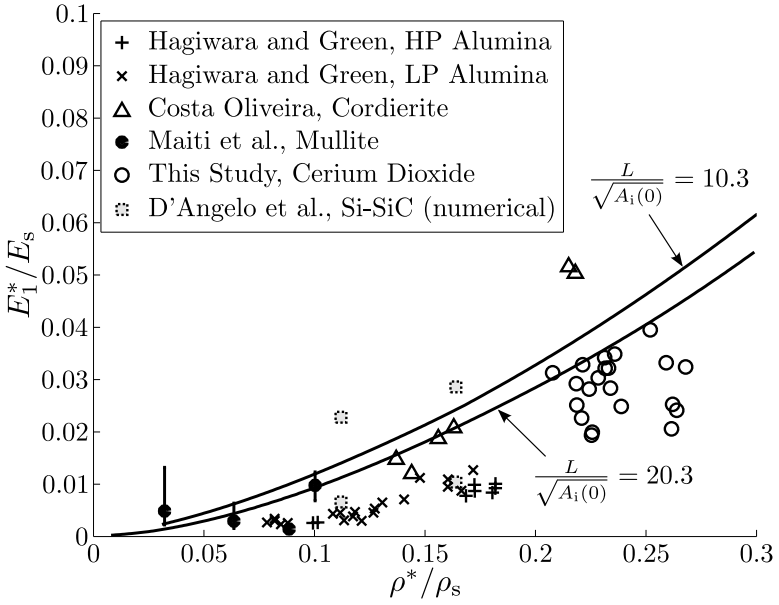


Figure 2.19: Relative density dependence of the relative elastic modulus. The different curves are for different ligament $L/\sqrt{A_i(0)}$ ratios. The +, ×, △, •, and □ symbols are data reported in the open literature for RPCs manufactured using the replication method [23, 24, 31, 32].

data fall both above and below the curve obtained for a normalized ligament length of 20.3. The scatter in the data is likely due to the random orientations of the ligaments in an actual RPC. While the model fit constants fall within the 95% confidence intervals of the alumina data obtained by Hagiwara and Green [24], the measured data are lower than the analytically predicted values for relative densities from 0.08 to 0.18. Some variation is expected, as the model assumes that RPCs are idealized periodic structures of ligaments, while the ligaments of actual RPCs may vary substantially from the ideal ones. The values of $E_s$ used to report data in the previous work may lead to additional discrepancies. Hagiwara and Green used the $E_s$ value of dense, pure, polycrystalline

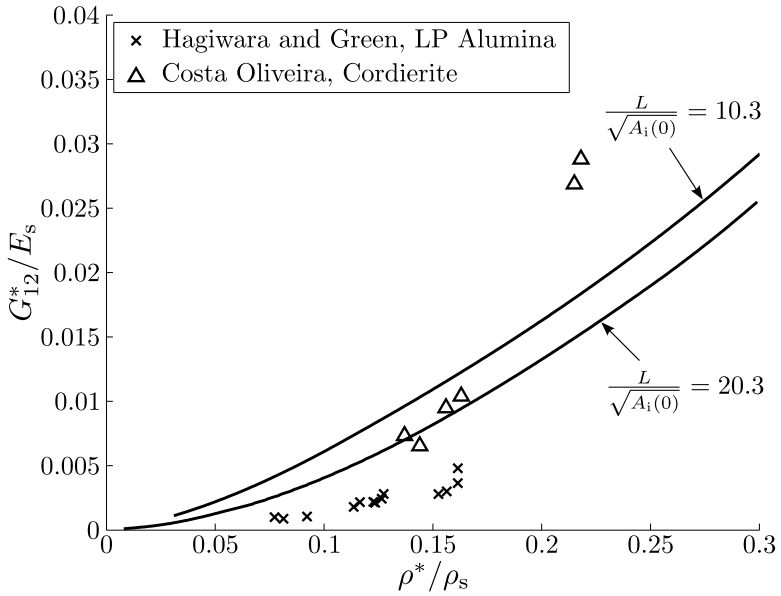


Figure 2.20: Relative density dependence of the relative shear modulus. The different curves are for different ligament $L/\sqrt{A_i(0)}$ ratios. The $\times$ and $\triangle$ symbols are data reported in the open literature for RPCs manufactured using the replication method [24, 31].

alumina in their normalization. However, they experimentally measured the moduli of both low purity (LP) and high purity (HP) alumina RPCs. In the case of the low purity alumina, which had a $ZrO_2$ content of greater than 5%, the authors noted that $ZrO_2$ is known to form microcracks in the material, which would cause the actual $E_s$ to be lower than $E_s$ of pure alumina. This, in turn, would cause the reported value of $E^*/E_s$ to be low. In the case of the high purity alumina, the ligaments were not completely sintered, as observed by heating the RPC specimens to progressively higher temperatures and recording the ligament densities. Incomplete sintering would again lead to an underestimation of relative elastic modulus.

The sparse data for relative elastic modulus from Costa Oliveira [31] for cordierite

and Maiti et al.[32] for mullite with relative densities less than 0.2 agree fairly well with the present model. The measured values are 40% higher than the analytically predicted elastic modulus for Costa Oliveira's high relative density material. This discrepancy is possibly due to closed cells existing within the RPC, which would tend to increase the elastic modulus of the foam. As the relative density increases, the frequency of closed cells in the foam and the thickness of the cell walls are likely to increase during the replication manufacturing process. These combined effects would produce a relative modulus curve with a larger exponential dependence on relative density.

The relative shear modulus plot shows exactly the same trends as are seen in the relative elastic modulus plot for the available data.

The data by D'Angelo et al. [23] highlight the variability possible from elongating the unit cell, yielding orthotropic cells rather than isotropic cells. Compression simulations were performed on finite element geometries created from X-ray computed tomography scans of Si-SiC RPCs. The results show that compression simulations performed with the cell elongation direction parallel to the load direction result in values higher than the model, while compression simulations performed with the elongation direction perpendicular to the load direction result in values lower than the model. Elongating a unit cell tends to increase the portion of the load that is supported axially, and decrease the portion of the load that is supported by bending, in the direction of elongation. Therefore the RPC appears stiffer in the direction of elongation. Based on these results, the model seems to accurately predict the result expected for RPCs with a cell structure

having no cell elongation.

When comparing the model results to data, the importance of quantifying the elastic modulus of the ligament material is apparent. This importance is driven by the fact that the foam properties are a function of the ligament properties. In a comparison of the model results to the experimental alumina RPC data and the numerical Si-SiC data, better agreement is observed with the numerical data in which the ligament elastic modulus used in normalization was a construct of the numerical simulation. This use of a known quantity for the normalization is in contrast to the experimental method where the elastic modulus for normalization is an estimation. Quantification of the ligament properties and characterization of the ligament morphology is frequently neglected when reporting experimental results of RPCs. Adding these additional details in future studies of RPC properties will improve the usefulness of these models.

## 2.6 Conclusions

This study derives a new model to predict the relative elastic and shear moduli of reticulated porous ceramics based on their microstructures. A tetrakaidecahedron is used as the unit cell to represent the RPC, with double Plateau border cross sections used to represent the shape of the ligament. Geometric parameters of the ligaments are varied, specifically the midplane thickness ratio $\zeta$, external-cusp half-angle $\theta_{\mathrm{o}}$, and normalized length $L/\sqrt{A_{\mathrm{i}}(0)}$, to determine what effect changing these parameters have on the relative moduli versus relative density relationship. While prior work found that changing

the shape of solid ligaments impacts the moduli of foamed materials [22, 25–27], changing the external shape of RPC ligaments with an internal void has little effect on the moduli. As a result, the particulars of the cross-sectional shape examined are not necessary to determine the relative moduli; only the relative density and normalized ligament length are needed. Changes to the normalized ligament length, $L/\sqrt{A_{\mathrm{i}}(0)}$, affect the moduli for a fixed relative density by 11–49%, with the percent difference decreasing with increasing relative density. Geometries with smaller normalized ligament lengths have larger moduli values.

## 2.7 Acknowledgments

This research was supported by the National Science Foundation (EFRI-1038307) and the University of Minnesota Initiative for Renewable Energy and the Environment. Parts of this work were carried out in the Characterization Facility, University of Minnesota, which receives partial support from NSF through the MRSEC program. The micrograph of RPC is courtesy of Peter Krenzke.

## 2.8 Nomenclature

$A$ Area, mm$^2$

$b$ Width of the ligament, mm

$C$ Fit constant

$C_{XYZ}$ Geometrical integral constant, $\mathrm{mm}^{-2}$ or $\mathrm{mm}^{-4}$

$c$ Half-distance between the Plateau border centroid and cusps, mm

$D_{\mathrm{J_T}}$ Nondimensionalized torsional constant ($J_{\mathrm{T}}/(2I)$)

$E$ Elastic modulus, MPa

$f$ Nondimensionalized area shape function ($A(\xi)/A(0)$)

$G$ Shear modulus, MPa

$I$ Second moment of area, $\mathrm{mm}^4$

$J_{\mathrm{T}}$ Torsional constant, $\mathrm{mm}^4$

$L$ Length of the ligament, mm

$M$ Bending moment, N mm

$m$ Mass, kg

$N$ Normal force, N

$n$ Fit constant

$P$ Force, N

$Q$ Statical moment of area, $\mathrm{mm}^3$

$R$ Radius of the Plateau border arc, mm

$T$ Torque, N mm

$t$ Distance between the internal and external cusps, mm

$U$ Strain energy, mJ

$u$ Displacement, mm

$V$ Shear force, N

$V$ Volume, $m^3$

$X$ Geometric integral constant alpha-variable

$x$ Axial position along the ligament, mm

$Y$ Geometric integral constant numeric-variable

$Z$ Geometric integral constant alpha-variable

## Greek Symbols

$\alpha$ Distance between the Plateau border centroid and arc center, mm

$\beta$ Shear form factor

$\Delta$ Displacement difference between nodes, mm

$\delta$ Displacement, mm

$\varepsilon$ Strain

| | |
|---|---|
| $\zeta$ | Midplane thickness ratio |
| $\theta$ | Plateau border cusp half-angle, $^\circ$ |
| $\nu$ | Poisson's ratio |
| $\xi$ | Nondimensionalized axial location ($x/L$) |
| $\rho$ | Density, kg m$^{-3}$ |

### Subscripts

| | |
|---|---|
| A | Node A |
| B | Node B |
| cube | Cubic unit cell |
| $i$ | Index |
| i | Internal Plateau border |
| o | External Plateau border |
| s | Ligament material |
| x | $x$-direction |
| y | $y$-direction |
| z | $z$-direction |

| | |
|---|---|
| 1 | 1-direction |
| 2 | 2-direction |
| 3 | 3-direction |

### Superscripts

| | |
|---|---|
| * | Foam |

# Chapter 3

# Mechanical Properties of Gelcast Cerium Dioxide From 23 to 1500 °C[1]

## 3.1 Summary

This work reports the elastic modulus and four-point flexural strength of a gelcast ceramic, cerium dioxide (ceria), with a microporosity of nominally 20% and a grain size of 11 $\mu$m from 23 to 1500 °C. The data augment the sparse data published for ceria and extend previous results by 150 °C. The ceria tested is representative of that constituting

[1] **This chapter is based on the article Stephen J. Sedler, Thomas R. Chase, and Jane H. Davidson. Mechanical Properties of Gelcast Cerium Dioxide From 23 to 1500 °C. Journal of Engineering Materials and Technology, 139(1):011008, January 2017. [DOI: 10.1115/1.4034925]**

the ligaments of a reticulated porous ceramic. The elastic modulus decreases from 90 GPa at 23 °C to 16 GPa at 1500 °C. The flexural strength is 78 MPa below 900 °C and then decreases rapidly to 5 MPa at 1500 °C. These trends are consistent with data reported for other ceramics. Comparing the measured elastic modulus to prior data obtained for lower porosity shows the minimum solid area (MSA) model can be used to extend the modulus data to other porosities. Similarly, the flexural strength data agree with prior data when the effects of specimen size, porosity, and grain size are taken into account.

## 3.2 Introduction

Cerium dioxide (ceria) is used in a variety of applications, including engine exhaust pollution control [1], wastewater treatment [2], thin film electrolytes within solid oxide fuel cells [3], and polishing materials [44]. Recently, ceria has been utilized in solar thermochemical reduction/oxidation (redox) cycles (for example, Refs. [4–6]). These cycles convert solar energy into chemical energy in the form of storable and transportable fuels. Ceria works well as a redox material because oxygen diffuses rapidly in its cubic fluorite crystal structure [45, 46], it does not undergo structural phase transitions between its fully oxidized and partially reduced forms, and it maintains stable rates of oxidation over hundreds of cycles at temperatures as high as 1500 °C [47–50]. The reduction step is endothermic and requires high temperatures (>1400 °C) and low-oxygen partial pressures. Thermodynamics shows the uptake of oxygen is improved in the

exothermic oxidation step by performing it at temperatures 200 to 400 °C cooler [51]. Therefore, in many reactors, the ceria substrate must withstand substantial thermal stresses attributable to the temperature difference between reduction and oxidation.

Reticulated porous ceramic foams (RPCs) are good candidates for the ceria substrate in redox cycles because they combine structural integrity with reasonably high-specific surface area and accessibility required for rapid mass transport and fuel production [14, 49, 52]. Several alternatives to RPCs have been considered, with some morphologies exhibiting better stability than others. Ceria monolith structures thermochemically cycled between 1500 °C and 800 °C experienced a three-fold increase in grain size [46]. Higher surface area materials such as three-dimensionally ordered macroporous ceria lost a large fraction of the surface area and pore volume at temperatures as low as 825 °C [53], and the ordered structure was lost completely after 1 h at 1250 °C [52, 54]. While electrospun ceria fibers cycled between 800 °C and 1500 °C maintained an open fibrous network up to 1400 °C [55], commercial ceria felts made with fibers exhibited significant sintering and shrinking in a prototype solar reactor [48]. Ceria particles made from fibers showed stable fuel production when isothermally cycled at 1500 °C [7, 8]. RPCs made from other materials are also used in a variety of other applications, for example, filtration [11], radiant burners [12], and bone tissue engineering [13].

The motivation for the work described here is the desire to design a free-standing cylinder of ceria RPC for use in a solar reactor where the cylinder is subjected to a temperature differential of up to 500 °C [9]. Data on the structural properties of

ceria (reviewed below) are sparse. The purpose of the present work is to fill a gap in the available data to enable analysis-driven design of ceria-based structures, especially those involving thermal stresses. While these data are essential for predicting the strength of ceria RPCs, the data are also necessary for modeling the strength of other ceria morphologies. The methods used to ensure that the specimens tested are representative of the ligaments of RPC are extensible to other ceramics commonly fabricated as RPCs, such as alumina.

Wachtel and Lubomirsky [56] summarize the state-of-the-art knowledge of the elastic modulus of pure and doped ceria. They comment on the difficulty of measuring the modulus at high temperatures and the limited availability of high-temperature data. The most complete data on elastic modulus as a function of temperature are reported by Wygant [29], where the data extend to 1300 °C. Unfortunately, the results are of limited usage, as the exact composition of the material, reported to be approximately 80% ceria, is not known. The elastic modulus at room temperature and 600 °C is reported by Sato et al. [34, 35]. Additional data at room temperature and different porosities are reported by Lipińska-Chwałek et al. [37] and Wang et al. [36]. These previous results are compared to the results reported here in Sec. 3.7. Nakajo et al. [57] provide limited data on the elastic modulus of gadolinia-doped ceria, but doped ceria cannot be directly compared to the undoped ceria tested in the present study.

The availability of flexural strength data is more limited still. Akopov and Poluboyarinov [30] present flexural strength data for ceria up to 1350 °C, but the details of the

experimental technique are not provided. The new data generated here are compared to available room temperature data of previous authors in Sec. 3.7.

Numerous studies have been performed to characterize the effect of nonstoichiometry on the mechanical properties of ceria-based oxides. Kossoy et al. [58] explore the effect of nonstoichiometry on the elastic modulus of thin film ceria, showing a decrease in modulus with an increase in chemical strain. Wang et al. [59] evaluate the effect of reduction on the room temperature flexural strength of ceria, observing a significant drop in strength with increasing nonstoichiometry. It should be noted that Wang et al. attribute some of the reduction in strength to internal stresses generated by having a highly reduced specimen surface with an unreduced interior below. Quantification of the impact of the gradient on the strength was not performed. In related work, Kaiser et al. [60] evaluated a doped ceria membrane for mechanical stability when subjected to a nonstoichiometry gradient across the thickness. Failure of the membrane occurred when relative chemical expansion exceeded a strain of 0.001. Various studies have investigated the effect of reduction on the chemical expansion of undoped and doped ceria [61–63]. The present study is restricted to $CeO_2$ and does not consider the impact of nonstoichiometry on mechanical properties.

This work reports the elastic modulus and four-point flexural strength of a gelcast ceria, with a microporosity of nominally 20% and a grain size of 11 $\mu$m from 23 to 1500 °C. The procedure used to fabricate test specimens with morphology similar to the material constituting ligaments of RPC is presented in Sec. 3.3. The experimental

methods are described in Sec. 3.4. The results for the elastic modulus and flexural strength up to 1500 °C are presented in Sec. 3.5. Extending these results to RPC is discussed in Sec. 3.6. The results are compared to previous work in Sec. 3.7. Conclusions are drawn in Sec. 3.8.

## 3.3 Test Specimen Fabrication

Flexural test specimens were fabricated which conform to size "B" specimens of ASTM Standard C1211 [64]. They were fabricated by gelcasting, a near-net-shape manufacturing process for ceramics which can yield strong, dense, and defect-free parts [65, 66]. Gelcasting was chosen over alternative forming processes because the processing steps are the most similar to those used for RPCs. In particular, both methods utilize pressureless sintering. In contrast, alternatives such as extruding and pressing introduce high pressures that are likely to yield different porosities, pore shapes, and grain sizes. The pore shape and grain size of the specimens are further explored in Sec. 3.6.

The gelcast process used ceria powder (Alfa Aesar, 99.9% $CeO_2$) with a $D_{50}$ particle diameter of $\sim$5 $\mu$m measured using the SediGraph technique [67]. To reduce warping, the bars were fired in a tunnel kiln at a temperature of 1580 °C for 6 h, turned upside down, then fired for another 6 h at 1580 °C. The final firing temperature was set 80 °C above the highest test temperature to minimize any changes to the microstructure attributable to sintering. The nominal dimensions of the specimens, as fired, were 3.5 mm $\times$ 4.5 mm $\times$ 45 mm. The bars were then ground to their finished 3 mm

$\times$ 4 mm cross-sectional dimensions with a parallelism tolerance of 0.015 mm on the longitudinal faces, as specified in the ASTM standard [64].

The porosity, $P$, of the test specimens was calculated as:

$$P = 1 - \frac{m/(hwL)}{\rho} \tag{3.1}$$

where $m$ is the mass of the specimen, $\rho$ is the density of ceria (7.65 g/cm$^3$ [68]), and $h$, $w$, and $L$ are the height, width, and length, respectively, of the specimens. The mass of each specimen was measured using a mass balance with a resolution of 0.001 g (Sartorius, GD-503-NTEP). The height, width, and length of each specimen were measured using calipers having a readout resolution of 0.01 mm (General, 147). The average porosity of the test specimens is $0.21 \pm 0.02$.

## 3.4 Experimental Methods

All testing was done in accordance with ASTM Standard C1211 [64]. The test specimens described in Sec. 3.3 were loaded in a fully articulated, silicon carbide, four-point, ¼-point, size B flexure fixture [64]. The fixture has a load span of 20 mm and a support span of 40 mm, with load point diameters of 4.8 mm.

A standard universal tester (Instron, Model 55R1123) was used to load the specimens with a constant displacement rate of 0.51 mm/min (0.020 in./min). A high-crosshead displacement rate was used to reduce any effects attributable to creep. The time,

Table 3.1: Number of specimens tested at each temperature

| *Temperature (°C)* | 23 | 500 | 800 | 1000 | 1200 | 1300 | 1400 | 1500 |
|---|---|---|---|---|---|---|---|---|
| *No. of specimens* | 3 | 3 | 5 | 5 | 3 | 3 | 3 | 3 |

crosshead displacement, and load were recorded at a rate of 20 Hz.

The elastic modulus and the flexural strength are deduced from the recorded test data using beam bending equations, rearranged to solve for the value of interest [69]. The elastic modulus, $E$, is

$$E = \frac{(L_\mathrm{o} - L_\mathrm{i})^2(L_\mathrm{o} + 2L_\mathrm{i})}{4wh^3} \times \frac{\Delta F}{\Delta \delta_\mathrm{crosshead}} \tag{3.2}$$

where $L_\mathrm{o}$ is the support span of the test fixture and $L_\mathrm{i}$ is the load span. Only the linear portion of the applied force, $F$, versus the crosshead displacement, $\delta_\mathrm{crosshead}$, curve is used. The flexural strength, $\sigma_\mathrm{fs}$, is

$$\sigma_\mathrm{fs} = \frac{3F_\mathrm{max}(L_\mathrm{o} - L_\mathrm{i})}{2wh^2} \tag{3.3}$$

where $F_\mathrm{max}$ is the maximum total load applied to the specimen.

Multiple specimens were tested at several different temperatures between room temperature (nominally 23 °C) and 1500 °C. The number of specimens tested at each temperature is listed in Table 3.1. As the specimens exhibited a variation in porosity of $\pm 0.02$, they were distributed across the range of testing temperatures to equalize the porosity of the specimens in every range to the extent possible.

For tests above room temperature, the specimen and the fixture were heated at a rate of 10 °C/min in a clamshell furnace. Temperatures were measured using a Type R thermocouple positioned about 3 mm from the specimen. Once the temperature set point was reached, a 15 min soak was employed. All tests were performed at ambient atmospheric conditions. Based on the data from Panlener et al. [51], the equilibrium nonstoichiometry of ceria in air at 1500 °C would be less than 0.001, and thus the chemical strain would be less than 0.0001 based on the chemical expansion versus nonstoichiometry relationship developed by Bishop et al. [61]. This chemical strain is equivalent to the thermal expansion of ceria with a rise in temperature of approximately 10 °C [70]. As such, the chemical strains of the ceria in this study are negligible compared to the thermal strains.

## 3.5 Results

The measured elastic moduli of the gelcast ceria test specimens for temperatures from 23 to 1500 °C are plotted in Fig. 3.1. At room temperature, the elastic modulus of the gelcast ceria has a mean of 90 GPa with a standard deviation of ±4 GPa. The modulus decreases with increasing temperature to $16 \pm 2$ GPa at 1500 °C, with the reduction in modulus caused by a decrease in interatomic bonding force between ceria atoms. The measured moduli exhibit larger scatter in the data at intermediate temperatures, with a standard deviation of ±10 GPa at 800 and 1000 °C, and ±7 GPa at 500 °C.

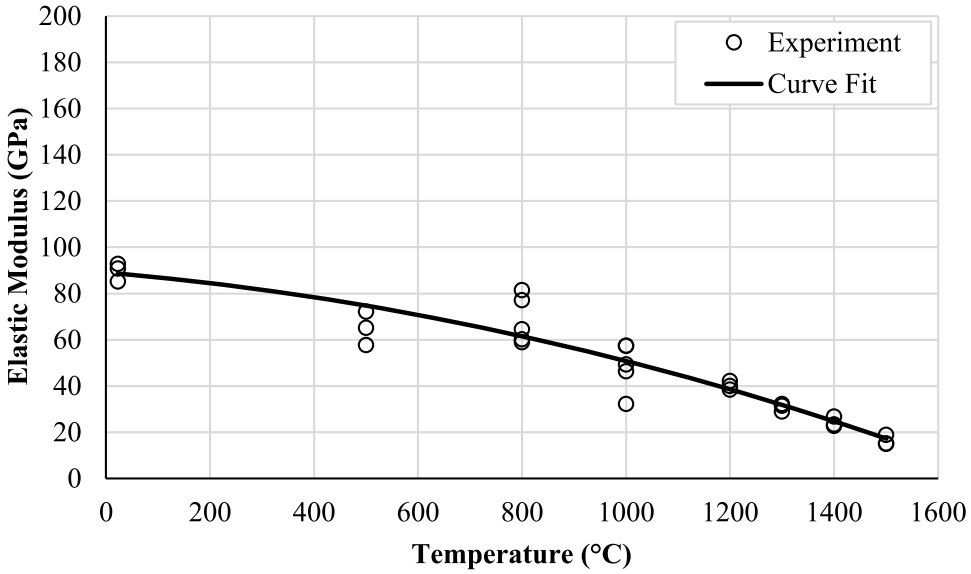


Figure 3.1: Measured elastic moduli of gelcast ceria from 23 to 1500 °C. The data obtained in the current study have a maximum measurement error of ±2.9 GPa based on specimen dimensions and load cell uncertainty. Error bars are not shown because they span only within the markers. The curve fit to the data is represented by Eq. (3.4).

A curve having the following form was fit to the experimental data for elastic modulus using a least squares regression:

$$E = -1.92 \times 10^{-5} T^2 - 0.0191T + 89.0 \quad \text{(GPa)} \tag{3.4}$$

where $T$ is the temperature in °C. The large scatter of the data in the 500–1000 °C range leads to a coefficient of determination for the curve fit, $R^2$, of 0.948. The result is shown as a solid curve in Fig. 3.1.

Some nonlinear effects were observed in the 1400 and 1500 °C data sets just prior to failure, where the failure mode changed from brittle to plastic. Creep does not impact

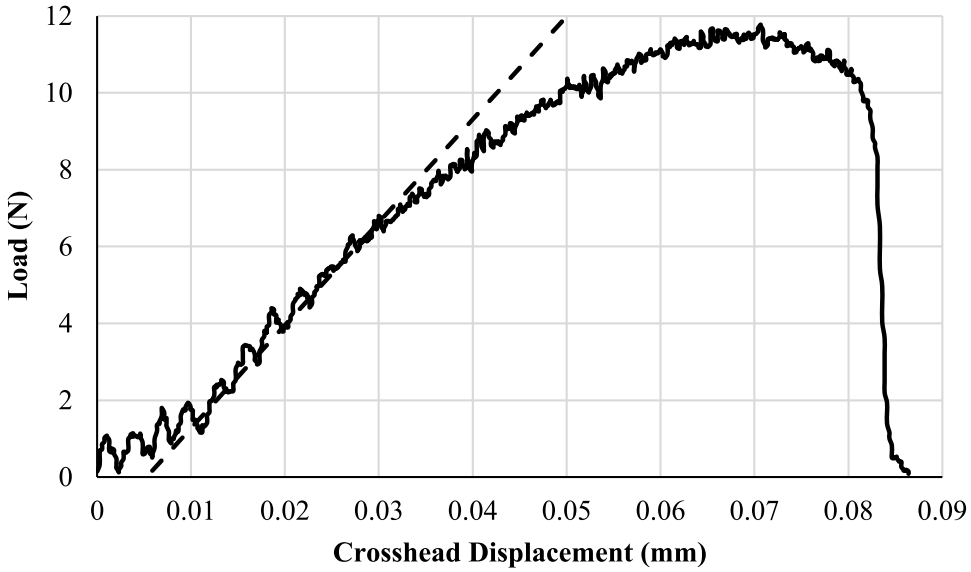


Figure 3.2: Load versus crosshead displacement curve for one of the specimens tested at 1500 °C. Note the non-linear behavior in the region of the maximum load. The superimposed line is based on the $E$ value deduced from this curve.

the data. Based on ceria creep characterizations performed by Lipińska-Chwałek et al. [71], the creep rate is less than 1% strain per year when calculated at conditions of 1500 °C and a stress of 5 MPa. An example of the nonlinear effect is shown in Fig. 3.2. The slope of the linear portion of the curve was used to determine the elastic modulus, as indicated in the figure.

The measured flexural strength of the gelcast ceria from 23 to 1500 °C is shown in Fig. 3.3. The mean flexural strength is $78 \pm 6$ MPa at 23 °C. The strength is relatively stable until 900 °C. Thereafter, it decreases dramatically with increasing temperature. The flexural strength is $5 \pm 4$ MPa at 1500 °C. Like the elastic modulus, the measured flexural strength has more scatter at the intermediate temperatures. The standard

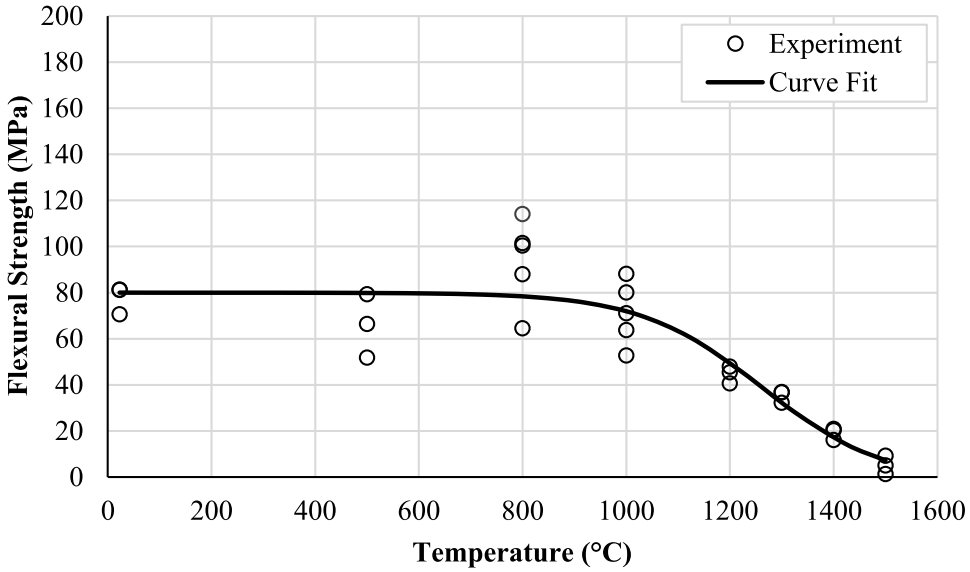


Figure 3.3: Measured flexural strength along with a curve fit to the experimental data using Eq. 3.5. The data obtained in the present study have a maximum measurement error of ±1.8 MPa. Error bars are not shown because they span only within the markers.

deviation is ±14 MPa at 500 and 1000 °C, and ±19 MPa at 800 °C. At low temperatures, the feature limiting the strength of the specimen is expected to be the size of the critical flaw, namely an existing pore in the specimen. At elevated temperatures, failure is attributed to subcritical cracks propagating into a critical flaw [72]. This change in failure mechanism dictates the shape of the strength curve.

A curve having the following form was fit to the data for flexural strength using a least squares regression:

$$\sigma_{\text{fs}} = 80.1 - \frac{82.6}{1 + 4.33 \times 10^4 e^{-0.00845T}} \quad \text{(MPa)} \tag{3.5}$$

The form of the curve is that used by Munro for the flexural strength of alumina [73].

The coefficient of determination for the curve fit is 0.808. The resulting curve is shown superimposed on the experimental data in Fig. 3.3.

## 3.6 Extension of the Results to RPCs

The results reported in Sec. 3.5 are general, i.e., they are not limited to RPCs. Nevertheless, the immediate motivation for obtaining these results was to predict the mechanical properties of RPCs. Extending these results to RPCs is discussed here.

The mechanical properties of RPCs relevant to this study are described in Sec. 3.6.1. The methods applied to ensure that the flexural test specimens are representative of the material constituting the ligaments of a ceria RPC are described in Sec. 3.6.2. These methods are extensible to RPCs fabricated from other materials.

### 3.6.1 Porosity, Elastic Modulus, and Flexural Strength of RPCs.

The image in Fig. 3.4 is of an RPC fabricated using the replication method [15, 16], where a polyurethane foam is immersed in a ceramic slurry, purged of excess slurry, and fired at high temperatures to volatilize the foam and sinter the ceramic. The result of the process is an open-cell structure made of a series of interconnected ceramic ligaments, as illustrated in Fig. 3.4. Depending on the slurry constituents, firing temperature, heating rate, and processing steps, varying degrees of porosity can be obtained both at the macroscopic and microscopic levels [16, 17, 74]. The dual-scale porosity of the RPC is clarified in Fig. 3.5.

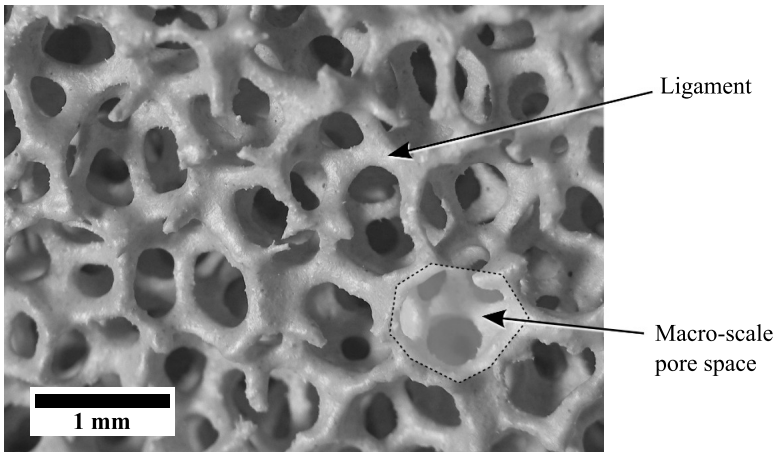


Figure 3.4: Ceria RPC consisting of a series of interconnected ligaments and macroscale pore spaces

RPCs are generally described in terms of their macroscopic porosity, $P_{\mathrm{RPC}}$, and linear macroscale pore density, $\lambda_{\mathrm{P}}$, generally given as pores per inch (ppi) (e.g. Ref. [75]):

$$P_{\mathrm{RPC}} = 1 - \frac{\rho^*}{\rho_{\mathrm{s}}} \tag{3.6}$$

$$\lambda_{\mathrm{P}} = \frac{N}{L_{\mathrm{P}}} \tag{3.7}$$

where $\rho^*$ is the effective density of the RPC, $\rho_{\mathrm{s}}$ is the density of the material from which the ligaments are constructed, and $N$ is the number of macroscopic pores within the RPC that are intersected by a straight line of a known length, $L_{\mathrm{P}}$. The macroscale pore density of the RPC illustrated in Fig. 3.4 is determined by the 30 ppi polyurethane foam used to fabricate it.

Analytical and semi-empirical models have been developed that relate the macroscale

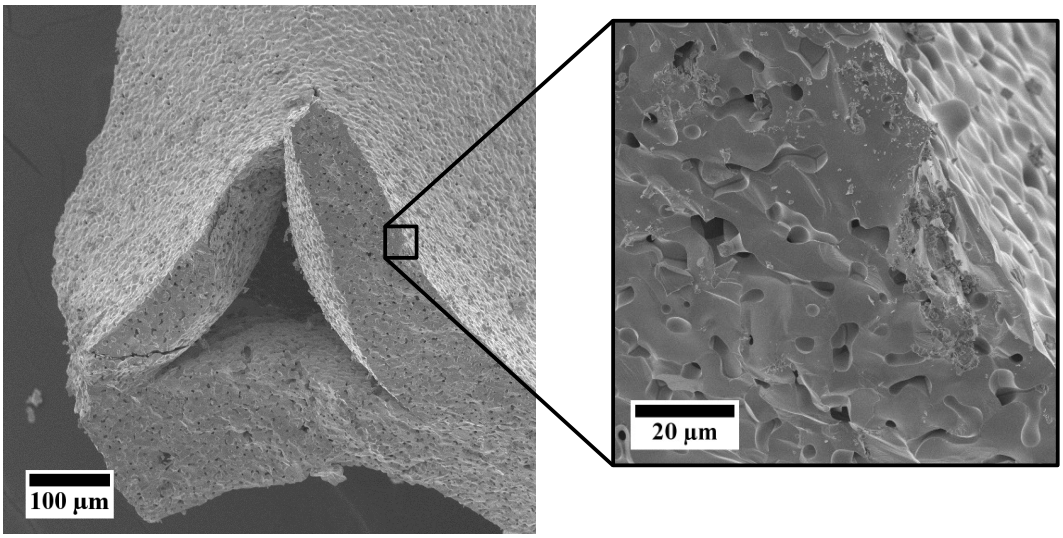


Figure 3.5: Scanning electron micrographs of a broken ligament of a ceria RPC. The internal void, having the shape of a Plateau border [20], constitutes a macroscale feature; e.g., the porosity of the ligament material does not include this void. The inset micrograph clarifies the microscale porosity of the ligament material.

properties of foam materials to the microscale properties of the constituent materials [22, 28, 76–78]. Gibson and Ashby [28] developed a power law relationship between the modulus and the density based on a staggered cubic structure of ligaments

$$\frac{E^*}{E_\mathrm{s}} = C\left(\frac{\rho^*}{\rho_\mathrm{s}}\right)^n \tag{3.8}$$

where $E^*$ is the effective elastic modulus of the foam, $E_\mathrm{s}$ is the elastic modulus of the material constituting the ligaments, and $C$ and $n$ are empirically fit constants. Hagiwara and Green [24] found that this model provided a good fit for the elastic modulus of alumina RPC using constants of $C = 0.3$ and $n = 1.93$. The elastic modulus reported in Sec. 3.5 constitutes $E_\mathrm{s}$. The relative flexural strength of ceramic foams can also be

predicted by substituting the strengths for the moduli in Eq. (3.8) [79, 80]. Therefore, Eq. (3.8) can be used to extend the results reported here to ceria RPC.

### 3.6.2 Comparison of Test Specimens With RPC Ligaments.

Several attributes of the morphology of the test specimens were analyzed to demonstrate that they are representative of those in ceria RPC ligaments. These attributes include area porosity fraction, pore density, pore area on a cross section, pore roundness, and grain size. These attributes were also measured in a test specimen taken to 1500 °C then cooled to room temperature, to confirm that exposure to the maximum temperature considered in this study did not change the morphology of the specimen.

The material morphology was quantified by photographing the microstructure of specimens, then processing the resulting images. One specimen was selected for each sample type: RPC ligament, room temperature test specimen, and a test specimen that had been taken to 1500 °C. Each specimen was potted in a cylindrical mold of epoxy (Buehler, EpoThin2). As the porosity of the test specimens varied slightly between specimens, those that were potted were selected to have porosity as close as possible to the average value. The potted specimens were ground and polished on one face. A series of images of the polished surface of each specimen was obtained using a visual microscope (Nikon, Optiphot) and digital camera (Canon, SL1), thereby giving a visual representation of one cross section through each specimen. One such image is shown in Fig. 3.6(a), where the light areas of the image are ceria and the dark areas the pore

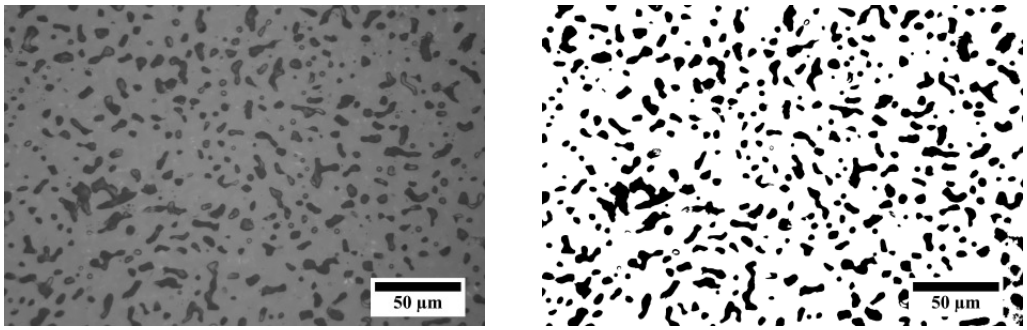


(a) (b)

Figure 3.6: Example microstructure of a ceria test specimen that was not heated beyond room temperature following fabrication. (a) Photographic image of the polished cross section and (b) thresholded mask of the cross section shown in Fig. 3.6(a).

space. Thresholding was performed on the cross-sectional specimen images using an image processing program (NIH, ImageJ) to highlight the pores within the specimens. A sample result of this process is illustrated in Fig. 3.6(b).

The area porosity fraction was determined by dividing the total highlighted pore area on a designated area by the enclosing area. If one assumes that the pores are uniformly distributed in the material, then the area porosity fraction is the same as the porosity. Based on an analysis of 31 images of the test specimen tested at 23 °C, the average porosity is 0.20, with a standard deviation of 0.01. This value is in agreement with the measured porosity of $0.21 \pm 0.02$ (see Sec. 3.3). The area porosity fraction of the gelcast sample is close to the target value measured for the RPC (based on eight images): $0.23 \pm 0.02$.

The pore density was estimated by counting the number of pores appearing in the imaged areas. The pore density of the gelcast material (8100 pores/mm$^2$) is about 40%

higher than the RPC (5800 pores/mm$^2$). However, as noted below, the pores in the gelcast specimen are smaller than those in the RPC, yielding similar overall porosity.

Pore area on a cross section examines the area of each pore on the polished face of each specimen. The pore area is only an approximate measure, as the pores are actually three-dimensional ellipsoids having irregular shapes. The area produced by each pore on an intersecting plane will depend on the position and orientation of the plane relative to each pore. Nevertheless, the overall pore area distributions are expected to follow the same general trends for similar materials.

A histogram of the pore areas on the imaged surface of each specimen type is shown in Fig. 3.7. The area of the room temperature gelcast specimen inspected included 12,989 pores, while the areas of the 1500 °C gelcast specimen and the RPC specimen included 10,318 and 1999 pores, respectively. The area distributions for the two gelcast specimens are very similar. The pore areas for the RPC specimen are somewhat larger but cover an overall range similar to the gelcast specimens. The average pore area for the RPC specimen is 40 $\mu$m$^2$, about 1.6 times the average pore area for the gelcast specimens of 25 $\mu$m$^2$.

Determining the roundness of each pore was initiated by best fitting an ellipse to each pore using the image processing software. “Best fit” is defined as matching the area and centroid of the ellipse with the area of the dark pixels defining the pore, respectively, then solving for the orientation, major axis length, and minor axis length using a Newton-based Pratt fit [81]. Examples of how ellipses are fit to the pores on

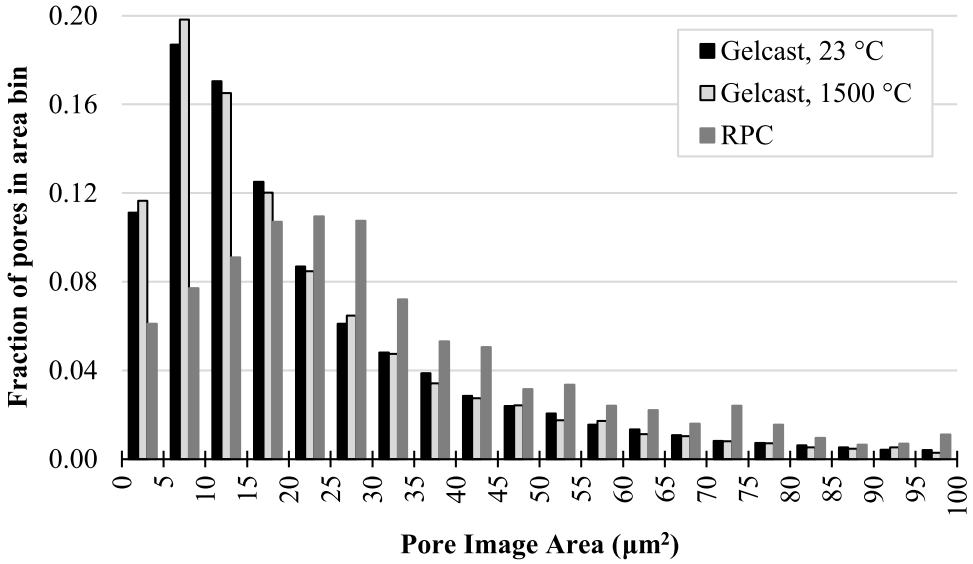


Figure 3.7: Histogram of pores' areas on the imaged cross section of each specimen type. The tail of the histogram is cut off since all pore area bins greater than 100 $\mu$m$^2$ have frequencies less than 0.01.

the imaged surfaces are illustrated in Fig. 3.8. Once the ellipse is fit, the roundness of the pore is calculated as

$$\text{Roundness} = \frac{\beta}{\alpha} \tag{3.9}$$

where $\alpha$ and $\beta$ are the length of the major and minor axes, respectively, of the best fit ellipse. Roundness values of unity indicate perfectly circular pore areas with decreasing roundness values indicating elongated pore areas. As with pore area on a cross section, pore roundness is an approximate measure, since the roundness of the pores will vary depending on the position and orientation of the intersecting plane.

A histogram of the pore roundness corresponding to the imaged surface of each specimen type is shown in Fig. 3.9. The same pores used to calculate the area porosity

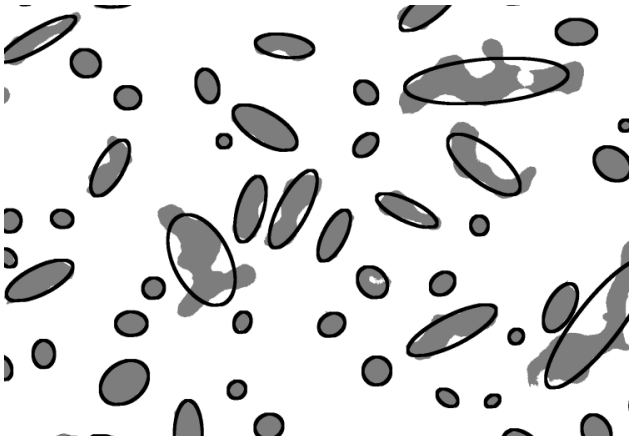

Figure 3.8: Examples of fitting ellipses to pore areas. For each pore area, the best fit ellipse axes' lengths and orientation are determined using a Newton-based Pratt fit [81].

fraction were used here. All specimens show a similar trend: the frequency of pores with improving roundness increases to roundness of 0.85–0.90, then drop in the final bins. We conclude that the pore shapes are similar between all specimens.

The average grain size of each test specimen was determined visually using the linear intercept method [82]. The polished face of each specimen was chemically etched at room temperature in a solution of 50% $H_2O$, 45% $HNO_3$ (70%), and 5% HF (49%) for 1 h to expose the grain boundaries. The faces were then rephotographed in the same manner as was done for the pore analysis. An example of the grain boundaries in the room temperature test specimens is provided in Fig. 3.10. The grains have approximately the same average size of 11 $\mu$m in all samples.

The morphological attributes of the test specimen taken to 1500 °C are all very close to the values measured for the test specimen that was not heated beyond room temperature following firing. From this result, we conclude that the morphology of the

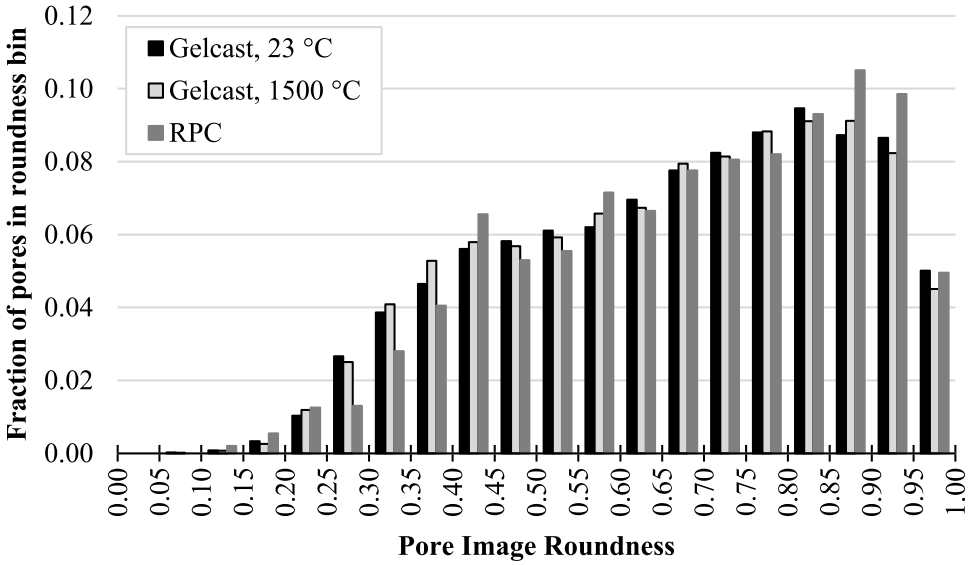


Figure 3.9: Histogram of pore roundness measured in each specimen type

gelcast specimens did not change as a result of heating to 1500 °C. Therefore, it appears that the gelcast material did not densify at high temperatures.

The results of comparing the gelcast ceria test specimens with the material comprising the ligaments of a ceria RPC are summarized in Table 3.2. The gelcast ceria test specimens are representative of the material comprising the ligaments of the ceria RPC. The grain size is approximately the same between materials. While the pores in the RPC are somewhat larger, the RPC also has fewer pores, so that the overall porosity of the test specimens and RPC samples agree to within about $\pm 0.02$. The average pore roundnesses of the test samples are also similar, with similar roundness distributions. Raising a test sample to 1500 °C did not appear to change its morphology.

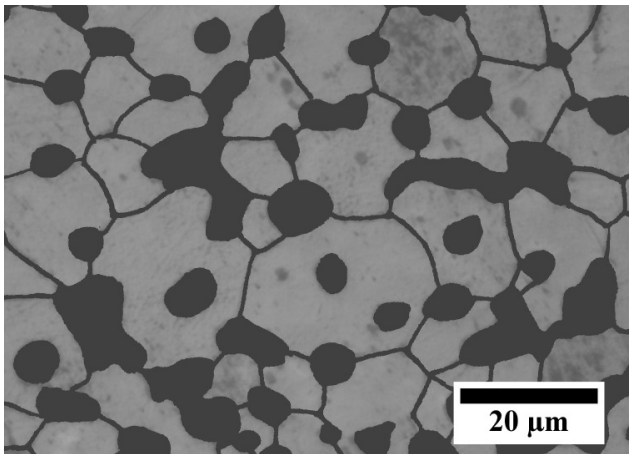


Figure 3.10: Image of a polished cross section of gelcast ceria after chemical etching to reveal the grain boundaries. The grain boundaries have been emphasized for clarity.

Table 3.2: Summary table of the morphological attributes measured for the ligaments in ceria RPC, the gelcast test specimens at room temperature, and the gelcast test specimens taken to 1500 °C and then cooled to room temperature. The porosity of the original gelcast test specimens is also included.

| *Specimen* | *Porosity* | *Average porosity fraction* | *Pore density (pores/mm$^2$)* | *Average pore area ($\mu m^2$)* | *Average pore roundness* | *Average grain size ($\mu m$)* |
|---|---|---|---|---|---|---|
| RPC | N/A | $0.23 \pm 0.02$ | 5800 | 30 | 0.68 | $11 \pm 1$ |
| Gelcast, 23 °C | $0.21 \pm 0.02$ | $0.20 \pm 0.01$ | 8100 | 23 | 0.67 | $11 \pm 2$ |
| Gelcast, 1500 °C | N/A | $0.21 \pm 0.02$ | 8300 | 23 | 0.66 | $11 \pm 1$ |

## 3.7 Discussion

The results for elastic moduli and flexural strength are demonstrated to be reasonably consistent with those in the literature. While data are limited for pure ceria at high temperatures, baseline comparisons are made to available room temperature data.

The effect of porosity must be considered to compare the data measured in this work with those in the literature. The minimum solid area (MSA) model is a widely accepted

approach for accommodating the effects of both porosity and pore shape [33]

$$\frac{X}{X_0} = e^{-bP} \tag{3.10}$$

where $X$ is the porous material property of interest, $X_0$ is the corresponding property of the nonporous material, and $b$ is an empirical constant related to the property of interest and pore shape. For porous media manufactured using pressed and colloidal processing techniques and having random pore stacking, the $b$-values are typically between 3 (representative of cubic stacking of spherical pores) and 5 (representative of cubic stacking of spherical solids) [33, 83, 84]. Similarly, two materials, A and B, of different porosity can be compared as

$$\frac{X_{\mathrm{A}}}{X_{\mathrm{B}}} = e^{-b(P_{\mathrm{A}} - P_{\mathrm{B}})} \tag{3.11}$$

Figure 3.11 illustrates published elastic modulus data for less porous [29, 34–36] and more porous [37] ceria, formed by pressing, superimposed on the new data for gelcast ceria. All values from the literature are adjusted to an equivalent 0.20 porosity by applying Eq. (3.11). Using a $b$-value of 3.0 in Eq. (3.11) produces good agreement with the data obtained in the present study and the literature values obtained using bulk measurement methods (see Fig. 3.11).

The elastic moduli at room temperature nominally agree between this study, Sato et al. [34, 35], and Wygant [29]. However, the moduli of Lipińska-Chwałek et al. [37] and

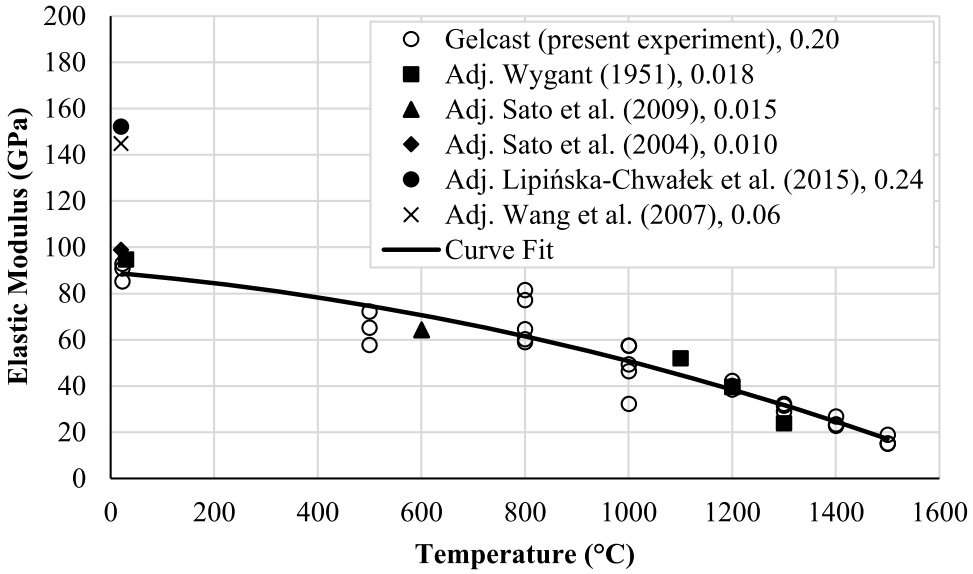


Figure 3.11: Comparison of elastic moduli for ceria from different sources. Published data from Wygant [29] (calculated assuming Poisson's ratio of 0.3), Sato et al. [34, 35] Lipińska-Chwałek et al. [37], and Wang et al. [36] are shown superimposed on the data generated in the present study. The values from the literature are adjusted to an equivalent porosity of 0.20 using Eq. (3.11) with $b = 3.0$. (A base porosity value of zero was used instead of the specimen porosity of 0.06 for Wang et al. [36] because they used nanoindentation and the indents fell entirely within single grains.) The original specimen porosities are shown in the legend. The curve fit to the data for gelcast ceria (Eq. (3.4)) is also shown.

Wang et al. [36] are approximately 50% higher. The difference is attributed to the methods used to measure the moduli. The first group of authors used "bulk measurement" techniques: flexural tests or the "small punch" method [34, 35]. The second group used indentation techniques. This discrepancy is consistent with variability observed by Radovic et al. [85] and Wachtel and Lubomirsky [56] when comparing different elastic modulus measurement techniques.

The probability of failure of a ceria specimen is assumed to follow a Weibull distribution [86]

$$P_{\mathrm{f}} = 1 - e^{-(\sigma/\sigma_0)^m} \tag{3.12}$$

where $P_{\mathrm{f}}$ is the probability of failure, $\sigma$ is the stress at failure of an individual specimen, $\sigma_0$ is the characteristic strength, and $m$ is the Weibull modulus. Note from Fig. 3.3 that the strength of the ceria specimens tested here stays nominally constant from room temperature through 800 °C. Therefore, the Weibull modulus is estimated using all of the available data points in that range. The nominal Weibull constants are $m = 4.9$ and $\sigma_0 = 88.7$ MPa. Note that the Weibull modulus indicates high variability in the data. The limits of the 90% confidence interval on the Weibull modulus corresponding to the 11 available data points [87] are

$$2.8 \leq m \leq 6.5 \tag{3.13}$$

The probability of failure may be related to either an effective volume, if the predominant flaw type is volume-distributed, or an effective area, if the predominant flaw type is surface-distributed [88]. Fractographic analysis was performed on the failed test specimens. For specimens tested up to 1300 °C, fractures originated at both surface and subsurface pores. (The fracture origin could not be determined for the samples tested above 1300 °C.) An image of a fracture surface with a subsurface fracture origin is shown in Fig. 3.12. As a result of some failures originating at subsurface pores, the

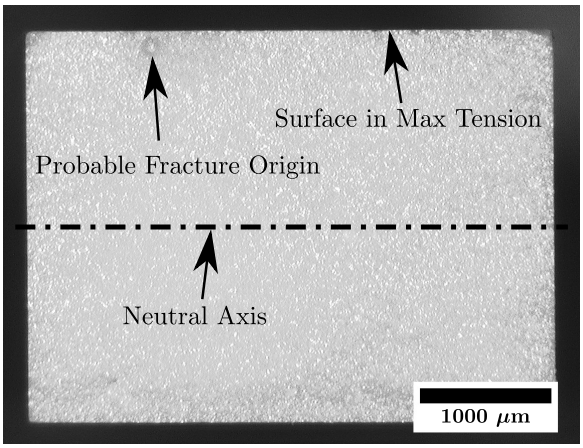


Figure 3.12: Fracture surface of an example flexural specimen tested at 1200 °C with a subsurface fracture origin. The top edge of the cross section in this photo was in the surface under tension during the test.

strength is assumed to scale with effective volume [89]

$$\frac{\sigma_1}{\sigma_2} = \left(\frac{V_{\mathrm{E},2}}{V_{\mathrm{E},1}}\right)^{1/m} \tag{3.14}$$

Equation (3.14) enables comparing the strengths of specimens having different sizes and loading geometries. In addition, specimen strength is expected to depend on porosity and grain size. Porosity is accounted for using Eq. (3.11). The Hall–Petch relationship [90, 91] can account for grain size; the general trend of the relationship shows decreasing strength with increasing grain size.

The room temperature flexural strength from previous studies of undoped ceria is summarized in Table 3.3. It is not possible to directly compare the results obtained here with Akopov and Poluboyarinov [30] nor Maschio et al. [38] because of missing

Table 3.3: Specifications of specimen characteristics and results for previous studies of the flexural strength of undoped ceria. All specimens are loaded in four-point flexure, except for Akopov and Poluboyarinov for which loading was unspecified. "?" symbols indicate values not specified in the reference.

| *Author* | *Volume ($h \times w \times L_o$, mm)* | *Loading* | *Porosity* | *Average grain size ($\mu m$)* | *Flexural strength (MPa)* |
|---|---|---|---|---|---|
| This Study | 3×4×40 | ¼-point | 0.20 | 11 | $78 \pm 6$ |
| Akopov and Poluboyarinov [30] | 4×4×? | ? | 0.04–0.05 | ? | 139 |
| Maschio et al. [38] | ?×?×30 | ⅓-point | 0.06 | 3.5 | 85 |
| Wang et al. [59] | 2.6×4×30 | ⅓-point | 0.04–0.06 | 24 | $113 \pm 19$ |
| Cutler and Meixner [92] | 3×4×40 | ¼-point | 0.03–0.17 | ? | $148 \pm 7$ |

information about the specimens or test procedures. Nevertheless, Akopov and Poluboyarinov provide the only published data on the high-temperature strength of ceria. A qualitative comparison between our results and theirs is performed by normalizing the flexural strength versus temperature data of each study, dividing the data by the average room temperature strength (see Fig. 3.13). Comparison is difficult due to the gap in their data between room temperature and 800 °C. However, their strength data appear to start decreasing at a lower temperature than was observed in our tests.

The remaining strength data were obtained at room temperature. The flexural strength of Wang et al. [59] shows substantial scatter. Equation (3.11) is applied to adjust to an equivalent porosity of 0.20 using a $b$-value of 3.0. A lower bound of 58 MPa is obtained by applying a porosity of 0.04 to the lower bound of measured flexural strength, and an upper bound of 87 MPa is obtained by applying a porosity of 0.06 to the upper bound of measured flexural strength. The effective volume for their ⅓-point

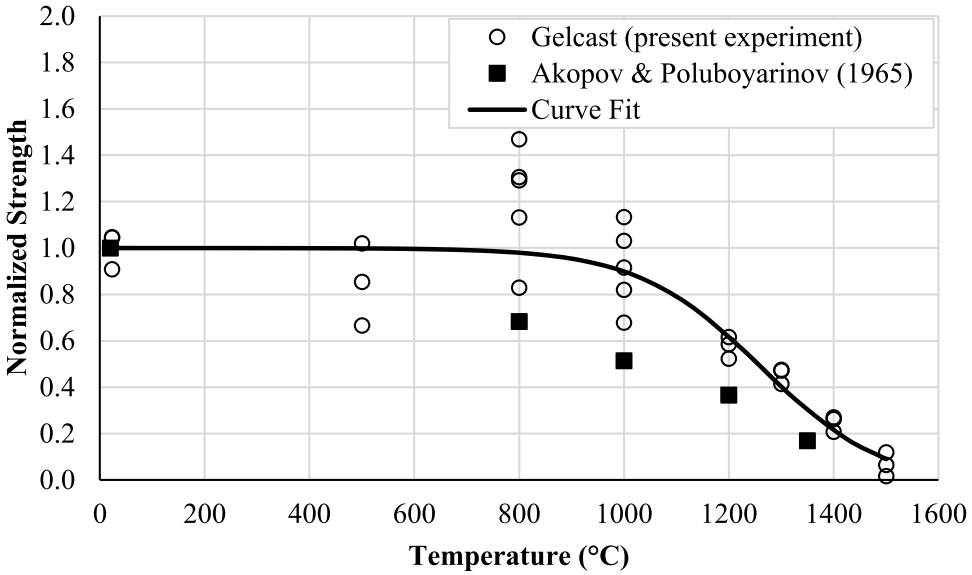


Figure 3.13: Normalized flexural strength compared to those of Akopov and Poluboyarinov [30]. The normalized curve fit for gelcast ceria, resulting from Eq. (3.5), is also included.

tests is obtained from [89]

$$V_{\mathrm{E,W}} = \frac{h_{\mathrm{W}} w_{\mathrm{W}} L_{\mathrm{o,W}}}{6} \frac{m+3}{(m+1)^2} \tag{3.15}$$

where $V_{\mathrm{E}}$ is the effective volume, and the "W" subscript indicates the first author, Wang. The effective volume for the ¼-point tests performed in our study is

$$V_{\mathrm{E,S}} = \frac{h_{\mathrm{S}} w_{\mathrm{S}} L_{\mathrm{o,S}}}{4} \frac{m+2}{(m+1)^2} \tag{3.16}$$

where the "S" subscript indicates the first author in the present study. The flexural strength can be adjusted to account for effective volume by substituting Eq. (3.15),

Eq. (3.16) and the specimen dimensions (from Table 3.3) into Eq. (3.14)

$$\frac{\sigma_{\mathrm{S}}}{\sigma_{\mathrm{W}}} = \left[\frac{13(m+3)}{30(m+2)}\right]^{1/m} \tag{3.17}$$

The data of Wang et al. can then be used to predict the strength expected in this study. Note that Eq. (3.17) indicates that our failure strength is expected to be lower than that of Wang et al. for all positive values of $m$. A lower bound is estimated by using their minimum strength, after adjustment to 0.20 porosity, and the minimum Weibull modulus of 2.8 in Eq. (3.17). A parallel procedure is used to estimate an upper bound, yielding

$$46 \text{ MPa} \leq \sigma_{\mathrm{S,predicted}} \leq 78 \text{ MPa} \tag{3.18}$$

While the measured data from our study are at the upper limit of the estimated range, the effect of grain size has not yet been considered. Unfortunately, no available experimental studies quantify the constants in the Hall–Petch relationship for ceria. Therefore, we can only utilize the qualitative relation that a smaller grain size is expected to produce a higher strength. Because the grain size of the specimens tested here is smaller than that reported by Wang et al., a higher strength is expected from this study, which is consistent with the strength of our specimens being at the upper limit of the range in Eq. (3.18).

Comparing our data with that of Cutler and Meixner [92] is more challenging still, as the porosity of their specimens varied over a wide range and their grain size is

unknown. However, their specimen geometry is identical to ours, so compensation for effective volume effects is not required. A coarse lower bound for the expected strength for our specimens is made by adjusting their lower bound for flexural strength from their minimum porosity of 0.03 to 0.20. A coarse upper bound is estimated in a parallel manner, yielding

$$85 \text{ MPa} \leq \sigma_{\text{S,predicted}} \leq 142 \text{ MPa} \tag{3.19}$$

While our data fall below the lower bound of Cutler and Meixner, this trend could occur if their specimens had a smaller grain size. Note that the minimum strength predicted from Cutler and Meixner's data is above the maximum predicted strength resulting from the data of Wang et al.

The trends observed for elastic modulus and flexural strength are similar to those seen in comparable ceramics. For example, Munro [73] provides equivalent data for dense alumina. For comparison, our data are corrected to zero porosity. The elastic modulus of alumina exhibits a near-linear decrease from 0 to 1600 °C. This trend is similar to our elastic modulus, except the alumina is approximately 4.5 times stiffer at room temperature, and the ceria data are better described by a quadratic fit. The rate of decrease of modulus with temperature is about the same for ceria and alumina. Dense alumina is approximately 2.8 times stronger than dense ceria, but both exhibit a precipitous dropoff in strength beginning around 900 °C. The dropoff in strength of ceria appears to be more linear than that of alumina. The trend of the strength data

for alumina is consistent with our data in Fig. 3.13, but different than that of Akopov and Poluboyarinov [30].

## 3.8 Conclusion

This paper presents new data on the temperature dependency of the elastic modulus and flexural strength of ceria, specifically gelcast ceria, to 1500 °C. The elastic modulus decreases monotonically from about 90 GPa at room temperature to about 16 GPa at 1500 °C. The flexural strength remains approximately constant at about 78 MPa to a temperature to about 900 °C. At higher temperatures, its strength drops roughly linearly with increasing temperature to about 5 MPa at 1500 °C.

The data add to the very limited data available in the scientific literature for ceria and extend the upper temperature range of previous results by 150 °C. Overall, the trends of decreasing strength and elastic modulus with increasing temperature are consistent with previously reported trends in the literature.

When using the data presented in this study, care should be taken to consider the impact of material morphology. While the data were obtained for gelcast specimens with a porosity of 0.20, the results can be extended to other low porosities using the minimum solid area model. Adjusting the previously published moduli to equivalent porosity using the MSA model produced good agreement with the new experiments.

Only one previous source for high-temperature flexural strength data is published [30]. Some discrepancy appears to exist between the previous and current flexural

strength data after correcting for porosity. However, little is known about the testing details for the earlier data; the discrepancy is possibly attributable to differences in test fixture or grain size in the earlier test specimens. Reasonable agreement was found with available room temperature flexural strength data.

The present study was motivated by the desire to utilize ceria RPC in solar thermochemical reactors as self supporting catalytic structures. A gelcast ceria was used as the surrogate because of manufacturing similarities with the replication method used to manufacture RPC. Great care was taken to ensure that the morphology of the gelcast material tested here is representative of that in RPC ligaments. Nevertheless, the results are applicable to other ceria morphologies in addition to RPC. The enhanced data presented here facilitate exploiting ceria in new high-temperature applications.

## 3.9 Acknowledgments

This research was supported by the National Science Foundation (EFRI-1038307) and the University of Minnesota Initiative for Renewable Energy and the Environment. Parts of this work were carried out in the Characterization Facility, University of Minnesota, which receives partial support from NSF through the MRSEC program. The authors appreciate the assistance of Steven Goodrich, University of Dayton Research Institute, in performing the flexural tests at elevated temperature, and Rudolph Olson, SELEE Corp., in preparing the samples. Micrographs of RPC are courtesy of Peter Krenzke.

# Chapter 4

# Conclusion

## 4.1 Summary

The primary objective of the present work was to develop and validate a model for predicting the elastic properties of RPCs based on the ligament/matrix structure and the ligament elastic modulus. A secondary objective was to characterize the elastic modulus and flexural strength of material representative of the morphology of ceramic ligaments in RPCs. Ceria was selected as an example ceramic because of its recent use in solar thermochemical redox cycles.

To determine the elastic modulus, shear modulus, and Poisson's ratio of RPCs, a model was developed that accurately captures the cellular structure and ligament geometry. Previous models of foam elastic properties either have simplified cell geometries [28], neglect energy components in the model of deformation [26, 27], or use ligament

geometries not representative of RPCs [22, 25]. The new model presented herein has a cellular geometry of tetrakaidecahedrons, which based on previous measurements of cellular shapes in foams is the most frequent cellular shape in foams [21, 22]. The ligaments are represented by double Plateau border cross sections, capturing the internal void shape that is found within RPC ligaments, along with the varying shapes possible from the replication manufacturing process. The size of the ligament varies along the length, capturing an aspect of the structure that was neglected in prior models. The model also accounts for the energy component attributable to the shear forces in the ligaments. This component was neglected in most earlier models of foams [26–28].

While the results show that the specific cross-sectional shape, within the bounds of a double Plateau border, have relatively little effect on the relative moduli, using cell shapes and ligament shapes representative of those in RPCs significantly improves the predictive capabilities for RPC elastic properties versus the model of Gibson and Ashby, which assumed a staggered cubic cell structure. The small impact of changing the distribution of the material in the ligament around the internal Plateau border void is captured by the "thickness" of the curves in Figs. 2.15–2.17. The relatively small effect of the distribution is due to the small change in the second moment of area with changing cross-sectional shape (Fig. 2.18). The new model predicts a relative elastic modulus within 30% of the experimentally measured values of ceria RPC. This agreement is a significant improvement compared to the 95% over prediction by the Gibson and Ashby model.

Prior to the work presented in this dissertation, the mechanical properties of ceria were unknown above 1350 °C. With the results presented in Chapter 3, the temperature dependence of the elastic modulus and flexural strength of ceria with a porosity of 20% and microstructure representative of the porosity seen in the ligaments of a ceria RPC is now known. As expected, elastic modulus declines steadily with increasing temperature. At low temperatures, the flexural strength is relatively constant with increasing temperature up to 1000 °C. Above 1000 °C, the flexural strength decreases rapidly at a rate of ∼0.12 MPa/°C. The porosity dependence of the elastic modulus was quantified through comparisons with prior data at low temperatures using the MSA model [29, 34, 35]. An MSA exponent constant of 3.0 provides the best fit to the data.

## 4.2 Contributions

The new model is the first model of the effective elastic modulus, shear modulus, and Poisson's ratio applicable to RPCs. With the model, a more accurate prediction of deformation and stress is realizable in structural analyses of RPC components. The model allows researchers to investigate the impact of potential changes to the RPC structure on the response of the component. In conjunction with an RPC failure model, the elastic properties model can be used to evaluate the structural integrity of RPC components.

Increasing the temperature range for the elastic modulus and flexural strength of ceria from 1350 °C to 1500 °C takes the range for which ceria can be designed for

structural service to new limits. Structural challenges have been seen in using ceria in high temperature solar redox reactors. With the additions of the RPC properties model and the high temperature ceria data, improved structural modeling of components can be performed.

## 4.3 Recommendations for Future Work

One area of interest for refinement of the model of the RPC elastic properties is to alter the assumption of how the material is distributed along the length of the ligaments. In the present model, the distance between the internal cusps and external cusps is assumed to be constant in each specified geometry. This assumption affects how the surrounding material of the ligament is sized with respect to the internal void, changing the integral constants. Alternative assumptions could include scaling the thickness with the size of the internal void, effectively keeping the same cross-sectional shape along the entire length of the ligament, or generating a new functional description on how the size scales along the length, independent of the internal void size. Allowing for changes in this parameter would effectively generate another control with which the stiffness of the ligaments could be altered, changing the elastic properties of the RPC.

Another avenue of further investigation would be to add cell elongation into the model. This addition would change the material from an isotropic cellular material to an orthotropic cellular material. Relaxing this constraint of a tetrakaidecahedron with eight regular hexagonal faces and six square faces would add another variable that would

correspond to elongation seen in some RPCs. A study in cell elongation on the resultant properties in the model may be used to quantify the observed differences in elastic modulus when numerical compression tests were performed on RPCs in orthogonal directions [23].

Adding cell elongation to the model while relaxing the cusp distance assumption would open up interesting possibilities regarding mass distribution on ligaments of varying size. Surface tension of the slurry material used in the replication process could promote material to gather in regions with smaller ligaments, generating variations in the stiffness of ligaments within the RPC. The stiffness of the smaller ligaments where more mass would gather would likely increase, while the stiffness of the longer ligaments where the material has been removed would likely decrease. Understanding how these two competing trends affect the overall RPC elastic properties could lead to new requirements on the slurry used in the manufacture to produce desired RPC elastic properties.

Developing a model for predicting the tensile strength of RPCs that utilizes the actual ligament geometry is of interest. The addition of a strength model would allow one to not only predict the elastic response of an RPC, but also to predict the failure response. One large challenge foreseen in developing a strength model is accurately characterizing the ligament strength. The strength of ceramics scales with volume, so an RPC with a higher pore density (smaller ligaments) could lead to an increase in ligament strength. At the same time, the randomness of the structure of RPCs leads to

ligaments of varying size stressed by varying amounts, which in turn leads to failure of some ligaments before others. Failure of isolated ligaments leads to increased loads on adjacent ligaments. The tensile strength of RPC corresponds to the failure of a series of adjacent ligaments in an RPC, such that adjacent ligaments continue to fail with no increase in load. Because ceramic strength is an extrinsic property and the RPC ligaments form a random structure, use of statistical techniques for developing a model of RPC tensile strength may be preferred over a continuum method.

Additional experimental elastic property characterizations of ceria RPCs are also of interest. The reported ceria RPC experiments were for specimens with the same nominal relative density and pore density. Obtaining elastic property measurements of ceria RPCs at different relative densities and pore densities would provide additional validation of the model. These experiments would further confirm the trend of increasing modulus with increasing relative density, and provide confirmation that the size of the pores in the RPC does not impact the moduli. Additional experiments to obtain the elastic properties of ceria RPC at varying relative densities and varying temperatures would also provide additional validation to the relative density dependent and temperature dependent elastic modulus projections. Because the model shows that the RPC elastic properties are a function of the ligament elastic modulus, the same temperature dependence trend would be expected in the ligament and the RPC.

The work in this dissertation presents a model for predicting the elastic properties of RPCs. The model accounts for the specific cellular and ligament geometries within

RPCs. The model was developed and partially validated against property data available in the literature and experimental characterizations on ceria RPCs. The model is shown to provide a significant improvement in predicting the elastic response of RPCs when compared to a previous model for high density foams. Additionally, the mechanical properties of ceria at temperatures never before examined were quantified, opening up new opportunities of utilizing ceria at high temperatures.

# References


[1] H. S. Gandhi, G. W. Graham, and R. W. McCabe. Automotive exhaust catalysis. Journal of Catalysis, 216(1–2):433–442, May–June 2003.

[2] Liang-Shu Zhong, Jin-Song Hu, An-Min Cao, Qiang Liu, Wei-Guo Song, and Li-Jun Wan. 3D Flowerlike Ceria Micro/Nanocomposite Structure and Its Application for Water Treatment and CO Removal. Chemistry of Materials, 19(7):1648–1655, April 2007.

[3] D. L. Maricle, T. E. Swarr, and S. Karavolis. Enhanced ceria – a low-temperature SOFC electrolyte. Solid State Ionics, 52(1–3):173–182, May 1992.

[4] Hiroshi Kaneko, Takao Miura, Akinori Fuse, Hideyuki Ishihara, Shunpei Taku, Hiroaki Fukuzumi, Yuuki Naganuma, and Yutaka Tamaura. Rotary-Type Solar Reactor for Solar Hydrogen Production with Two-step Water Splitting Process. Energy and Fuels, 21(4):2287–2293, July 2007.

[5] James E. Miller, Mark D. Allendorf, Andrea Ambrosini, Ken S. Chen, Eric N.

Coker, Daniel E. Dedrick, Richard B. Diver, Roy E. Hogan, Ivan Ermanoski, Terry A. Johnson, Gary L. Kellogg, Anthony H. McDaniel, Nathan P. Siegel, Chad L. Staiger, and Ellen B. Stechel. Final Report – Reimagining Liquid Transportation Fuels: Sunshine to Petrol. Sandia National Laboratories Report No. SAND2012-0307, January 2012.

[6] Roman Bader, Rohini Bala Chandran, Luke J. Venstrom, Stephen J. Sedler, Peter T. Krenzke, Robert M. De Smith, Aayan Banerjee, Thomas R. Chase, Jane H. Davidson, and Wojciech Lipiński. Design of a Solar Reactor to Split $CO_2$ Via Isothermal Redox Cycling of Ceria. Journal of Solar Energy Engineering, 137(3):031007, June 2015.

[7] Brandon J. Hathaway, Rohini Bala Chandran, Stephen Sedler, Daniel Thomas, Adam Gladen, Thomas Chase, and Jane H. Davidson. Effect of Flow Rates on Operation of a Solar Thermochemical Reactor for Splitting $CO_2$ via the Isothermal Ceria Redox Cycle. Journal of Solar Energy Engineering, 138(1):011007, February 2016.

[8] Brandon Jay Hathaway, Rohini Bala Chandran, Adam C. Gladen, Thomas R. Chase, and Jane H. Davidson. Demonstration of a Solar Reactor for Carbon Dioxide Splitting via the Isothermal Ceria Redox Cycle and Practical Implications. Energy & Fuels, 30(8):6654–6661, August 2016.

[9] Justin Lapp and Wojciech Lipiński. Transient Three-Dimensional Heat Transfer Model of a Solar Thermochemical Reactor for $H_2O$ and $CO_2$ Splitting Via Nonstoichiometric Ceria Redox Cycling. Journal of Solar Energy Engineering, 136(3):031006, January 2014.

[10] J. W. Brockmeyer and L. S. Aubrey. Application of Ceramic Foam Filters in Molten Metal Filtration. In W. J. Smothers, editor, Application of Refractories: Ceramic Engineering and Science Proceedings, volume 8, pages 63–74. John Wiley & Sons, Inc., Hoboken, NJ, 1987.

[11] Joerg Adler. Ceramic Diesel Particulate Filters. International Journal of Applied Ceramic Technology, 2(6):429–439, November 2005.

[12] Amanda J. Barra and Janet L. Ellzey. Heat recirculation and heat transfer in porous burners. Combustion and Flame, 137(1–2):230–241, April 2004.

[13] Qizhi Z. Chen, Ian D. Thompson, and Aldo R. Boccaccini. 45S5 Bioglass®-derived glass–ceramic scaffolds for bone tissue engineering. Biomaterials, 27(11):2414–2425, April 2006.

[14] Philipp Furler, Jonathan Scheffe, Michal Gorbar, Louis Moes, Ulrich Vogt, and Aldo Steinfeld. Solar Thermochemical $CO_2$ Splitting Utilizing a Reticulated Porous Ceria Redox System. Energy & Fuels, 26(11):7051–7059, November 2012.

[15] Karl Schwartzwalder and Arthur V. Somers. US Patent #3090094, "Method of making porous ceramic articles", May 1963.

[16] Jeannine Saggio-Woyansky, Curtis E. Scott, and W. P. Minnear. Processing of Porous Ceramics. American Ceramic Society Bulletin, 71(11):1674–1682, November 1992.

[17] Xinwen Zhu, Dongliang Jiang, Shouhong Tan, and Zhaoquan Zhang. Improvement in the Strut Thickness of Reticulated Porous Ceramics. Journal of the American Ceramic Society, 84(7):1654–1656, July 2001.

[18] Xiumin Yao, Shouhong Tan, Zhengren Huang, and Dongliang Jiang. Effect of recoating slurry viscosity on the properties of reticulated porous silicon carbide ceramics. Ceramics International, 32(2):137–142, March 2006.

[19] Xinwen Zhu, Dongliang Jiang, and Shouhong Tan. Improvement in the strength of reticulated porous ceramics by vacuum degassing. Materials Letters, 51(4):363–367, November 2001.

[20] Joseph Antoine Ferdinand Plateau. Statique expérimentale et théorique des liquides soumis aux seules forces moléculaires. Gauthier-Villars, Paris, 1873.

[21] Edwin B Matzke. The Three-Dimensional Shape of Bubbles in Foam—An Analysis of the Role of Surface Forces in Three-Dimensional Cell Shape Determination. American Journal of Botany, 33(1):58–80, January 1946.

[22] L. Gong, S. Kyriakides, and W.-Y. Jang. Compressive response of open-cell foams. Part I: Morphology and elastic properties. International Journal of Solids and Structures, 42(5–6):1355–1379, March 2005.

[23] Claudio D'Angelo, Alberto Ortona, and Paolo Colombo. Finite element analysis of reticulated ceramics under compression. Acta Materialia, 60(19):6692–6702, November 2012.

[24] Hiroshi Hagiwara and David J. Green. Elastic Behavior of Open-Cell Alumina. Journal of the American Ceramic Society, 70(11):811–815, November 1987.

[25] Wen Yea Jang, Andrew M. Kraynik, and Stelios Kyriakides. On the microstructure of open-cell foams and its effect on elastic properties. International Journal of Solids and Structures, 45(7–8):1845–1875, April 2008.

[26] H. X. Zhu, J. F. Knott, and N. J. Mills. Analysis of the elastic properties of open-cell foams with tetrakaidecahedral cells. Journal of the Mechanics and Physics of Solids, 45(3):319–343, March 1997.

[27] W. E. Warren and A. M. Kraynik. Linear Elastic Behavior of a Low-Density Kelvin Foam With Open Cells. Journal of Applied Mechanics, 64(4):787, December 1997.

[28] L. J. Gibson and M. F. Ashby. The Mechanics of Three-Dimensional Cellular Materials. Proceedings of the Royal Society of London A: Mathematical, Physical and Engineering Sciences, 382(1782):43–59, July 1982.

[29] James F. Wygant. Elastic and Flow Properties of Dense, Pure Oxide Refractories. Journal of the American Ceramic Society, 34(12):374–380, December 1951.

[30] F. A. Akopov and D. N. Poluboyarinov. Some properties of sintered ceria ceramics. Refractories, 6(3–4):196–201, March 1965.

[31] F. A. Costa Oliveira. Elastic moduli of open-cell cordierite foams. Journal of Non-Crystalline Solids, 351(19–20):1623–1629, July 2005.

[32] S. K. Maiti, L. J. Gibson, and M. F. Ashby. Deformation and energy absorption diagrams for cellular solids. Acta Metallurgica, 32(11):1963–1975, November 1984.

[33] R. W. Rice. The Porosity Dependence of Physical Properties of Materials: A Summary Review. Key Engineering Materials, 115:1–20, 1996.

[34] Kazuhisa Sato, Ken Suzuki, Keiji Yashiro, Tatsuya Kawada, Hiroo Yugami, Toshiyuki Hashida, Alan Atkinson, and Junichiro Mizusaki. Effect of $Y_2O_3$ addition on the conductivity and elastic modulus of $(CeO_2)_{1-x}(YO_{1.5})_x$. Solid State Ionics, 180(20–22):1220–1225, August 2009.

[35] K. Sato, H. Yugami, and T. Hashida. Effect of rare-earth oxides on fracture properties of ceria ceramics. Journal of Materials Science, 39(18):5765–5770, September 2004.

[36] Yanli Wang, Keith Duncan, Eric D. Wachsman, and Fereshteh Ebrahimi. The

effect of oxygen vacancy concentration on the elastic modulus of fluorite-structured oxides. Solid State Ionics, 178(1–2):53–58, January 2007.

[37] M. Lipińska-Chwałek, F. Schulze-Küppers, and J. Malzbender. Mechanical properties of pure and doped cerium oxide. Journal of the European Ceramic Society, 35(5):1539–1547, May 2015.

[38] S. Maschio, O. Sbaizero, and S. Meriani. Mechanical properties in the ceria-zirconia system. Journal of the European Ceramic Society, 9(2):127–132, March 1992.

[39] James M. Gere. Mechanics of Materials. Brooks/Cole, Pacific Grove, CA, 5th edition, 2001.

[40] The MathWorks, Inc. MATLAB R2012a [Computer software], 2012.

[41] W. E. Warren, M. K. Neilsen, and A. M. Kraynik. Torsional rigidity of a plateau border. Mechanics Research Communications, 24(6):667–672, November–December 1997.

[42] Parametric Technology Corporation. Creo Elements/Pro 5.0 [Computer software], 2012.

[43] Stephen J. Sedler, Thomas R. Chase, and Jane H. Davidson. Mechanical Properties of Gelcast Cerium Dioxide From 23 to 1500 °C. Journal of Engineering Materials and Technology, 139(1):011008, January 2017.

[44] Xiangdong Feng, Dean C. Sayle, Zhong Lin Wang, M. Sharon Paras, Brian Santora, Anthony C. Sutorik, Thi X. T. Sayle, Yi Yang, Yong Ding, Xudong Wang, and Yie-Shein Her. Converting Ceria Polyhedral Nanoparticles into Single-Crystal Nanospheres. Science, 312(5779):1504–1508, June 2006.

[45] LeRoy Eyring. The Binary Lanthanide Oxides: Synthesis and Identification. In G. Meyer and L. R. Morss, editors, Synthesis of Lanthanide and Actinide Compounds, volume 2, pages 187–224. Springer, Dordrecht, Netherlands, 1991.

[46] William C. Chueh and Sossina M. Haile. A thermochemical study of ceria: exploiting an old material for new modes of energy conversion and $CO_2$ mitigation. Philosophical Transactions of the Royal Society A: Mathematical, Physical and Engineering Sciences, 368(1923):3269–3294, July 2010.

[47] William C. Chueh, Christoph Falter, Mandy Abbott, Danien Scipio, Philipp Furler, Sossina M. Haile, and Aldo Steinfeld. High-Flux Solar-Driven Thermochemical Dissociation of $CO_2$ and $H_2O$ Using Nonstoichiometric Ceria. Science, 330(6012):1797–1801, December 2010.

[48] Philipp Furler, Jonathan R. Scheffe, and Aldo Steinfeld. Syngas production by simultaneous splitting of $H_2O$ and $CO_2$ via ceria redox reactions in a high-temperature solar reactor. Energy & Environmental Science, 5(3):6098–6103, March 2012.

[49] Philipp Furler, Jonathan Scheffe, Daniel Marxer, Michal Gorbar, Alexander Bonk,

Ulrich Vogt, and Aldo Steinfeld. Thermochemical $CO_2$ splitting via redox cycling of ceria reticulated foam structures with dual-scale porosities. Physical Chemistry Chemical Physics, 16(22):10503–10511, June 2014.

[50] Luke J. Venstrom, Robert M. De Smith, Yong Hao, Sossina M. Haile, and Jane H. Davidson. Efficient Splitting of $CO_2$ in an Isothermal Redox Cycle Based on Ceria. Energy & Fuels, 28(4):2732–2742, April 2014.

[51] R. J. Panlener, R. N. Blumenthal, and J. E. Garnier. A thermodynamic study of nonstoichiometric cerium dioxide. Journal of Physics and Chemistry of Solids, 36(11):1213–1222, November 1975.

[52] Luke J. Venstrom, Nicholas Petkovich, Stephen Rudisill, Andreas Stein, and Jane H. Davidson. The Effects of Morphology on the Oxidation of Ceria by Water and Carbon Dioxide. Journal of Solar Energy Engineering, 134(1):011005, February 2012.

[53] Nicholas D. Petkovich, Stephen G. Rudisill, Luke J. Venstrom, Daniel B. Boman, Jane H. Davidson, and Andreas Stein. Control of Heterogeneity in Nanostructured $Ce_{1-x}Zr_xO_2$ Binary Oxides for Enhanced Thermal Stability and Water Splitting Activity. The Journal of Physical Chemistry C, 115(43):21022–21033, November 2011.

[54] Stephen G. Rudisill, Luke J. Venstrom, Nicholas D. Petkovich, Tingting Quan, Nicholas Hein, Daniel B. Boman, Jane H. Davidson, and Andreas Stein. Enhanced

Oxidation Kinetics in Thermochemical Cycling of $CeO_2$ through Templated Porosity. The Journal of Physical Chemistry C, 117(4):1692–1700, January 2013.

[55] William T. Gibbons, Luke J. Venstrom, Robert M. De Smith, Jane H. Davidson, and Gregory S. Jackson. Ceria-based electrospun fibers for renewable fuel production via two-step thermal redox cycles for carbon dioxide splitting. Physical Chemistry Chemical Physics, 16(27):14271–14280, July 2014.

[56] Ellen Wachtel and Igor Lubomirsky. The elastic modulus of pure and doped ceria. Scripta Materialia, 65(2):112–117, July 2011.

[57] Arata Nakajo, Jakob Kuebler, Antonin Faes, Ulrich F. Vogt, Hans Jürgen Schindler, Lieh-Kwang Chiang, Stefano Modena, Jan Van herle, and Thomas Hocker. Compilation of mechanical properties for the structural analysis of solid oxide fuel cell stacks. Constitutive materials of anode-supported cells. Ceramics International, 38(5):3907–3927, July 2012.

[58] Anna Kossoy, Anatoly I. Frenkel, Yishay Feldman, Ellen Wachtel, Alla Milner, and Igor Lubomirsky. The origin of elastic anomalies in thin films of oxygen deficient ceria, $CeO_{2-x}$. Solid State Ionics, 181(33–34):1473–1477, October 2010.

[59] Yanli Wang, Keith L. Duncan, Eric D. Wachsman, and Fereshteh Ebrahimi. Effects of Reduction Treatment on Fracture Properties of Cerium Oxide. Journal of the American Ceramic Society, 90(12):3908–3914, December 2007.

[60] A. Kaiser, S. Foghmoes, C. Chatzichristodoulou, M. Søgaard, J. A. Glasscock, H. L. Frandsen, and P. V. Hendriksen. Evaluation of thin film ceria membranes for syngas membrane reactors—Preparation, characterization and testing. Journal of Membrane Science, 378(1–2):51–60, August 2011.

[61] Sean R. Bishop, Keith L. Duncan, and Eric D. Wachsman. Defect equilibria and chemical expansion in non-stoichiometric undoped and gadolinium-doped cerium oxide. Electrochimica Acta, 54(5):1436–1443, February 2009.

[62] C. Chatzichristodoulou, P. V. Hendriksen, and A. Hagen. Defect Chemistry and Thermomechanical Properties of $Ce_{0.8}Pr_xTb_{0.2-x}O_{2-\delta}$. Journal of the Electrochemical Society, 157(2):B299–B307, 2010.

[63] C. Chatzichristodoulou and P. V. Hendriksen. Oxygen Nonstoichiometry and Defect Chemistry Modeling of $Ce_{0.8}Pr_{0.2}O_{2-\delta}$. Journal of the Electrochemical Society, 157(4):B481–B489, 2010.

[64] ASTM. C1211-13, "Standard Test Method for Flexural Strength of Advanced Ceramics at Elevated Temperatures". ASTM International, West Conshohocken, PA, 2013.

[65] Ogbemi O. Omatete, Mark A. Janney, and Richard A. Strehlow. Gelcasting – a new ceramic forming process. American Ceramic Society Bulletin, 70(10):1641–1649, October 1991.

[66] Mark A. Janney and Ogbemi O. Omatete. US Patent #5028362: "Method for molding ceramic powders using a water-based gel casting", July 1991.

[67] John P. Coakley and James P. M. Syvitski. SediGraph technique. In James P. M. Syvitski, editor, Principles, Methods, and Application of Particle Size Analysis, pages 129–142. Cambridge University Press, Cambridge, United Kingdom, 1991.

[68] François Cardarelli. Materials handbook: a concise desktop reference. Springer, London, 2nd edition, 2008.

[69] Warren C. Young, Richard G. Budynas, and Ali M. Sadegh. Roark's Formulas for Stress and Strain. McGraw-Hill, New York, 8 edition, 2011.

[70] Y. S. Touloukian, R. K. Kirby, R. E. Taylor, and T. Y. R. Lee. Thermal Expansion – Nonmetallic Solids, volume 13 of Thermophysical Properties of Matter. IFI/Plenum, New York, 1977.

[71] M. Lipińska-Chwałek, G. Pećanac, and J. Malzbender. Creep behaviour of membrane and substrate materials for oxygen separation units. Journal of the European Ceramic Society, 33(10):1841–1848, September 2013.

[72] Dietrich Munz and Theo Fett. Ceramics: Mechanical Properties, Failure Behaviour, Materials Selection. Springer, Berlin, 1999.

[73] R. G. Munro. Evaluated Material Properties for a Sintered $\alpha$-Alumina. Journal of the American Ceramic Society, 80(8):1919–1928, August 1997.

[74] F. F. Lange and K. T. Miller. Open-cell, low-density ceramics fabricated from reticulated polymer substrates. Advanced Ceramic Materials (USA), 2(4):827–831, October 1987.

[75] L. J. Gibson and M. F. Ashby. Cellular Solids: Structure and Properties. Cambridge Solid State Science Series. Cambridge University Press, New York, 2nd edition, 1997.

[76] A. N. Gent and A. G. Thomas. The deformation of foamed elastic materials. Journal of Applied Polymer Science, 1(1):107–113, January/February 1959.

[77] J. M. Lederman. The prediction of the tensile properties of flexible foams. Journal of Applied Polymer Science, 15(3):693–703, March 1971.

[78] J. G. Zwissler and M. A. Adams. Fracture Mechanics of Cellular Glass. In R. C. Bradt, Anthony G. Evans, D. P. H. Hasselman, and F. F. Lange, editors, Fracture Mechanics of Ceramics, volume 6, pages 211–241. Plenum Press, New York, 1983.

[79] Paolo Colombo, John R. Hellmann, and David L. Shelleman. Mechanical Properties of Silicon Oxycarbide Ceramic Foams. Journal of the American Ceramic Society, 84(10):2245–2251, October 2001.

[80] Santanu Dhara and Parag Bhargava. Influence of Slurry Characteristics on Porosity and Mechanical Properties of Alumina Foams. International Journal of Applied Ceramic Technology, 3(5):382–392, October 2006.

[81] Vaughan Pratt. Direct Least-squares Fitting of Algebraic Surfaces. Computer Graphics, 21(4):145–152, July 1987.

[82] ASTM. E112-13, "Standard Test Methods for Determining Average Grain Size". ASTM International, West Conshohocken, PA, 2014.

[83] R. W. Rice. Evaluation and extension of physical property-porosity models based on minimum solid area. Journal of Materials Science, 31(1):102–118, January 1996.

[84] R. W. Rice. Comparison of physical property-porosity behaviour with minimum solid area models. Journal of Materials Science, 31(6):1509–1528, January 1996.

[85] M. Radovic, E. Lara-Curzio, and L. Riester. Comparison of different experimental techniques for determination of elastic properties of solids. Materials Science and Engineering: A, 368(1–2):56–70, March 2004.

[86] Waloddi Weibull. A Statistical Distribution Function of Wide Applicability. Journal of Applied Mechanics, 18(3):293–297, September 1951.

[87] ASTM. C1239-13, "Standard Practice for Reporting Uniaxial Strength Data and Estimating Weibull Distribution Parameters for Advanced Ceramics". ASTM International, West Conshohocken, PA, 2013.

[88] G. Pećanac, S. Foghmoes, M. Lipińska-Chwałek, S. Baumann, T. Beck, and J. Malzbender. Strength degradation and failure limits of dense and porous ceramic

membrane materials. Journal of the European Ceramic Society, 33(13–14):2689–2698, November 2013.

[89] George D Quinn. Weibull Strength Scaling for Standardized Rectangular Flexure Specimens. Journal of the American Ceramic Society, 86(3):508–510, March 2003.

[90] E. O. Hall. The Deformation and Ageing of Mild Steel: III Discussion of Results. Proceedings of the Physical Society. Section B, 64(9):747–753, September 1951.

[91] N. J. Petch. The cleavage strength of polycrystals. J. Iron Steel Inst., 174:25–28, 1953.

[92] Raymond A. Cutler and D. Laurence Meixner. Ceria–lanthanum strontium manganite composites for use in oxygen generation systems. Solid State Ionics, 159(1–2):9–19, March 2003.

[93] Stephen J. Sedler, Thomas R. Chase, and Jane H. Davidson. Modeling the Elastic Properties of Reticulated Porous Ceramics. Journal of Engineering Materials and Technology, In Press.

[94] Mark A. Janney. Weibull Statistics and Scaling Laws for Reticulated Ceramic Foam Filters. In M Brito, E Case, W M Kriven, J Salem, and D Zhu, editors, Developments in Porous, Biological and Geopolymer Ceramics, volume 28 of Ceramic Engineering and Science Proceedings, pages 105–112. John Wiley & Sons, Inc., 2007.

# Appendix A

# Ceria RPC Flexural Test Details

## A.1 Materials and Methods

The flexural test specimens are ceria RPCs manufactured using the replication method and fired at 1580 °C. The specimens are rectangular with nominal dimensions of 87 mm × 39 mm × 10 mm, and a nominal pore density of 30 pores per inch (ppi). An image of the RPC structure is shown in Fig. A.1. Along with having a macroporosity due to the RPC structure, the ceria material from which the ligaments are constructed has a microporosity of $23 \pm 2\%$ [43].

The relative densities of the RPC specimens were determined by measuring the linear dimensions and mass of the specimens. Using this information, the relative densities of

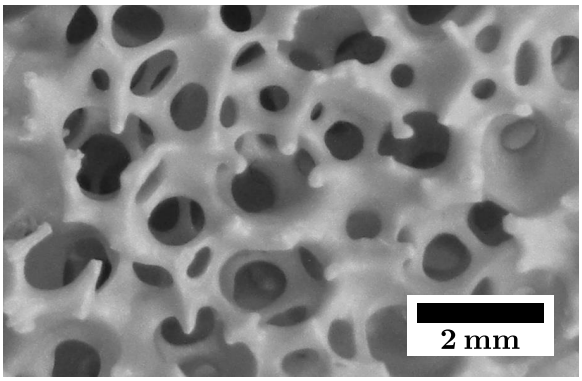


Figure A.1: Photopgraph of the ceria RPC structure

the RPC specimens, $\rho^*/\rho_s$, were calculated using Eq. (A.1):

$$\frac{\rho^*}{\rho_s} = \frac{\frac{m}{Lwh}}{\rho\,(1-P)} \tag{A.1}$$

where $m$ is the mass of the RPC specimen, $L$, $w$, and $h$ are the length, width, and thickness of the specimen, respectively, $\rho$ is the density of ceria (7.65 g/cm$^3$ [68]), and $P$ is the microporosity of the ligament.

The test specimens were loaded in a three-point flexure fixture, with a support span of 80 mm and load point diameters of 12.7 mm. A deflectometer (Epsilon Technology Corp., 3540-015T-ST) was centered on the bottom of the specimen to measure the mid-span displacement. A thin strip of plastic (3 mm wide by 0.3 mm thick) was positioned between the deflectometer tip and the specimen to prevent the deflectometer tip from entering the volume of the beam. A standard universal test machine (MTS, QTest/10) was used load the specimens at a constant crosshead displacement rate of 1 mm/min until there was fracture through the thickness of the specimens. A load cell

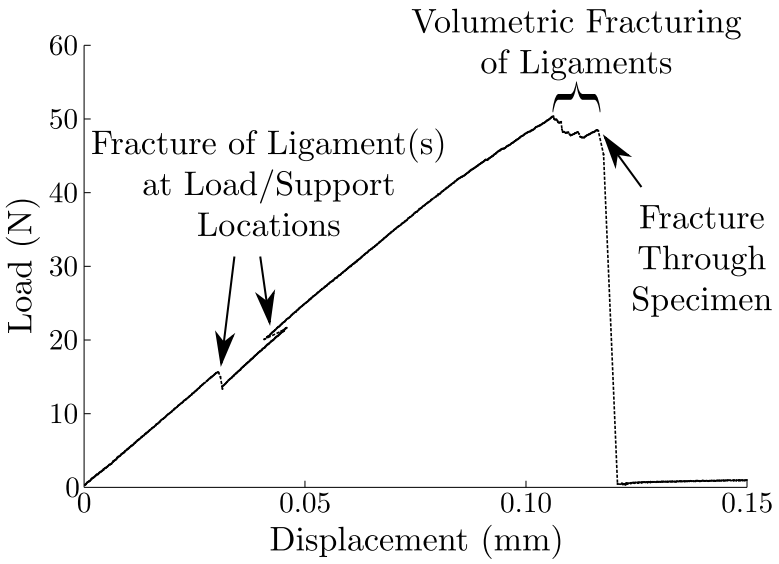


Figure A.2: Typical load vs. displacement curve from the experimental tests

(MTS, 1500BLZ-1000N) was mounted between the crosshead and loading fixture. The deflectometer displacement and load were recorded at a rate of 100 Hz. The specimens were tested in atmospheric conditions at 22 °C.

A typical load versus displacement curve is shown in Fig. A.2. The curve shows a general trend of increasing load with increasing displacement. This trend is consistent with what is expected in a bending beam. The short sharp drops in the load are attributed to the localized fracture of individual or groups of ligaments at the support or load points. After the fractures, the load again increases linearly with increasing displacement. Once the load reaches a peak, volumetric fracturing of ligaments occurs as the crack in the RPC propogates. The load drops to near zero as the RPC fractures through the specimen.

Using the change in deflectometer displacement, $\Delta\delta$, and the change in the applied

load, $\Delta F$, the elastic modulus of the RPC, $E^*$, is:

$$E^* = \frac{L_o^3}{4wh^3} * \frac{\sum_{i=1}^{n} (\Delta F)_i}{\sum_{i=1}^{n} (\Delta \delta)_i} \tag{A.2}$$

where $L_o$ is the support span of the test fixture and the summations from 1 to $n$ are for the linearly increasing portions of the curve. The flexural strength of the RPC, $\sigma_{fs}^*$, is:

$$\sigma_{fs}^* = \frac{3L_o F_{max}}{2wh^2} \tag{A.3}$$

where $F_{max}$ is the maximum load applied to the specimen.

## A.2 Results

### A.2.1 Elastic Modulus

Using the load versus displacement data for the 21 specimens, the elastic modulus is determined for each specimen using the linear portions of the curves and Eq. (A.2). The moduli are normalized by the elastic modulus of the nominally 23% porous ligament material. The elastic modulus of a 20% porous gelcast material with the same microstructure as the RPC ligaments is 89 GPa. This value is adjusted to account for the 3% difference in porosity using the Minimum Solid Area approach [33], giving $E_s = 89e^{-3*0.03} = 81$ GPa. The relative elastic modulus is plot in Fig. A.3.

The relative density range examined is small, only spanning between 0.20 and 0.27,

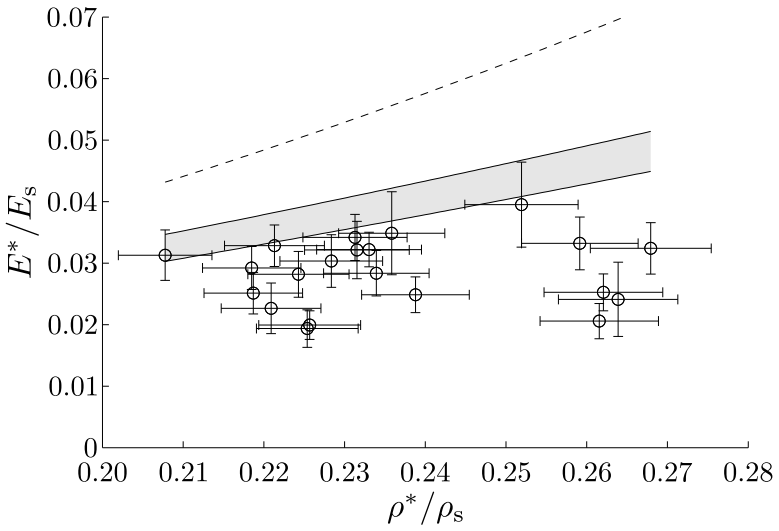


Figure A.3: Measured relative elastic modulus of ceria versus relative density. The shaded region is the expected range from the model developed by Sedler et al. The dashed curve is the model by Gibson and Ashby. The data points are the relative moduli, with the error bars representing the standard errors of the uncertainties.

and the relative uncertainty is large, thus it would not be appropriate to generate a functional relationship between the relative elastic modulus and the relative density by fitting a curve to the data. The data are visually compared to predicted values from analytical models presented in the literature for brittle materials. The two curves shown are two such models proposed as being representative of foams of brittle materials [28, 93]. The average relative density of the specimens examined is 0.236 with a standard deviation of 0.018. The average relative elastic modulus is 0.029 with a standard deviation of 0.005. The simple cubic model by Gibson and Ashby [28] predicts a relative elastic modulus of 0.056 at a relative density of 0.236, an over prediction of the measured average by 95%. The double Plateau border tetrakaidecahedron model developed by Sedler et al. [93] predicts a relative elastic modulus of at least 0.037 at

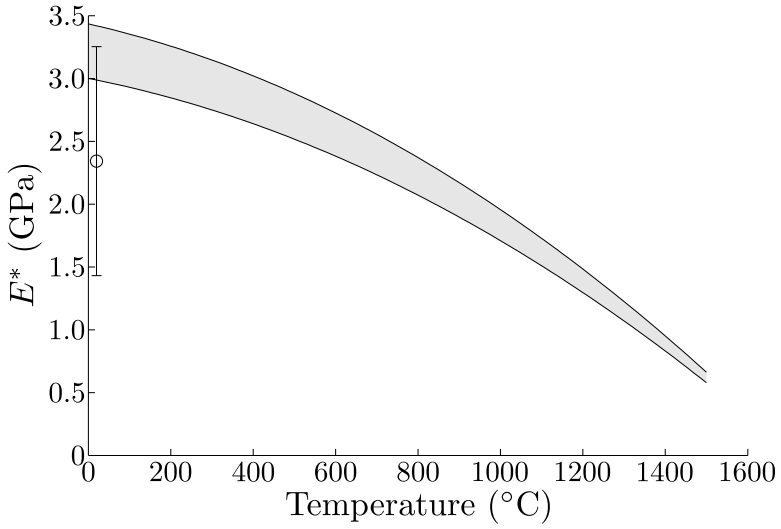


Figure A.4: Projected ceria RPC elastic modulus versus temperature range for an RPC with a relative density of 0.236 and ligaments having a porosity of 23%. The shaded region is generated using the temperature dependent elastic modulus of a 20% porous gelcast ceria, a ligament elastic modulus adjustment using the MSA method, and the bounds from the RPC relative elastic modulus model. The data point presented is the average modulus of the RPC specimens experimentally tested and the error bars are the 95% confidence bounds of Student's t-distribution.

the same relative density, an over prediction of the average by 29%.

A projected temperature dependence of the elastic modulus of an RPC having a relative density of 0.236 and a ligament porosity of 23% is shown in Fig. A.4. The temperature dependence is applied to the model in Eq. (2.1) via the elastic modulus of the ligament. The temperature dependence elastic modulus is that of the gelcast ceria material with microstructure having similar porosity characteristics as the RPC ligament [43]. Having the temperature dependent elastic modulus of the ceria RPC enables structural modeling of the RPC at high temperatures to occur.

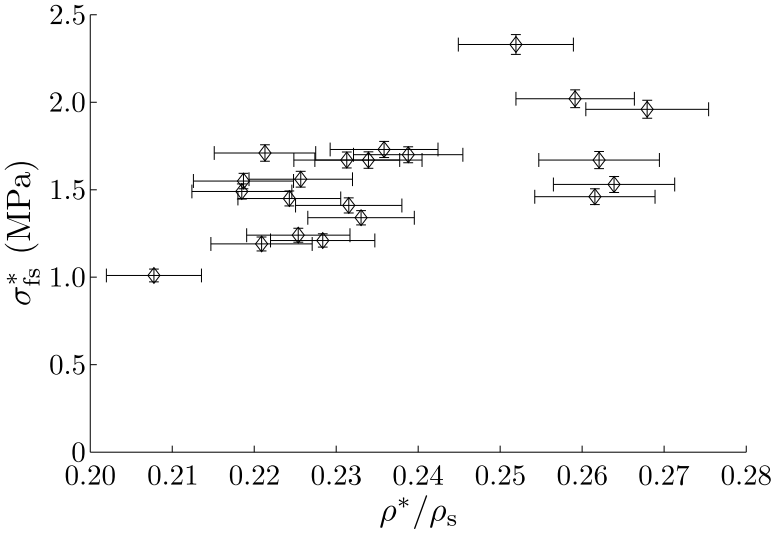


Figure A.5: Measured flexural strength of ceria versus relative density. The error bars are the standard errors based on the measurement uncertainties.

For ceria RPC structures that have a different relative density or a different microporosity, variations to the trend presented would be required. Changes to the amount of microporosity in the ligaments would necessitate use of the MSA model (or other method if the pore shape changes) to adjust the elastic modulus of the ligament. Similarly, altering the relative density of the RPC would impact the relative elastic modulus of the RPC, and thus impact the absolute elastic modulus of the RPC.

### A.2.2 Flexural Strength

Using the same load versus displacement data for the 21 specimens, the flexural strength was determined for each specimen using the peak load of the curves and Eq. (A.3). The flexural strength of each specimen is plot in Fig. A.5 at its corresponding relative density. The average flexural strength of the specimens is 1.57 MPa.

The probability of failure of an RPC specimen is assumed to follow a Weibull distribution [86]:

$$P_{\mathrm{f}} = 1 - e^{-(\sigma^*_{\mathrm{fs}}/\sigma^*_0)^m} \tag{A.4}$$

where $P_{\mathrm{f}}$ is the probability of failure, $\sigma^*_{\mathrm{fs}}$ is the stress at failure of an individual RPC specimen, $\sigma^*_0$ is the characteristic strength of the RPC, and $m$ is the Weibull modulus. Fitting a linear function to a Weibull plot of the data using a least squares regression yields a Weibull modulus of 6.3 and a characteristic strength of 1.68 MPa. The limits of the 90% confidence interval on the Weibull modulus for the 21 flexural strength data points [87] are:

$$4.4 \leq m \leq 7.9 \tag{A.5}$$

RPCs have a been shown to have their flaws volume distributed as opposed to surface distributed [94], so the Weibull modulus calculated is useful for estimating the strength of the ceria RPC for different loading situations and sizes using Weibull strength scaling (Eq. (A.6)) using effective volume calculations:

$$\frac{\sigma^*_1}{\sigma^*_2} = \left(\frac{V_{\mathrm{E},2}}{V_{\mathrm{E},1}}\right)^{1/m} \tag{A.6}$$

where $\sigma^*_1$ and $\sigma^*_2$ are characteristic strengths of RPCs 1 and 2 having different sizes or volumetric stress distributions, respectively, and $V_{\mathrm{E},1}$ and $V_{\mathrm{E},2}$ are the effective volumes of RPCs 1 and 2, respectively, based on their sizes and loading configurations. For the

3-point flexural test in this study, the effective volume is calculated to be 290 $mm^3$ using Eq. (A.7) [89].

$$V_{\mathrm{E}} = \frac{L_{\mathrm{o}} w h}{2\left(m+1\right)^2} \tag{A.7}$$

With the characteristic strength, Weibull modulus, and effective volume defined, the data can be used in the consideration of potential designs of structural ceria RPC components.

# Appendix B

# Plateau Border Arc Equations

The equations and limits of validity describing the double Plateau border geometry in Fig. 2.3 are presented in Tables B.1–B.3.

Table B.1: Equations defining the arcs of the internal Plateau border

| Arc | Equation | Limits |
|---|---|---|
| 1 | $\left(y-\frac{\alpha_\mathrm{i}}{2}\right)^2+\left(z-\frac{\sqrt{3}\alpha_\mathrm{i}}{2}\right)^2=R_\mathrm{i}^2$ | $y\leq 2c_\mathrm{i};\ z\leq\sqrt{3}c_\mathrm{i}$ |
| 2 | $\left(y-\frac{\alpha_\mathrm{i}}{2}\right)^2+\left(z+\frac{\sqrt{3}\alpha_\mathrm{i}}{2}\right)^2=R_\mathrm{i}^2$ | $y\leq 2c_\mathrm{i};\ z\geq-\sqrt{3}c_\mathrm{i}$ |
| 3 | $\left(y+\alpha_\mathrm{i}\right)^2+z^2=R_\mathrm{i}^2$ | $y\geq -c_\mathrm{i}$ |

Table B.2: Equations defining the arcs of the external Plateau border, when $0\leq\theta_\mathrm{o}<30^\circ$

| Arc | Equation | Limits |
|---|---|---|
| 4 | $\left(y-\frac{\alpha_\mathrm{o}}{2}\right)^2+\left(z-\frac{\sqrt{3}\alpha_\mathrm{o}}{2}\right)^2=R_\mathrm{o}^2$ | $y\leq 2c_\mathrm{o};\ z\leq\sqrt{3}c_\mathrm{o}$ |
| 5 | $\left(y-\frac{\alpha_\mathrm{o}}{2}\right)^2+\left(z+\frac{\sqrt{3}\alpha_\mathrm{o}}{2}\right)^2=R_\mathrm{o}^2$ | $y\leq 2c_\mathrm{o};\ z\geq-\sqrt{3}c_\mathrm{o}$ |
| 6 | $\left(y+\alpha_\mathrm{o}\right)^2+z^2=R_\mathrm{o}^2$ | $y\geq -c_\mathrm{o}$ |

Table B.3: Equations defining the arcs of the external Plateau border, when $30° < \theta_o \leq 90°$

| Arc | Equation | Limits |
|---|---|---|
| 4 | $\left(y + \frac{\alpha_o}{2}\right)^2 + \left(z + \frac{\sqrt{3}\alpha_o}{2}\right)^2 = R_o^2$ | $y \geq -c_o$; $z \geq 0$ |
| 5 | $\left(y + \frac{\alpha_o}{2}\right)^2 + \left(z - \frac{\sqrt{3}\alpha_o}{2}\right)^2 = R_o^2$ | $y \geq -c_o$; $z \leq 0$ |
| 6 | $(y - \alpha_o)^2 + z^2 = R_o^2$ | $y \leq -c_o$ |

# Appendix C

# Solving for the Shear Modulus

Note: The derivation of the shear modulus equation utilizes the shear modulus unit cell defined by Gong et al. in Ref. [22]. The first free body diagram (FBD) used is in Fig. C.1.

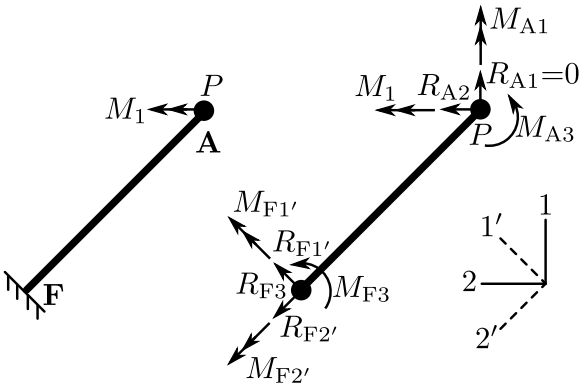


Figure C.1: FBD showing loads and moments on beam AF

The constraints on the beam are that Point A has zero displacement in the 2-direction, and Point A has zero rotation in the 1- and 3-directions. Balancing the forces and moments in the $1'$-, $2'$-, and 3-directions:

$$R_{\mathrm{F}1'} + \frac{\sqrt{2}}{2}R_{\mathrm{A}1} + \frac{\sqrt{2}}{2}R_{\mathrm{A}2} = 0 \tag{C.1}$$

$$R_{\mathrm{F}2'} - \frac{\sqrt{2}}{2}R_{\mathrm{A}1} + \frac{\sqrt{2}}{2}R_{\mathrm{A}2} = 0 \tag{C.2}$$

$$R_{\mathrm{F}3} + P = 0 \tag{C.3}$$

$$M_{\mathrm{F}1'} + \frac{\sqrt{2}}{2}M_{\mathrm{A}1} + \frac{\sqrt{2}}{2}M_1 - PL = 0 \tag{C.4}$$

$$M_{\mathrm{F}2'} - \frac{\sqrt{2}}{2}M_{\mathrm{A}1} + \frac{\sqrt{2}}{2}M_1 = 0 \tag{C.5}$$

$$M_{\mathrm{F}3} + M_{\mathrm{A}3} + \frac{\sqrt{2}}{2}R_{\mathrm{A}2}L + \frac{\sqrt{2}}{2}R_{\mathrm{A}1}L = 0 \tag{C.6}$$

To solve for the internal forces, the FBD in Fig. C.2 is used.

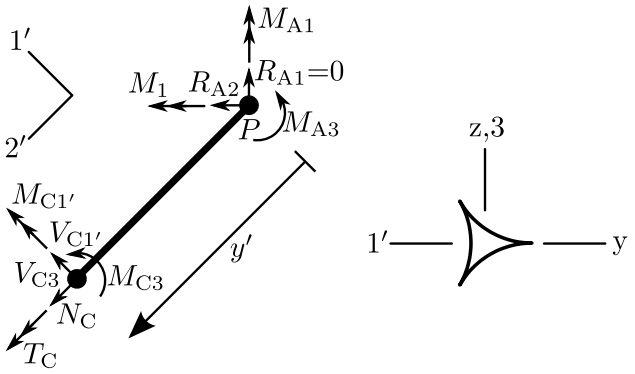


Figure C.2: FBD showing the loads, moments, and torque on beam AC, and the orientations of the axes with respect to the Plateau border cross section

Breaking the ligament at Point C and balancing the forces and moments in the $1'$-, $2'$-, and 3-directions:

$$V_{C1'} + \frac{\sqrt{2}}{2} R_{A1} + \frac{\sqrt{2}}{2} R_{A2} = 0 \tag{C.7}$$

$$N_C - \frac{\sqrt{2}}{2} R_{A1} + \frac{\sqrt{2}}{2} R_{A2} = 0 \tag{C.8}$$

$$V_{C3} + P = 0 \tag{C.9}$$

$$M_{C1'} + \frac{\sqrt{2}}{2} M_{A1} + \frac{\sqrt{2}}{2} M_1 - PL\left(\xi + \frac{1}{2}\right) = 0 \tag{C.10}$$

$$T_C - \frac{\sqrt{2}}{2} M_{A1} + \frac{\sqrt{2}}{2} M_1 = 0 \tag{C.11}$$

$$M_{C3} + M_{A3} + \frac{\sqrt{2}}{2} R_{A1} L\left(\xi + \frac{1}{2}\right) + \frac{\sqrt{2}}{2} R_{A2} L\left(\xi + \frac{1}{2}\right) = 0 \tag{C.12}$$

Solving for the internal forces and moments:

$$N_C = \frac{R_{A1} - R_{A2}}{\sqrt{2}} \tag{C.13}$$

$$M_{C1'} = \frac{1}{2}\left(-\sqrt{2} M_1 - \sqrt{2} M_{A1} + LP\left(1 + 2\xi\right)\right) \tag{C.14}$$

$$M_{C3} = -M_{A3} - \frac{L\left(R_{A1} + R_{A2}\right)\left(1 + 2\xi\right)}{2\sqrt{2}} \tag{C.15}$$

$$V_{C1'} = -\frac{R_{A1} + R_{A2}}{\sqrt{2}} \tag{C.16}$$

$$V_{C3} = -P \tag{C.17}$$

$$T_C = \frac{-M_1 + M_{A1}}{\sqrt{2}} \tag{C.18}$$

The displacement of Point A in the 2-direction relates to the unknown moments and

forces as:

$$\bar{\delta}_{\mathrm{A2}} = 0 = \int_{-\frac{1}{2}}^{\frac{1}{2}} \frac{L}{E_{\mathrm{s}} A(\xi)} N_{\mathrm{C}} \frac{\partial N_{\mathrm{C}}}{\partial R_{\mathrm{A2}}} \,\mathrm{d}\xi + \int_{-\frac{1}{2}}^{\frac{1}{2}} \frac{L}{E_{\mathrm{s}} I(\xi)} M_{\mathrm{C1'}} \frac{\partial M_{\mathrm{C1'}}}{\partial R_{\mathrm{A2}}} \,\mathrm{d}\xi + \int_{-\frac{1}{2}}^{\frac{1}{2}} \frac{L}{E_{\mathrm{s}} I(\xi)} M_{\mathrm{C3}} \frac{\partial M_{\mathrm{C3}}}{\partial R_{\mathrm{A2}}} \,\mathrm{d}\xi + \int_{-\frac{1}{2}}^{\frac{1}{2}} \frac{L}{G_{\mathrm{s}} A(\xi)} \beta_{\mathrm{z}}(\xi) V_{\mathrm{C1'}} \frac{\partial V_{\mathrm{C1'}}}{\partial R_{\mathrm{A2}}} \,\mathrm{d}\xi + \int_{-\frac{1}{2}}^{\frac{1}{2}} \frac{L}{G_{\mathrm{s}} A(\xi)} \beta_{\mathrm{y}}(\xi) V_{\mathrm{C3}} \frac{\partial V_{\mathrm{C3}}}{\partial R_{\mathrm{A2}}} \,\mathrm{d}\xi + \int_{-\frac{1}{2}}^{\frac{1}{2}} \frac{L}{G_{\mathrm{s}} J_{\mathrm{T}}(\xi)} T_{\mathrm{C}} \frac{\partial T_{\mathrm{C}}}{\partial R_{\mathrm{A2}}} \,\mathrm{d}\xi \tag{C.19}$$

where

$$\frac{\partial N_{\mathrm{C}}}{\partial R_{\mathrm{A2}}} = -\frac{1}{\sqrt{2}} \tag{C.20}$$

$$\frac{\partial M_{\mathrm{C1'}}}{\partial R_{\mathrm{A2}}} = 0 \tag{C.21}$$

$$\frac{\partial M_{\mathrm{C3}}}{\partial R_{\mathrm{A2}}} = -\frac{L\,(1+2\xi)}{2\sqrt{2}} \tag{C.22}$$

$$\frac{\partial V_{\mathrm{C1'}}}{\partial R_{\mathrm{A2}}} = -\frac{1}{\sqrt{2}} \tag{C.23}$$

$$\frac{\partial V_{\mathrm{C3}}}{\partial R_{\mathrm{A2}}} = 0 \tag{C.24}$$

$$\frac{\partial T_{\mathrm{C}}}{\partial R_{\mathrm{A2}}} = 0 \tag{C.25}$$

Simplifying Eq. (C.19):

$$2\sqrt{2}\,(C_{0\mathrm{I}} + 2C_{1\mathrm{I}})\,L M_{\mathrm{A3}} + 4C_{0\mathrm{A}}\,(-R_{\mathrm{A1}} + R_{\mathrm{A2}}) + (C_{0\mathrm{I}} + 4\,(C_{1\mathrm{I}} + C_{2\mathrm{I}}))\,L^2\,(R_{\mathrm{A1}} + R_{\mathrm{A2}}) + 8C_{\beta_{\mathrm{z}}0\mathrm{A}}\,(R_{\mathrm{A1}} + R_{\mathrm{A2}})\,(1+\nu_{\mathrm{s}}) = 0 \tag{C.26}$$

The rotation of Point A in the 1-direction relates to the unknown moments and forces as:

$$\begin{aligned}\bar{\theta}_{\mathrm{A1}} = 0 = &\int_{-\frac{1}{2}}^{\frac{1}{2}} \frac{L}{E_{\mathrm{s}}A(\xi)} N_{\mathrm{C}} \frac{\partial N_{\mathrm{C}}}{\partial M_{\mathrm{A1}}}\, \mathrm{d}\xi + \int_{-\frac{1}{2}}^{\frac{1}{2}} \frac{L}{E_{\mathrm{s}}I(\xi)} M_{\mathrm{C1'}} \frac{\partial M_{\mathrm{C1'}}}{\partial M_{\mathrm{A1}}}\, \mathrm{d}\xi + \\ &\int_{-\frac{1}{2}}^{\frac{1}{2}} \frac{L}{E_{\mathrm{s}}I(\xi)} M_{\mathrm{C3}} \frac{\partial M_{\mathrm{C3}}}{\partial M_{\mathrm{A1}}}\, \mathrm{d}\xi + \int_{-\frac{1}{2}}^{\frac{1}{2}} \frac{L}{G_{\mathrm{s}}A(\xi)} \beta_{\mathrm{z}}(\xi) V_{\mathrm{C1'}} \frac{\partial V_{\mathrm{C1'}}}{\partial M_{\mathrm{A1}}}\, \mathrm{d}\xi + \\ &\int_{-\frac{1}{2}}^{\frac{1}{2}} \frac{L}{G_{\mathrm{s}}A(\xi)} \beta_{\mathrm{y}}(\xi) V_{\mathrm{C3}} \frac{\partial V_{\mathrm{C3}}}{\partial M_{\mathrm{A1}}}\, \mathrm{d}\xi + \int_{-\frac{1}{2}}^{\frac{1}{2}} \frac{L}{G_{\mathrm{s}}J_{\mathrm{T}}(\xi)} T_{\mathrm{C}} \frac{\partial T_{\mathrm{C}}}{\partial M_{\mathrm{A1}}}\, \mathrm{d}\xi \end{aligned} \tag{C.27}$$

where

$$\frac{\partial N_{\mathrm{C}}}{\partial M_{\mathrm{A1}}} = 0 \tag{C.28}$$

$$\frac{\partial M_{\mathrm{C1'}}}{\partial M_{\mathrm{A1}}} = -\frac{1}{\sqrt{2}} \tag{C.29}$$

$$\frac{\partial M_{\mathrm{C3}}}{\partial M_{\mathrm{A1}}} = 0 \tag{C.30}$$

$$\frac{\partial V_{\mathrm{C1'}}}{\partial M_{\mathrm{A1}}} = 0 \tag{C.31}$$

$$\frac{\partial V_{\mathrm{C3}}}{\partial M_{\mathrm{A1}}} = 0 \tag{C.32}$$

$$\frac{\partial T_{\mathrm{C}}}{\partial M_{\mathrm{A1}}} = \frac{1}{\sqrt{2}} \tag{C.33}$$

Simplifying Eq. (C.27):

$$\begin{aligned}&-\sqrt{2}\left(C_{0\mathrm{I}} + 2C_{1\mathrm{I}}\right) LP + 2M_1 \left(C_{0\mathrm{I}} - 2C_{0\mathrm{J_T}}(1+\nu_{\mathrm{s}})\right) + \\ &2M_{\mathrm{A1}} \left(C_{0\mathrm{I}} + 2C_{0\mathrm{J_T}}(1+\nu_{\mathrm{s}})\right) = 0\end{aligned} \tag{C.34}$$

The rotation of Point A in the 3-direction relates to the unknown moments and forces as:

$$\begin{aligned}\bar{\theta}_{\mathrm{A3}} = 0 = &\int_{-\frac{1}{2}}^{\frac{1}{2}} \frac{L}{E_{\mathrm{s}}A(\xi)} N_{\mathrm{C}} \frac{\partial N_{\mathrm{C}}}{\partial M_{\mathrm{A3}}}\, \mathrm{d}\xi + \int_{-\frac{1}{2}}^{\frac{1}{2}} \frac{L}{E_{\mathrm{s}}I(\xi)} M_{\mathrm{C1'}} \frac{\partial M_{\mathrm{C1'}}}{\partial M_{\mathrm{A3}}}\, \mathrm{d}\xi + \\ &\int_{-\frac{1}{2}}^{\frac{1}{2}} \frac{L}{E_{\mathrm{s}}I(\xi)} M_{\mathrm{C3}} \frac{\partial M_{\mathrm{C3}}}{\partial M_{\mathrm{A3}}}\, \mathrm{d}\xi + \int_{-\frac{1}{2}}^{\frac{1}{2}} \frac{L}{G_{\mathrm{s}}A(\xi)} \beta_{\mathrm{z}}(\xi) V_{\mathrm{C1'}} \frac{\partial V_{\mathrm{C1'}}}{\partial M_{\mathrm{A3}}}\, \mathrm{d}\xi + \\ &\int_{-\frac{1}{2}}^{\frac{1}{2}} \frac{L}{G_{\mathrm{s}}A(\xi)} \beta_{\mathrm{y}}(\xi) V_{\mathrm{C3}} \frac{\partial V_{\mathrm{C3}}}{\partial M_{\mathrm{A3}}}\, \mathrm{d}\xi + \int_{-\frac{1}{2}}^{\frac{1}{2}} \frac{L}{G_{\mathrm{s}}J_{\mathrm{T}}(\xi)} T_{\mathrm{C}} \frac{\partial T_{\mathrm{C}}}{\partial M_{\mathrm{A3}}}\, \mathrm{d}\xi \end{aligned} \tag{C.35}$$

where

$$\frac{\partial N_{\mathrm{C}}}{\partial M_{\mathrm{A3}}} = 0 \tag{C.36}$$

$$\frac{\partial M_{\mathrm{C1'}}}{\partial M_{\mathrm{A3}}} = 0 \tag{C.37}$$

$$\frac{\partial M_{\mathrm{C3}}}{\partial M_{\mathrm{A3}}} = -1 \tag{C.38}$$

$$\frac{\partial V_{\mathrm{C1'}}}{\partial M_{\mathrm{A3}}} = 0 \tag{C.39}$$

$$\frac{\partial V_{\mathrm{C3}}}{\partial M_{\mathrm{A3}}} = 0 \tag{C.40}$$

$$\frac{\partial T_{\mathrm{C}}}{\partial M_{\mathrm{A3}}} = 0 \tag{C.41}$$

Simplifying Eq. (C.35):

$$4C_{0\mathrm{I}}M_{\mathrm{A3}} + \sqrt{2}\left(C_{0\mathrm{I}} + 2C_{1\mathrm{I}}\right) L \left(R_{\mathrm{A1}} + R_{\mathrm{A2}}\right) = 0 \tag{C.42}$$

Solving Eqs. (C.26), (C.34), and (C.42) for the unknown forces and moments, $R_{\mathrm{A2}}$,

$M_{\mathrm{A1}}$, and $M_{\mathrm{A3}}$:

$$R_{\mathrm{A2}} = R_{\mathrm{A1}}\left(-1 + \frac{2C_{0\mathrm{A}}C_{0\mathrm{I}}}{-C_{1\mathrm{I}}^2L^2 + C_{0\mathrm{I}}\left(C_{0\mathrm{A}} + C_{2\mathrm{I}}L^2 + 2C_{\beta_{\mathrm{z}}0\mathrm{A}}(1+\nu_{\mathrm{s}})\right)}\right) \tag{C.43}$$

$$M_{\mathrm{A1}} = \frac{\sqrt{2}\left(C_{0\mathrm{I}} + 2C_{1\mathrm{I}}\right)LP - 2M_1\left(C_{0\mathrm{I}} - 2C_{0\mathrm{J_T}}(1+\nu_{\mathrm{s}})\right)}{2\left(C_{0\mathrm{I}} + 2C_{0\mathrm{J_T}}(1+\nu_{\mathrm{s}})\right)} \tag{C.44}$$

$$M_{\mathrm{A3}} = \frac{-C_{0\mathrm{A}}\left(C_{0\mathrm{I}} + 2C_{1\mathrm{I}}\right)LR_{\mathrm{A1}}}{\sqrt{2}\left(-C_{1\mathrm{I}}^2L^2 + C_{0\mathrm{I}}\left(C_{0\mathrm{A}} + C_{2\mathrm{I}}L^2 + 2C_{\beta_{\mathrm{z}}0\mathrm{A}}(1+\nu_{\mathrm{s}})\right)\right)} \tag{C.45}$$

$R_{\mathrm{A2}}$, $M_{\mathrm{A1}}$, and $M_{\mathrm{A3}}$ are inserted into Eqs. (C.13)–(C.18). The rotation of Point A in the 2-direction relates to the moments and forces as:

$$\begin{aligned}\bar{\theta}_{\mathrm{A2}} = &\int_{-\frac{1}{2}}^{\frac{1}{2}} \frac{L}{E_{\mathrm{s}}A(\xi)}N_{\mathrm{C}}\frac{\partial N_{\mathrm{C}}}{\partial M_1}\,\mathrm{d}\xi + \int_{-\frac{1}{2}}^{\frac{1}{2}} \frac{L}{E_{\mathrm{s}}I(\xi)}M_{\mathrm{C1'}}\frac{\partial M_{\mathrm{C1'}}}{\partial M_1}\,\mathrm{d}\xi + \\ &\int_{-\frac{1}{2}}^{\frac{1}{2}} \frac{L}{E_{\mathrm{s}}I(\xi)}M_{\mathrm{C3}}\frac{\partial M_{\mathrm{C3}}}{\partial M_1}\,\mathrm{d}\xi + \int_{-\frac{1}{2}}^{\frac{1}{2}} \frac{L}{G_{\mathrm{s}}A(\xi)}\beta_{\mathrm{z}}(\xi)V_{\mathrm{C1'}}\frac{\partial V_{\mathrm{C1'}}}{\partial M_1}\,\mathrm{d}\xi + \\ &\int_{-\frac{1}{2}}^{\frac{1}{2}} \frac{L}{G_{\mathrm{s}}A(\xi)}\beta_{\mathrm{y}}(\xi)V_{\mathrm{C3}}\frac{\partial V_{\mathrm{C3}}}{\partial M_1}\,\mathrm{d}\xi + \int_{-\frac{1}{2}}^{\frac{1}{2}} \frac{L}{G_{\mathrm{s}}J_{\mathrm{T}}(\xi)}T_{\mathrm{C}}\frac{\partial T_{\mathrm{C}}}{\partial M_1}\,\mathrm{d}\xi\end{aligned} \tag{C.46}$$

where

$$\frac{\partial N_{\mathrm{C}}}{\partial M_1} = 0 \tag{C.47}$$

$$\frac{\partial M_{\mathrm{C1'}}}{\partial M_1} = -\frac{2\sqrt{2}C_{0\mathrm{J_T}}(1+\nu_{\mathrm{s}})}{C_{0\mathrm{I}} + 2C_{0\mathrm{J_T}}(1+\nu_{\mathrm{s}})} \tag{C.48}$$

$$\frac{\partial M_{\mathrm{C3}}}{\partial M_1} = 0 \tag{C.49}$$

$$\frac{\partial V_{\mathrm{C1'}}}{\partial M_1} = 0 \tag{C.50}$$

$$\frac{\partial V_{\mathrm{C3}}}{\partial M_1} = 0 \tag{C.51}$$

$$\frac{\partial T_{\mathrm{C}}}{\partial M_1} = -\frac{\sqrt{2}C_{0\mathrm{I}}}{C_{0\mathrm{I}} + 2C_{0\mathrm{J_T}}(1+\nu_{\mathrm{s}})} \tag{C.52}$$

Simplifying Eq. (C.46):

$$\bar{\theta}_{\mathrm{A2}} = \frac{C_{0\mathrm{J_T}} L \left(4C_{0\mathrm{I}} M_1 - \sqrt{2}\left(C_{0\mathrm{I}} + 2C_{1\mathrm{I}}\right) LP\right)(1+\nu_{\mathrm{s}})}{E_{\mathrm{s}}\left(C_{0\mathrm{I}} + 2C_{0\mathrm{J_T}}(1+\nu_{\mathrm{s}})\right)} \tag{C.53}$$

The same analysis is performed on the free body diagram in Fig. C.3.

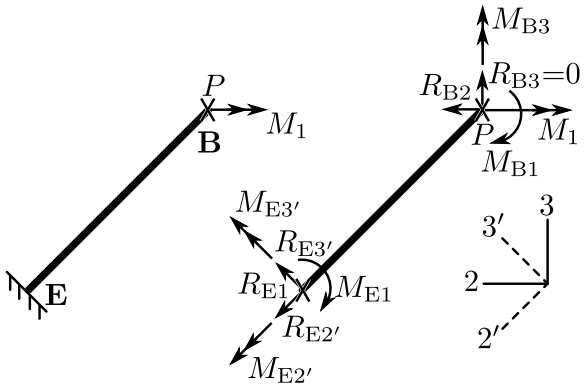


Figure C.3: FBD showing loads and moments on beam AF

The result is the rotation of Point B in the 2-direction:

$$\bar{\theta}_{\mathrm{B2}} = -\frac{C_{0\mathrm{J_T}} L \left(4C_{0\mathrm{I}} M_1 - \sqrt{2}\left(C_{0\mathrm{I}} + 2C_{1\mathrm{I}}\right) LP\right)(1+\nu_{\mathrm{s}})}{E_{\mathrm{s}}\left(C_{0\mathrm{I}} + 2C_{0\mathrm{J_T}}(1+\nu_{\mathrm{s}})\right)} \tag{C.54}$$

The next free body diagram that is used to solve for the 2-direction rotation of Points A and B is shown in Fig. C.4.

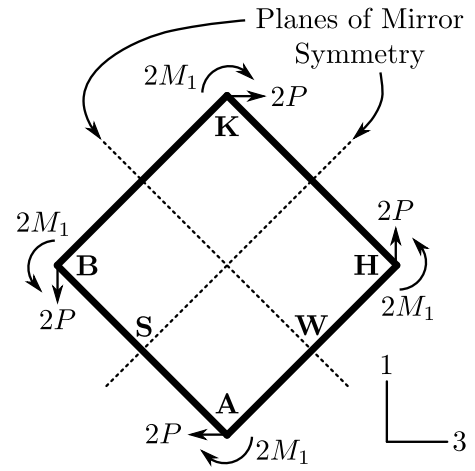


Figure C.4: FBD showing loads and moments on beam structure ABKH

Using the planes of mirror symmetry in the structure, the ligament structure is simplified in Fig. C.5. Note at Point S there is no $1'$-direction displacement and no 2-direction rotation. At Point K there is no $3'$-direction displacement and no 2-direction rotation.

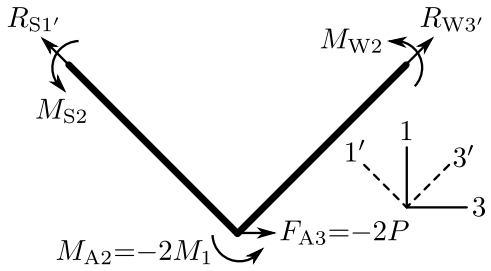


Figure C.5: FBD showing the loads and moments on beam structure SAW

Solving the force and moment balance:

$$R_{\mathrm{S1}'} - \frac{\sqrt{2}}{2} F_{\mathrm{A3}} = 0 \tag{C.55}$$

$$R_{\mathrm{W3}'} + \frac{\sqrt{2}}{2} F_{\mathrm{A3}} = 0 \tag{C.56}$$

$$M_{\mathrm{S2}} + M_{\mathrm{W2}} + M_{\mathrm{A2}} = 0 \tag{C.57}$$

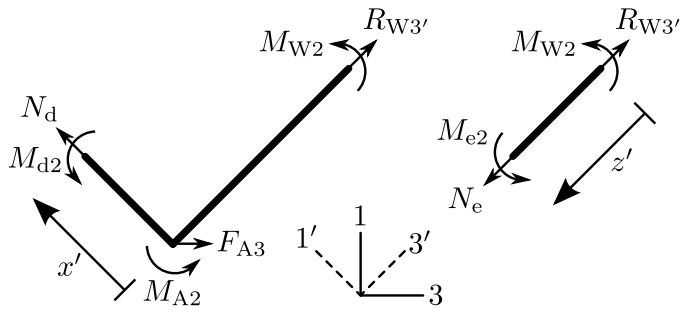


Figure C.6: FBD showing the internal loads and moments on the sections of beam structure SAW

Performing a force balance to solve for the internal forces using Fig. C.6:

$$N_{\mathrm{d}} = \frac{\sqrt{2}}{2} F_{\mathrm{A3}} \tag{C.58}$$

$$R_{\mathrm{W3}'} = -\frac{\sqrt{2}}{2} F_{\mathrm{A3}} \tag{C.59}$$

$$M_{\mathrm{d2}} = -M_{\mathrm{W2}} - M_{\mathrm{A2}} \tag{C.60}$$

$$N_{\mathrm{e}} = R_{\mathrm{W3}'} \tag{C.61}$$

$$M_{\mathrm{e2}} = -M_{\mathrm{W2}} \tag{C.62}$$

The rotation of Point W in the 2-direction relates to the unknown moments and forces as:

$$\theta_{\mathrm{W2}} = 0 = \int_0^{\frac{1}{2}} \frac{L}{E_{\mathrm{s}} A(\xi)} N_{\mathrm{e}} \frac{\partial N_{\mathrm{e}}}{\partial M_{\mathrm{W2}}} \, \mathrm{d}\xi + \int_0^{\frac{1}{2}} \frac{L}{E_{\mathrm{s}} I(\xi)} M_{\mathrm{e2}} \frac{\partial M_{\mathrm{e2}}}{\partial M_{\mathrm{W2}}} \, \mathrm{d}\xi + \int_{-\frac{1}{2}}^{0} \frac{L}{E_{\mathrm{s}} A(\xi)} N_{\mathrm{d}} \frac{\partial N_{\mathrm{d}}}{\partial M_{\mathrm{W2}}} \, \mathrm{d}\xi + \int_{-\frac{1}{2}}^{0} \frac{L}{E_{\mathrm{s}} I(\xi)} M_{\mathrm{d2}} \frac{\partial M_{\mathrm{d2}}}{\partial M_{\mathrm{W2}}} \, \mathrm{d}\xi \tag{C.63}$$

where

$$\frac{\partial N_{\mathrm{e}}}{\partial M_{\mathrm{W2}}} = 0 \tag{C.64}$$

$$\frac{\partial M_{\mathrm{e2}}}{\partial M_{\mathrm{W2}}} = -1 \tag{C.65}$$

$$\frac{\partial N_{\mathrm{d}}}{\partial M_{\mathrm{W2}}} = 0 \tag{C.66}$$

$$\frac{\partial M_{\mathrm{d2}}}{\partial M_{\mathrm{W2}}} = -1 \tag{C.67}$$

Simplifying Eq. (C.63):

$$M_{\mathrm{A2}} + 2M_{\mathrm{W2}} = 0 \tag{C.68}$$

Solving for $M_{\mathrm{W2}}$:

$$M_{\mathrm{W2}} = -\frac{M_{\mathrm{A2}}}{2} \tag{C.69}$$

$M_{\mathrm{W2}}$ is inserted into Eqs. (C.60) and (C.62). The rotation of Point A in the 2-direction relates to the moment $M_{\mathrm{A2}}$ as:

$$\theta_{\mathrm{A2}} = \int_0^{\frac{1}{2}} \frac{L}{E_{\mathrm{s}} A(\xi)} N_{\mathrm{e}} \frac{\partial N_{\mathrm{e}}}{\partial M_{\mathrm{A2}}}\, \mathrm{d}\xi + \int_0^{\frac{1}{2}} \frac{L}{E_{\mathrm{s}} I(\xi)} M_{\mathrm{e2}} \frac{\partial M_{\mathrm{e2}}}{\partial M_{\mathrm{A2}}}\, \mathrm{d}\xi + \int_{-\frac{1}{2}}^{0} \frac{L}{E_{\mathrm{s}} A(\xi)} N_{\mathrm{d}} \frac{\partial N_{\mathrm{d}}}{\partial M_{\mathrm{A2}}}\, \mathrm{d}\xi + \int_{-\frac{1}{2}}^{0} \frac{L}{E_{\mathrm{s}} I(\xi)} M_{\mathrm{d2}} \frac{\partial M_{\mathrm{d2}}}{\partial M_{\mathrm{A2}}}\, \mathrm{d}\xi \tag{C.70}$$

where

$$\frac{\partial N_{\mathrm{e}}}{\partial M_{\mathrm{A2}}} = 0 \tag{C.71}$$

$$\frac{\partial M_{\mathrm{e2}}}{\partial M_{\mathrm{A2}}} = \frac{1}{2} \tag{C.72}$$

$$\frac{\partial N_{\mathrm{d}}}{\partial M_{\mathrm{A2}}} = 0 \tag{C.73}$$

$$\frac{\partial M_{\mathrm{d2}}}{\partial M_{\mathrm{A2}}} = -\frac{1}{2} \tag{C.74}$$

Simplifying Eq. (C.70):

$$\theta_{\mathrm{A2}} = \frac{C_{0\mathrm{I}} L M_{\mathrm{A2}}}{4 E_{\mathrm{s}}} \tag{C.75}$$

By definition:

$$M_{\mathrm{A2}} = -2 M_1 \tag{C.76}$$

From symmetry:

$$\theta_{\mathrm{B2}} = -\theta_{\mathrm{A2}} \tag{C.77}$$

Therefore:

$$\theta_{\mathrm{A2}} = -\frac{C_{0\mathrm{I}} L M_1}{2E_{\mathrm{s}}} \tag{C.78}$$

$$\theta_{\mathrm{B2}} = \frac{C_{0\mathrm{I}} L M_1}{2E_{\mathrm{s}}} \tag{C.79}$$

The displacement of Point A in the 3-direction, $\delta_{\mathrm{A3}}$, relates to the force $F_{\mathrm{A3}}$ as:

$$\begin{aligned}\delta_{\mathrm{A3}} = &\int_0^{\frac{1}{2}} \frac{L}{E_{\mathrm{s}} A(\xi)} N_{\mathrm{e}} \frac{\partial N_{\mathrm{e}}}{\partial F_{\mathrm{A3}}}\, \mathrm{d}\xi + \int_0^{\frac{1}{2}} \frac{L}{E_{\mathrm{s}} I(\xi)} M_{\mathrm{e2}} \frac{\partial M_{\mathrm{e2}}}{\partial F_{\mathrm{A3}}}\, \mathrm{d}\xi + \\ &\int_{-\frac{1}{2}}^{0} \frac{L}{E_{\mathrm{s}} A(\xi)} N_{\mathrm{d}} \frac{\partial N_{\mathrm{d}}}{\partial F_{\mathrm{A3}}}\, \mathrm{d}\xi + \int_{-\frac{1}{2}}^{0} \frac{L}{E_{\mathrm{s}} I(\xi)} M_{\mathrm{d2}} \frac{\partial M_{\mathrm{d2}}}{\partial F_{\mathrm{A3}}}\, \mathrm{d}\xi\end{aligned} \tag{C.80}$$

where

$$\frac{\partial N_{\mathrm{e}}}{\partial F_{\mathrm{A3}}} = -\frac{1}{\sqrt{2}} \tag{C.81}$$

$$\frac{\partial M_{\mathrm{e2}}}{\partial F_{\mathrm{A3}}} = 0 \tag{C.82}$$

$$\frac{\partial N_{\mathrm{d}}}{\partial F_{\mathrm{A3}}} = \frac{1}{\sqrt{2}} \tag{C.83}$$

$$\frac{\partial M_{\mathrm{d2}}}{\partial F_{\mathrm{A3}}} = 0 \tag{C.84}$$

Simplifying Eq. (C.80):

$$\delta_{\mathrm{A3}} = \frac{F_{\mathrm{A3}} L}{2E_{\mathrm{s}}} C_{0\mathrm{A}} \tag{C.85}$$

By definition:

$$F_{\mathrm{A3}} = -2P \tag{C.86}$$

From symmetry:

$$\delta_{\mathrm{K3}} = -\delta_{\mathrm{A3}} \tag{C.87}$$

From symmetry, the relative displacement of Point A with respect to Point K in the 3-direction is:

$$\begin{aligned} \Delta_3 &= \delta_{\mathrm{K3}} - \delta_{\mathrm{A3}} \\ &= \frac{2C_{0\mathrm{A}}LP}{E_{\mathrm{s}}} \end{aligned} \tag{C.88}$$

From symmetry, the relative displacement of Point B with respect to Point H in the 1-direction is:

$$\begin{aligned} \Delta_1 &= \Delta_3 \\ &= \frac{2C_{0\mathrm{A}}LP}{E_{\mathrm{s}}} \end{aligned} \tag{C.89}$$

Using the compatibility condition, $\theta_{\mathrm{B2}} - \theta_{\mathrm{A2}} = \bar{\theta}_{\mathrm{B2}} - \bar{\theta}_{\mathrm{A2}}$, and solving for $M_1$ in terms of load $P$:

$$M_1 = \frac{2\sqrt{2}C_{0\mathrm{J_T}}\left(C_{0\mathrm{I}} + 2C_{1\mathrm{I}}\right)LP(1+\nu_{\mathrm{s}})}{C_{0\mathrm{I}}\left(C_{0\mathrm{I}} + 10C_{0\mathrm{J_T}}(1+\nu_{\mathrm{s}})\right)} \tag{C.90}$$

Using Eqs. (C.13)–(C.18), (C.43)–(C.45) and (C.90), the displacement of Point A in

the 3-direction in Fig. C.1 relates to force $P$ as:

$$\begin{aligned}\bar{\delta}_{\mathrm{A3}} = &\int_{-\frac{1}{2}}^{\frac{1}{2}} \frac{L}{E_{\mathrm{s}}A(\xi)} N_{\mathrm{C}} \frac{\partial N_{\mathrm{C}}}{\partial P}\, \mathrm{d}\xi + \int_{-\frac{1}{2}}^{\frac{1}{2}} \frac{L}{E_{\mathrm{s}}I(\xi)} M_{\mathrm{C1'}} \frac{\partial M_{\mathrm{C1'}}}{\partial P}\, \mathrm{d}\xi + \\ &\int_{-\frac{1}{2}}^{\frac{1}{2}} \frac{L}{E_{\mathrm{s}}I(\xi)} M_{\mathrm{C3}} \frac{\partial M_{\mathrm{C3}}}{\partial P}\, \mathrm{d}\xi + \int_{-\frac{1}{2}}^{\frac{1}{2}} \frac{L}{G_{\mathrm{s}}A(\xi)} \beta_{\mathrm{z}}(\xi) V_{\mathrm{C1'}} \frac{\partial V_{\mathrm{C1'}}}{\partial P}\, \mathrm{d}\xi + \\ &\int_{-\frac{1}{2}}^{\frac{1}{2}} \frac{L}{G_{\mathrm{s}}A(\xi)} \beta_{\mathrm{y}}(\xi) V_{\mathrm{C3}} \frac{\partial V_{\mathrm{C3}}}{\partial P}\, \mathrm{d}\xi + \int_{-\frac{1}{2}}^{\frac{1}{2}} \frac{L}{G_{\mathrm{s}}J_{\mathrm{T}}(\xi)} T_{\mathrm{C}} \frac{\partial T_{\mathrm{C}}}{\partial P}\, \mathrm{d}\xi \end{aligned} \tag{C.91}$$

where

$$\frac{\partial N_{\mathrm{C}}}{\partial P} = 0 \tag{C.92}$$

$$\frac{\partial M_{\mathrm{C1'}}}{\partial P} = L\left(\frac{-8C_{0\mathrm{J_T}}C_{1\mathrm{I}}(1+\nu_{\mathrm{s}}) + C_{0\mathrm{I}}\left(C_{0\mathrm{J_T}} - C_{1\mathrm{I}} + C_{0\mathrm{J_T}}\nu_{\mathrm{s}}\right)}{C_{0\mathrm{I}}\left(C_{0\mathrm{I}} + 10C_{0\mathrm{J_T}}(1+\nu_{\mathrm{s}})\right)} + \xi\right) \tag{C.93}$$

$$\frac{\partial M_{\mathrm{C3}}}{\partial P} = 0 \tag{C.94}$$

$$\frac{\partial V_{\mathrm{C1'}}}{\partial P} = 0 \tag{C.95}$$

$$\frac{\partial V_{\mathrm{C3}}}{\partial P} = -1 \tag{C.96}$$

$$\frac{\partial T_{\mathrm{C}}}{\partial P} = \frac{\left(C_{0\mathrm{I}} + 2C_{1\mathrm{I}}\right)L}{2\left(C_{0\mathrm{I}} + 10C_{0\mathrm{J_T}}(1+\nu_{\mathrm{s}})\right)} \tag{C.97}$$

Noting that $C_{1\mathrm{I}} = 0$ because the integrand is an odd function and the absolute values of the interval limits are equal, Eq. (C.91) simplifies as:

$$\begin{aligned}\bar{\delta}_{\mathrm{A3}} = &\frac{LP}{2E_{\mathrm{s}}\left(C_{0\mathrm{I}} + 10C_{0\mathrm{J_T}}(1+\nu_{\mathrm{s}})\right)^2}\Big(200C_{0\mathrm{J_T}}^2(1+\nu_{\mathrm{s}})^2\left(C_{2\mathrm{I}}L^2 + 2C_{\beta_{\mathrm{y}}0\mathrm{A}}(1+\nu_{\mathrm{s}})\right) + \\ &C_{0\mathrm{I}}^2\left(4C_{\beta_{\mathrm{y}}0\mathrm{A}}(1+\nu_{\mathrm{s}}) + L^2\left(C_{0\mathrm{J_T}} + 2C_{2\mathrm{I}} + C_{0\mathrm{J_T}}\nu_{\mathrm{s}}\right)\right) + \end{aligned}$$

$$2C_{0\mathrm{I}}C_{0\mathrm{J_T}}(1+\nu_\mathrm{s})\left(40C_{\beta_\mathrm{y}0\mathrm{A}}(1+\nu_\mathrm{s})+L^2\left(C_{0\mathrm{J_T}}+20C_{2\mathrm{I}}+C_{0\mathrm{J_T}}\nu_\mathrm{s}\right)\right)\Big) \tag{C.98}$$

From symmetry:

$$\bar{\delta}_{\mathrm{B1}} = \bar{\delta}_{\mathrm{A3}} \tag{C.99}$$

By definition:

$$\gamma_{13} = \frac{\Delta_1 + 2\bar{\delta}_{\mathrm{B1}}}{2\sqrt{2}L} + \frac{\Delta_3 + 2\bar{\delta}_{\mathrm{A3}}}{2\sqrt{2}L} \tag{C.100}$$

$$\sigma_{13} = \frac{P}{2L^2} \tag{C.101}$$

$$\frac{G^*_{13}}{E_\mathrm{s}} = \frac{\sigma_{13}}{\gamma_{13}} \tag{C.102}$$

Expanding Eq. (C.102) results in Eq. (2.29).[1]

[1] Recall: $G^*_{13} = G^*_{12}$